UNIVERSITY OF CALIFORNIA, SAN DIEGO

Surface Voltages of Polymer Films Electrified through Corona Charging and Contact Electrification

A dissertation submitted in partial satisfaction of the requirements for the degree Doctor of Philosophy

in

Materials Science and Engineering

by

Ying Zhong

Committee in Charge

Professor Yu Qiao, Chair
Professor Prabhakar R. Bandaru
Professor Farhat N. Beg
Professor Renkun Chen
Professor Zhaowei Liu

2017

The dissertation of Ying Zhong is approved, and it is acceptable in quality and form for publication on microfilm and electronically:

Chair

University of California, San Diego

2017

DEDICATION

To my family.

To all who supported me.

To all who helped me to learn and grow.

TABLE OF CONTENTS

LIST OF FIGURES

LIST OF TABLES

ACKNOWLEDGEMENTS

I would like to express my deepest appreciation to my advisor, Professor Yu Qiao, for his great support and inspiration. His advice and guidance will always be invaluable in my scientific pursuits.

I would like to thank my committee members, Professor Prabhakar R. Bandaru, Professor Farhat N. Beg, Professor Renkun Chen, and Professor Zhaowei Liu for their valuable suggestions and time. Special thanks are also due to Professor Chunqing Wang and Professor Sungho Jin for their valuable help.

I would like to thank Mr. Rui Kou, who offered important help with this work, and Dr. Meng Wang, Mr. Lewis Fowlergerace, and Ms. Yun Zhou. Support from other members in the Multifunctional Materials Research Lab, Dr. Yang Shi, Dr. Anh V. Le, Mr. Daniel J. Noelle, and Dr. Brian Chow is also gratefully acknowledged.

I would like to thank my parents for their unconditional support, generous tolerance, and infinite love. I would also like to thank all my friends, who have been standing by my side along the way.

Chapter 2, in part, is currently being prepared to be submitted for publication. Ying Zhong, Rui Kou, Lewis Fowlergerace, Meng Wang, and Yu Qiao. The dissertation author was the primary investigator and first author of the paper.

Chapter 3, in part, is currently being prepared to be submitted for publication. Ying Zhong, Rui Kou, Lewis Fowlergerace, Meng Wang, and Yu Qiao. The dissertation author was the primary investigator and first author of the paper.

Chapter 4, in part, is currently being prepared to be submitted for publication. Ying Zhong, Rui Kou, Lewis Fowlergerace, Meng Wang, and Yu Qiao. The dissertation author was the primary investigator and first author of the paper.

Chapter 5, in part, is currently being prepared to be submitted for publication. Ying Zhong, Rui Kou, Lewis Fowlergerace, Meng Wang, and Yu Qiao. The dissertation author was the primary investigator and first author of the paper.

VITA

2010 Bachelor of Engineering, Harbin Institute of Technology, Harbin, China

2012 Master of Engineering, Harbin Institute of Technology, Harbin, China

2017 Doctor of Philosophy, University of California, San Diego, USA

PUBLICATIONS

JOURNALS

[1] **Zhong Y.**, Zhang F., Wang M., Gardener C.J., Kim G. Liu Y., Leng J., Jin S. Chen R. Reversible Humidity Sensitive Clothing for Personalized Thermoregulation. Scientific Report, 2017, 7.

[2] **Zhong Y.**, An R., Wang C., Zheng Z., Liu Z., Liu C. Li C., Kim T. Jin S. Low Temperature Sintering Cu_6Sn_5 Nanoparticles for Superplastic and Super-uniform High Temperature Circuit Interconnections. Small, 2015, 11(33), 4097-4103.

[3] **Zhong Y.**, Liu W., Wang C., Zhao X., Caers J.F.J.M. The influence of strengthening and recrystallization to the cracking behavior of Ni, Sb, Bi alloyed SnAgCu solder during thermal cycling. Materials Science and Engineering: A, 2016, 652: 264-270.

[4] **Zhong Y.**, Zhang W., Wang C., Li B. Manufacturing and Microstructure of Cu Coated Diamonds/SnAgCu Composite Solder Bumps. Applied Mechanics and Materials. 2013, 288: 323-327.

[5] Zhao C., **Zhong Y.**, Qiao Y. Effects of porosity on dynamic indentation resistance of silica nanofoam, Scientific Report, 2017,7.

[6] Chow B., Chen T., **Zhong Y.**, Qiao Y. Direct Formation of Structural Components Using a Martian Soil Simulant. Scientific Report, 2017, 7.

[7] Zhang W., **Zhong Y.**, Wang C. Effect of diamond additions on wettability and distribution of SnAgCu composite solder. Journal of Materials Science and Technology, 2012, 28(7): 661-665.

[8] Li B., Wang C., Liu W., **Zhong Y.**, An R. Synthesis of Co-doped barium strontium titanate nanofibers by sol-gel/electrospinning process. Materials Letters, 2012, 75: 207-210.

PROCCEDINGS

[1] **Zhong Y.**, Wang C., Zhao X., Caers J.F.J.M. The influence of high melting point elements on the reliability of solder during thermal shock. The 65th IEEE Electronic Components and Technology Conference, 2015.

[2] **Zhong Y.**, Wang C., Caers J.F.J.M., Zhao X. The evolution of IMCs' morphologies and types in SAC and SAC+ solder bumps during thermal shock process. The 14th Electronics Materials & Packaging Conference, 2012: 1-4.

[3] **Zhong Y.**, Wang C., Caers J.F.J.M., Zhao X. Relationship between crack propagation trends and grains in SnAgCu interconnects. The 13th Electronic Packaging Technology and High Density Packaging Conference, 2012: 1200-1204.

[4] **Zhong Y.**, Wei Z., Wang C., Li B. Preparation and microstructure of functionally gradient diamond/SAC composite solder bumps. The 12th Electronic Packaging Technology and High Density Packaging Conference, 2011: 1-5.

PATENTS

[1] Qiao Y., **Zhong Y**. Stabilized Solid-Gap Multilayers. US provisional patent.

[2] Wang C., **Zhong Y.**, Hang C. Manufacturing Lead-free high temperature interconnections by sintering intermetallic nanoparticles at low temperature. CN102922071 A

[3] Wang C., **Zhong Y.**, Hang C. Intermetallic nanoparticle paste for Lead-free high temperature interconnections. CN102922177 B.

ABSTRACT OF THE DISSERTATION

Surface Voltages of Polymer Films Electrified through
Corona Charging and Contact Electrification

by

Ying Zhong

Doctor of Philosophy in Materials Science and Engineering

University of California, San Diego, 2017

Professor Yu Qiao, Chair

A triode corona charging system was developed with controlled charging parameters. Typically, the surface voltage of electrified film is close to the grid voltage. To achieve a large uniformly charged area, relatively large needle-electrode distance, small grid-electrode distance, large needle-grid distance, relatively high needle voltage, and relatively long charging time more than 20 seconds are desirable.

The front and back sides of corona charged polymer films usually share similar magnitude but opposite polarities of surface voltage. The surface voltage on each side decays over time, while the ratio of the voltmeter-measured surface voltage to the fieldmeter-measured voltage difference is nearly constant, independent of film material, charging condition, voltage decay rate, and time. This phenomenon can be explained by the dipolar charge injection model.

A small variation in surface density of free charges, as small as ~0.1% of the surface density of dipolar charges, may drastically change the absolute value of surface voltage and sometimes, even the polarity. The amount of free charges and the associated surface voltage can be tailored through contact electrification (CE), for which the key parameters include the film material, the liquid composition, and the external electric field. Contact electrification can be applied on either neutral or electrified films. By combining corona charging (CC) and CE, we can precisely control the surface voltages of polymer films. As the surface density of CE-induced free charges is much smaller than that of CC-induced dipolar charges and the latter is inherently more stable, the decay rate of free charges is much faster and the dipolar component of charge distribution is much more stable. The change in voltage difference across the film thickness is often negligible.

Chapter 1 Introduction

1.1 Energy efficiency of building windows

1.1.1 Heat loss through windows

According to the Buildings Energy Data Book,[1] in 2015 the U.S. building energy end-use was 39.26 quads, nearly 40% of the total energy consumption in the U.S.[2] Among the 39.26 quads energy, space heating accounts for 21.5% (8.45 quads) and 11.8% (4.63 quads) is for space cooling.[1, 3] About 53% of the 13.08 quads energy use of building heating and cooling is lost through building windows, with an estimated overall average U-factor of 0.75 $Btu \cdot hr^{-1} \cdot ft^{-2} \cdot °F^{-1}$ for all residential buildings.[3]

If Energy Star windows, most of them are enhanced double-pane windows, are fully put into use (U-factor: Northern ≤ 0.27, Central ≤ 0.30, Southern ≤ 0.40 in the U.S.),[4] there will be ~2 quads energy saving for building heating and ~1.5 quads for building cooling per year in the U.S.[5] However, 30~40% windows around the world are still single-pane windows, with U-factor around 1.2 $Btu \cdot hr^{-1} \cdot ft^{-2} \cdot °F^{-1}$.[3] They are inefficient for thermal insulation, and currently consuming a major portion of the energy wasted through non-Energy Star windows (~3.5 quads).[6] Replacing or upgrading single-pane windows are expensive and slow. The cost for replacing single-pane windows to Energy Star windows is $800~$1500 per square meter,[7, 8] approximately

$15,000 per household. Fully replacing single-pane windows may take as long as 4 decades.[3]

Retrofitting single-pane windows offers an attractive alternative solution. Compared with replacing windows, retrofitting is much more economical, faster, and less labor intensive. Desirably, a window retrofitting technique should be low-cost and easy to operate; the retrofitted window should has low emissivity (low-e), low overall U-factor (<0.5); long service life (>10 years); high visual transmittance (V_t) (>70%) and low haze (<1%); and high color rendering index (>0.9).[9]

1.1.2 Double-pane and single-pane windows

Heat transfers across windows consist via conduction, convection, and radiation, approximately accounting for 50%, 35%, and 15% of total transported thermal energy, respectively.[10] Currently, the most popular energy-efficiency windows are double-pane or triple-pane windows with low-e coatings. To suppress conductive heat transfer, the gaps in between glass panes are typically filled with air or Argon (Ar) gas. The gap thickness is typically 8~20 mm, taking advantage of the low thermal conductivity of air (0.0262 $W \cdot m^{-1} \cdot K^{-1}$) or Ar (0.0179 $W \cdot m^{-1} \cdot K^{-1}$).[11]

Note that a large gap thickness promotes convective heat transfer. When the gap is thicker than ~8 mm, air/Ar convection can be fully developed. When the gap thickness exceeds ~20 mm, convective heat transfer becomes more pronounced than heat conduction and therefore, further increasing gap thickness would not lead to any significant improvement in U-factor.

To reduce radiative heat transfer, low-e coating functions as a wavelength selector. It reflects long-wavelength radiation in the inferred (IR) domain while allows visible light to pass through. The windows can block 70%~80% of heat radiation from outside during summer and retain a large portion of heat from inside during winter. Low-e treated windows can also block ~92 % of damaging UV light, control glare, and provide day lighting.[12-14] A major issue of low-e coating is water condensation.[15] If the window coating is covered by a layer of water, heat absorption and conduction would be dominant and the low-e effect becomes negligible.

1.2 Improved thermal management of building windows

1.2.1 Storm windows

Storm window is an add-up layer mounted either outside or inside of the existing window. It is a lower-grade cost-effective retrofitting approach, compared to replacing the entire window. Storm window panes can be made of inexpensive plastic sheets for short term use, or high-end triple-track glasses with low-e coatings for long term use. Storm window frames are usually made of wood, aluminum (Al), engineering plastics, etc. Storm windows possess advantages of low cost, no window replacement, and easy installation.

However, once installed, many storm windows cannot be opened; the frames are heavy and must be customized to the same size of the original windows. Moreover, storm window offers less energy efficiency, compared to double-pane windows; it needs

more maintenance; and serious inner condensation may happen.[16-18] If a lighter, frameless structure can be mounted directly on glass pane, most of these issues may be circumvented.

1.2.2 Thermal insulation materials

Coating highly thermal insulating, highly transparent materials onto glass panes is another way to decrease the U-factor of windows. Aerogel is an important candidate currently under extensive investigation.[19] It is a highly porous solid, usually synthesized through so-gel methods. Silica aerogels can reach an ultralow thermal conductivity around 0.012 W/(m·K), a visual transmittance more than 99%, and a reflective index as low as 1.05.[20] It inhibits convective heat transfer as the pore size is much less than the surface layer thickness. It considerably nullifies thermal conduction due to the large porosity and the beneficial Knudsen effect:[20]

$$\lambda_g = \frac{\lambda_{g,0}}{1+2\xi K_n} \qquad \text{(Eq. 1.1)}$$

where λ_g is the thermal conductivity of gas phase in nanopores; $\lambda_{g,0}$ is the conductivity of bulk gas phase; ξ is a constant between 1.5 and 2.0; and K_n is the Knudsen number, defined as

$$K_n = \frac{k_B T}{\sqrt{2}\pi d_g^{\,2} P_g \delta} \qquad \text{(Eq. 1.2)}$$

where K_B is the Boltzmann constant, T is temperature, d_g is the diameter of air molecules, P_g is the gas pressure, and δ is the pore size. However, aerogel is inefficient in blocking

radiation; its synthesis may be relatively time consuming, and has difficulties in scaling-up. Most critically, silica aerogel is inherently fragile, with the flexural strength merely a fraction of 1 MPa.[21] Typical strengthening processes and additives would reduce the visual transmittance or the thermal insulation properties.[20, 22-25]

1.2.3 Low-emissivity films

Applying low-emissivity (low-e) films on glass panes offers a relatively cost-efficient method to reduce radiative heat transfer across widows in the important infrared (IR) domain. As IR radiation reaches a window pane, the incident energy (E_i) equals to the summation of the absorbed energy (E_a), the transmitted energy (E_t), and the reflected energy (E_r). Kirchhoff's law of thermal radiation states that the emitted energy (E_e) should be the same as the absorbed energy.[26] Thus, $E_i = E_e + E_t + E_r$. In the IR range, transmission of most materials is quite low; that is, $E_i \approx E_e + E_r$. Consequently, lowering the emissivity can increase the reflectivity to reduce heat transfer.[27] A commonly used low-e coating material is silver, together with oxide layers for adhesion and protection. The emissivity of a coating layer (ε) can be assessed by the Hagen-Rubens Relation[28]

$$\varepsilon \approx 4\sqrt{\frac{f}{\kappa_e}\pi\varepsilon_0} \qquad \text{(Eq. 1.3)}$$

where f is the frequency of light, κ_e is the electric conductivity, and ε_0 is the permittivity of empty space. It can be seen that a higher κ_e leads to a lower emissivity.[12, 29] In addition to highly electrically conductive metals such as silver, other low-e coating

materials include indium tin oxide (ITO),[30] doped zinc oxide [12], etc. The major technical hurdles for low-e films are the relatively high cost, the poor visual transmittance, and the complicated installation process. Very often, low-e coating alone cannot lead to the desired U-factor, since low-e films do not mitigate conductive or convective heat transfer.[31-33] Moreover, the low-e effect on reduction in heat transfer can be largely reduced if water condensation is formed on either side of the low-e coated window, as conductive heat transfer becomes dominant.

Table 1.1 Comparison of advanced multilayer low-e coatings [34-37]

Low-e multilayers	Visible transmittance (%)	Emissivity (%)
Glass-ZnO-Ag-$TiAO_x$-SnO_2	86	10
Glass-SnO_2-Ag-$NiCrO_x$-SnO_2	84	15
Glass-SnO_2-TiAOx-Ag-TiAOx-SnO_2	84	12
Glass-$SnBO_2$-ZnO-Ag-NiCrOx-$SnBO_2$	85	9
Glass-Tungsten Oxide-Ag-Silicon buffer-Tungsten Oxide	86	10
PET-TiO_2-ZnO:Ga-Ag-ZnO:Ga-TiO_2	80	10

1.3 Our concept: polymer-air multilayer (PAM)

Recently, we investigated a novel thermal insulating structure: polymer-air multilayer (PAM). PAM is constructed by placing a few transparent polymer films in parallel, stably separated by air gaps. The air gap thickness is below 1 mm, so that convective heat transfer is trivial. Because the polymer films are highly transparent,

mechanically robust, and low-cost, PAM circumvent most of the issues of other thermal insulating coating materials. In a typical PAM, the layer count is 4~8 and the polymer film thickness is ~100 μm. More analyses of thermal performance of PAM will be given below.

1.3.1 Radiative thermal transfer

Multilayer insulation (MLI) structures have been used for decades in a variety of areas.[38] For instance, NASA has been using multilayer insulation in spacecraft and satellites. A MLI usually consists of a large number of foils loosely packed together. At each foil surface, heat radiation is partly blocked. It works particularly well in vacuum, as convective heat transfer does not occur and conductive heat transfer takes place only across the contact areas of adjacent foils. The layers in MLI structure are usually made by low emissivity heat reflection materials, such as aluminum (Al) and silver (Ag), with the emissivity of only ~0.04.[39] Thin netting spacers, which may be made of thin polymers, can be added in between the heat reflection layer to offer structure stability and suppress thermal contact. The overall heat transfer coefficient, *U*, can be calculated as:[40, 41]

$$U = \frac{4\sigma_0 T^3}{N(2/\varepsilon - 1) + 1} \qquad \text{(Eq. 1.4)}$$

where $\sigma_0 = 5.7\times10^{-8}\,\mathrm{W\cdot m^{-2}\cdot K^{-4}}$ is Stefan-Boltzmann Constant, T is temperature, N is the layer count, and ε is the layer emissivity.

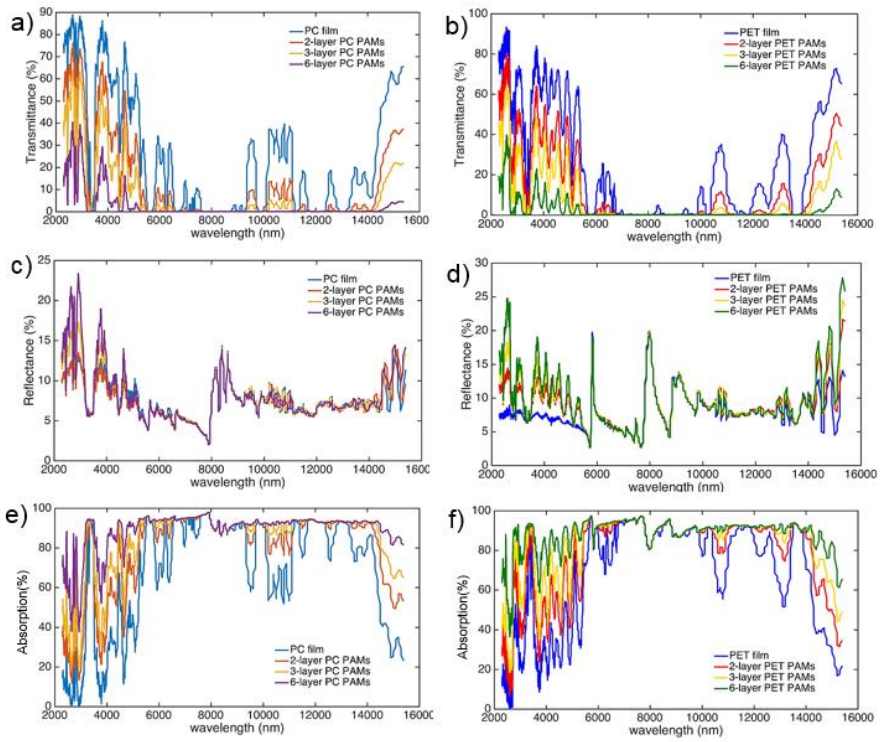

Figure 1.1 IR spectral transmittance, reflectance, and emissivity of PC and PET based PAM at 300 K. a) IR transmittance of PC-based PAM. b) IR transmittance of PET-based PAM, c) IR reflectance of PC-based PAM, d) IR reflectance of PET-based PAM, e) IR absorption of PC-bsaed PAM, f) IR absorption of PET-based PAM. Each PAM is 1×1 inch large, consisting of a few 125-μm-thick PET or PC films separated by 500-μm-thick spacers at the edges. The spacers are constructed by 2 mm-wide PC strips. The PET and PC films were obtained from McMaster-Carr. They have been thoroughly cleaned with Isopropyl alcohol and water.

According to our measurement at 300 K (Figs. 1.1 and 1.2), for a single layer of polyethylene terephthalate (PET) or polycarbonate (PC) film, the IR transmittance is about 15%. That is, the reflectance of a PET or PC film is ~8%; the rest (~77%) is absorptivity, which is equal to emissivity. The total IR heat flux blocked by the film includes the contribution from reflection (~8%) and a half of absorbed thermal energy (~38%), i.e. ~46% of incident heat flux. Therefore, the effective emissivity of a single PET or PC film is ~0.54. By using this value in Eq. 1.4, it can be assessed that with 2 to

6 layers of polymers, the overall effective emissivity of PAM would be 0.32, 0.22, 0.17, 0.12, and 0.11, respectively.

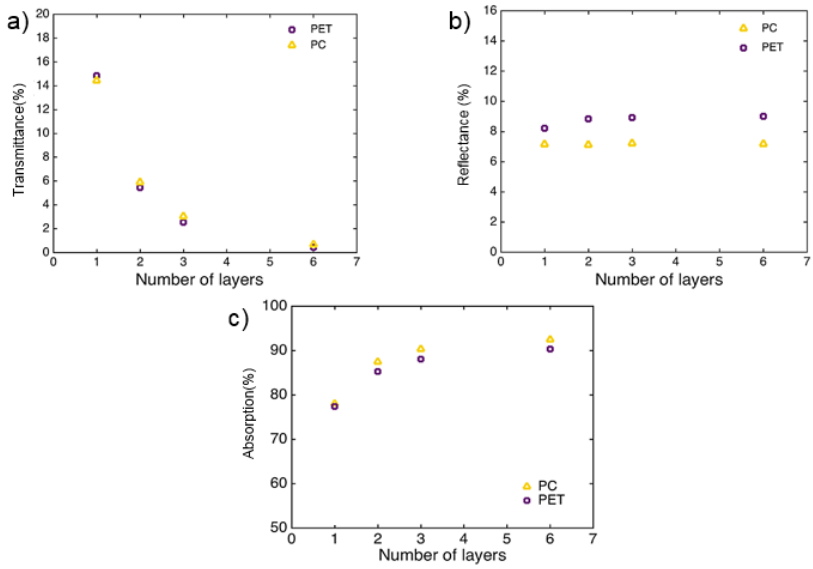

Figure 1.2 Blackbody spectrum weighted IR: a) transmittance, b) reflectance, and c) absorption of a single PET or PC film. Each film is 1×1 inch large and 125 μm thick. They have been thoroughly cleaned with isopropyl alcohol and water. The films are separated by 2-mm-wide 500-μm-thick PC spacer.

1.3.2 Convective heat transfer

In addition to suppression of heat radiation, PAM also significantly limits convective heat transfer. The Nusselt number (*Nu*) represents the ratio of convective to conductive heat transfer and can be calculated by Eq. 1.5:[42]

$$Nu = \frac{\text{Convection}}{\text{Conduction}} = f\left(\frac{g\beta(T_w - T_0)b^4}{\nu\alpha L}\right) \qquad \text{(Eq. 1.5)}$$

where g is the acceleration of gravity, β is the thermal expansion coefficient of air, T_ω is the surface temperature, T_0 is the ambient temperature, b is the air gap thickness, ν is

the kinetic viscosity of air, α is the thermal diffusivity of air, and L represents the size of window. As shown in Figure 1.3, when the air gap thickness is ~10 mm, Nu=1; when the air gap thickness is 20 mm, the convection effect is 2.3 times greater than the conduction effect and becomes the dominant factor. When the air gap thickness is 0.6 mm, the convection effect is only 0.4% of conduction, at the negligible level. Hence, by using PAM with the air gap thickness less than 1 mm, we are able to reduce the Nusselt number below 1.2%.

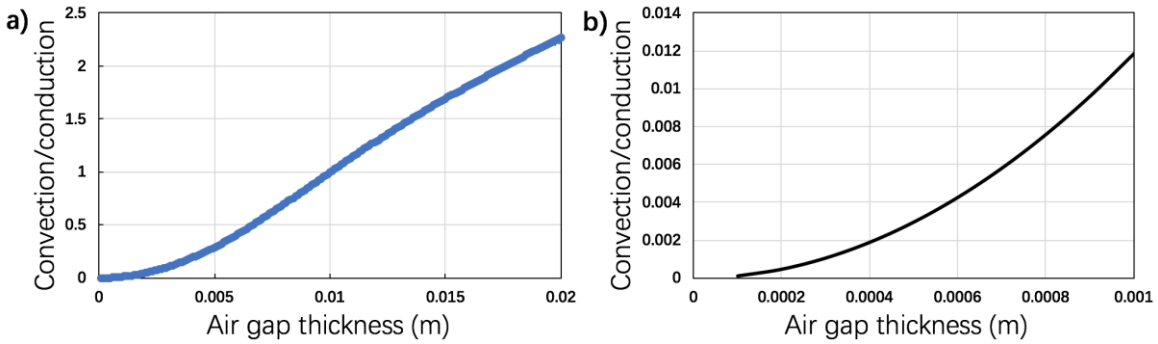

Figure 1.3 Ratio of convective to conductive heat transfer for different air gap thickness ranges: a) 0~20 mm, b) 0~1 mm.

1.3.3 Conductive thermal transfer

In a PAM, when the polymer layers are much thinner than the air gaps, the majority of PAM volume is occupied by air, so that the air phase dominates the overall thermal conductivity. The effective thermal conductivity of PAM, k_{PAM}, can be modeled as a series of thermal resistors of polymer and air layers:

$$k_{PAM} = \left(\frac{t_a}{k_{air,eff}} + \frac{t_p}{k_p}\right)^{-1}(t_a + t_p) \qquad \text{(Eq. 1.6)}$$

where K_p is the thermal conductivity of polymer, typically in the range from 0.2~0.4 $W \cdot m^{-1} \cdot K^{-1}$;[43] and t_a and t_p are the thicknesses of air gap and polymer films, respectively.

The effective thermal conductivity $k_{air,eff}$ depends on the thickness of the air gap, with the convection effect being taken into consideration. It can be assessed as[44]

$$k_{air,eff} = \frac{15\rho(2RT_0)^{3/2}b}{16D + 28\sqrt{\pi}} \quad \text{(Eq. 1.7)}$$

where ρ is the air density, R is the gas constant, T_0 is the average temperature, b is air gap thickness, and D is the inverse Knudsen number ($D=b/MFP$).

The calculated thermal conductivity of PAM is shown in Figure 1.4, where we assume k_p = 0.2 $W \cdot m^{-1} \cdot K^{-1}$. When the polymer thickness is below 175 μm and the air gap thickness is above 400 um, the overall thermal conductivity can be less than ~0.03 $W \cdot m^{-1} \cdot K^{-1}$, close to the air thermal conductivity.

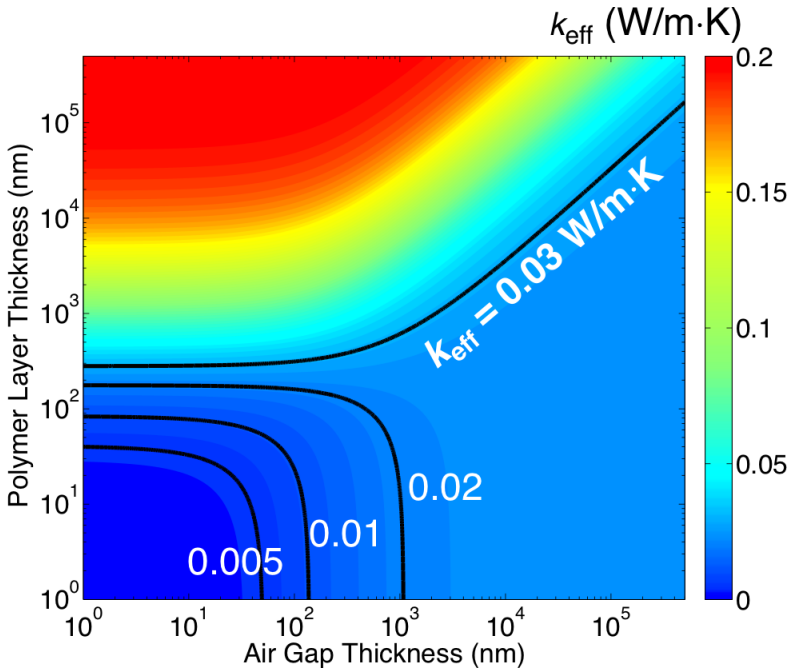

Figure 1.4 Contour plot of thermal conductivity of PAM.

1.3.4 Calculation of U-factor

As PAM suppresses all the heat transfer mechanism – heat radiation, convective heat transfer, and conductive heat transfer, when a thin PAM is coated on a glass pane, it may lead to a low U-factor. The center-of-glass U-factor can be modeled as a series of thermal resistances h_i^{-1}, RPAM, and h_0^{-1}; the U-factor is the reciprocal of the total thermal resistance and can be expressed as

$$U_{cg} = \left[h_i^{-1} + \frac{k_{PAM}}{t_{total}} + h_0^{-1} \right]^{-1} \quad \text{(Eq. 1.8)}$$

where h_i and h_0 are the heat transfer coefficient at the outer and inner glazing surfaces, respectively. A U-factor ~0.5 can be reached by a PAM with the total thickness of 3 mm, for which the polymer layer thickness is 175 μm and the air gap thickness is 575 μm. Compared to double-pane windows or storm windows, PAM is highly transparent, highly robust, and low-cost. A 3-mm-thick PAM is thin (space saving), lightweight, and easy to install. It will have a profound impact to the single-pane window retrofitting industry, and may also significantly influence the industry of double-pane window manufacturing and installation.

Compared to aerogels, PAM has a similar overall thermal conductivity yet much improved structural integrity, higher robustness, higher visual transmittance, and lower haze; it is also friendlier to mass production. Compared with low-e coatings, PAM offers excellent thermal insulation by blocking all three heat transfer processes, and is insensitive to water condensation.

1.4 Stabilization of Air Gaps in PAM

A key feature of PAM is that the polymer films are entirely separated by air gaps. While a few % of solid supports may not much affect the U-factor, they would reduce visual transmittance and are desirable for window coating applications. To suppress convective heat transfer, the air gap thickness must be small, below 1 mm. Maintain high stability and high resilience of the air gaps is a critical task for PAM development, for which magnetic and electronic forces offer two possible non-contact approaches.

1.4.1 Magnetic mechanism

Magnetic fields have been widely employed in a large number of areas, e.g. repulsive-force magnetic levitation (maglev) suspension systems, repulsive-type magnetic bearing systems, magnetic separators,[45] stable suspension of magnetic nanoparticles,[46] etc. Permanent magnets or electrical magnets must be involved to generate the repulsive forces.[47, 48]

For the PAM application, if the magnetic force is created by permanent magnets, the magnet components need to be embedded into the polymer layers, and their sizes must exceed the superparamagnetic thresholds.[49] However, the magnetic fillers would harm the visual transmittance of PAM; to offer repulsion forces, the magnets have to be precisely aligned; the bonding strength between the magnets and the polymer phase may not decay over time.[50] In addition, the repulsive forces are based on electromagnetism, an electrical power supply must be connected to the PAM continuously. These hurdles

render the magnetic mechanism less competitive than the electrification mechanism, discussed below.

1.4.2 Electrification mechanism

According to Coulomb's Law, the electric force between two point charges q_1 and q_2 is:[51]

$$F = \frac{kq_1q_2}{r^2} = \frac{q_1q_2}{4\pi\varepsilon_0 r^2} \quad \text{(Eq. 1.9)}$$

where ε_0 is the permittivity of the space, $k = 9\times10^9\ \mathrm{N\cdot m^2\cdot C^{-2}}$ is Coulomb's constant. Like charges repel each other.

Electrostatics-related techniques have been quite mature. For instance, corona charging is used to separate conductive and non-conductive materials;[52] tribo-charging is applied for separation and purification;[53] surface electrostatics can promote size selection,[53] uniform coating,[54] waste recycling,[52] etc.

Electrostatic stabilization, which utilizes the repulsion force between like-charged objects, is one of the most commonly used techniques for particle dispersion.[55-57] Another related phenomenon is the electrical double layer force between charge objects across a liquid medium.[58] Usually, the repulsion force increases with the charge density and decays exponentially with the distance.[58, 59]

Electrostatic separation of layered materials has been reported for anisotropy composite manufacturing[60] and energy harvesting.[61, 62] We hypothesize that by taking advantage of the repulsion force between likely charged polymer layers, the air gaps in

PAM can be stabilized, for which the science underpinning polymer electrification must be deeply understood.

1.5 Polymer electrification

If a polymer is sufficiently electrically insulating, it may permanently or quasi-permanently hold electric charges or/and dipolar polarization. Such electrified polymers have long been known as polymer electrets.[63] The manufacturing approaches and the applications of polymer electret were extensively investigated in the past a few decades,[64] yet the fundamental mechanisms and processes are still relatively poorly understood.

Based on their manufacturing approaches, polymer electrets can be classified as space-charge electrets (thermoelectrets), corona electrets, e-beam electrets, photoelectrets, radioelectrets, and mechanoelectrets,[64] as shown in Figure1.5 Electrified polymers have been widely applied for printing,[65] coating and surface treatment,[66] absorption and adsorption,[67] biomedical devices,[56] transducers,[68] electrophotography,[69] recording,[70] advanced filtration,[71] motors and generators,[72] dosimeters,[73] pyroelectric devices,[74] microphones,[64] energy harvesting,[54] etc. Figure 1.6 depicts the major charging mechanisms.

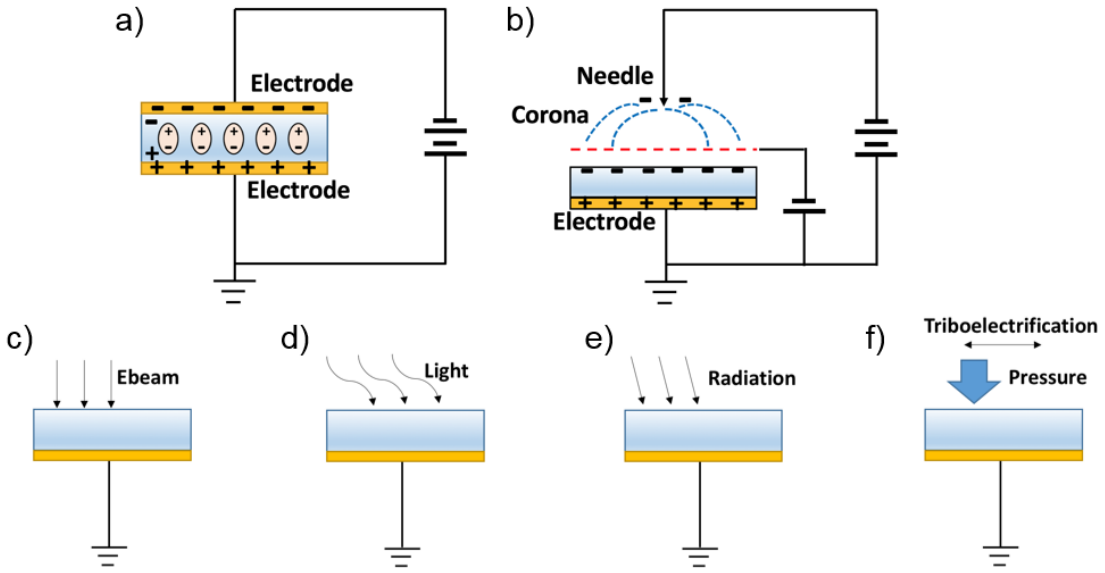

Figure 1.5 Polymer electrification: a) Space charging electrets, b) corona charging, c) e-beam charging, d) photo-charging, e) radio-charging, and f) triboelectric-frication.

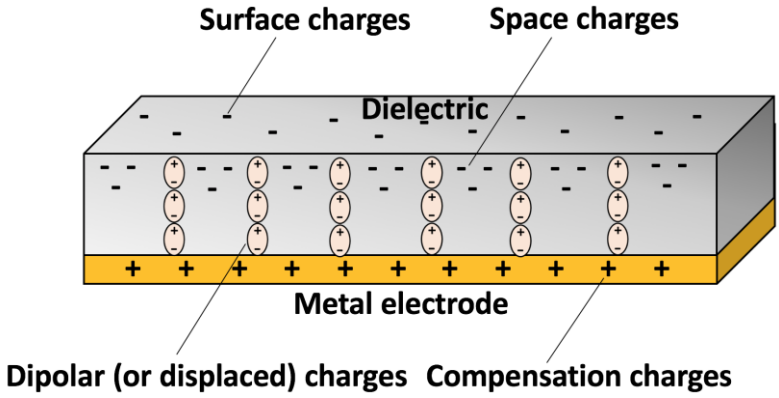

Figure 1.6 Schematic of polymer electrets

1.5.1 Space charging

Space charging, also known as thermo-charging, in which, a polymer film is sandwiched by two electrodes, across which a high voltage is applied (Figure 1.5a). The processing temperature is around the glass transmission temperature of the being

electrified polymer.[75] It is most relevant to polymers with polar groups. The polymer film is softened or melted in the strong electric field, often aided by heating elements, and the polar groups are aligned as dipoles. As the material is cooled down and solidified, the dipolar potential distribution can be stably maintained.[76]

The polarization density $\boldsymbol{P}$ can be stated as

$$\boldsymbol{P}=\varepsilon_0\chi_e\boldsymbol{E} \quad \text{(Eq. 1.10)}$$

where ε_0 is the vacuum permittivity and χ_e is the dielectric susceptibility. Collectively, $\varepsilon_0\chi_e$ determines the tendency of the material to be polarized, and χ_e is

$$\chi_e=\varepsilon_r-1 \quad \text{(Eq.1.11)}$$

where ε_r is the relative permittivity. The electric displacement field $\boldsymbol{D}$ is

$$\boldsymbol{D} = \varepsilon_0\boldsymbol{E}+\boldsymbol{P} = \varepsilon_0\boldsymbol{E}(1+\chi_e) = \varepsilon\boldsymbol{E} \quad \text{(Eq. 1.12)}$$

where, $\varepsilon= \varepsilon_0\,\varepsilon_r$ is the permittivity and $\varepsilon_r=1+\chi_e$. For an isotropic medium, ε is a constant; it is a tensor related to position inside of the material for an anisotropic medium. Note that ε is also dependent on the electric field and time.[64]

Polymers that have been thermo-charged include poly(methyl methacrylate) (PMMA), fluorinated ethylene propylene (FEP), high density polyethylene (HDPE), low density polyethylene (LDPE),[75] polyethylene terephthalate (PET),[77] perfluoroalkoxy alkane (PFA),[75] polycarbonate (PC), polyimide (PI),[78] polyphenylene sulfide (PPS),[75] polytetrafluoroethylene (PTFE),[79] polyvinyl dine-fluoride (PVDF),[80] etc. For instance, to charge PVDF film, an electric field of 2 $MV\cdot cm^{-1}$ is needed at 80~120 ºC.[80] If the polymer film is in direct contact with the electrode surface, in additional to the dipole orientation, there would be injected charges, as shown in Figure 1.6.

1.5.2 Corona charging

Corona charging, also known as corona discharge, is another important electrification method of polymer surfaces.[81] Corona is usually generated at a highly curved surface of high-voltage electrode. The large potential gradient breaks down the surrounding air and ionizes the air molecules. The ionization energy is usually 1~3 eV.[82] The ions are accelerated and separated in the electric field, and collide and further ionize nearby air molecules, leading to electron/ion "avalanches". The ion mobility is in a few $cm^2 \cdot V^{-1} \cdot s^{-1}$.[83]

Corona can be positive, which launches positive ions and attracts electrons; or negative, which launches electrons and attracts positive ions. A corona charging system typically consists of a needle-electrode connected to a high voltage power supply and a grounded electrode plate (Figure 1.5b).[84] A polymer film is placed on the grounded electrode, with the upper surface exposed to the corona. When a polymer surface is treated by corona charging, the electrons/ions are injected into the polymer. The polymer must have a very high electric resistivity, so that the injected charges are trapped locally without escaping, neutralization, or transferring.[85] Very often, a grid can be added in between the needle-electrode and the grounded electrode to form a triode charging system for better control the corona configuration.[86]

It is generally acknowledged that the mechanism of corona charging is complicated.[87] Classic corona charging models include: 1) the polarization model, capturing the dipole alignment/polarization in polar polymers;[88, 89] and 2) the charge injection model, capturing the motion of charge carriers from the surface into the bulk.[90]

The polarization model is somewhat similar with the space charging process. Polarizing electric field is offered by the corona and/or the accumulated surface charges.[88, 89] Thus, inverse dipoles are generated. In the charge injection model, the charges are from the corona, and the driving force of charge injection is from the electric field of the corona and/or the accumulated surface charges. The charge injection may happen at only one side or on both sides of the film.[90] Amorphous or semi-crystalline macromolecules and impurities, defects, and crystalline-amorphous interfaces can trap the injected charges.[91] As the polymer is sufficiently resistant to charge motion, the trapped charges would remain in the surface zone and build up an electric field. In contrast to the polarization model, the polarity of the electrified film predicted by the charge injection model is the same with the corona.

In a single polymer film, multiple electrification processes can take place simultaneously. Contribution from dipole orientation may increase with the charging temperature.[92] As polarities caused by polarization and charge injection are opposite to each other, there may be a critical condition at which the overall electrification effect is minimized. The dominate charging mechanism may vary with the material.

The decay of surface voltage of electrified polymer film is another important phenomenon. It is a complex procedure that may involve surface conduction,[91] volume conduction,[93] atmospheric neutralization,[94, 95] external charge injection,[96] electric field polarization,[97] humidity and contamination attraction,[98] among others. To manufacture polymer electrets with stable surface voltages, it is imperative to systematically examine the effects of key parameters on the surface-voltage decay rate. Such parameters include polymer material,[99, 100] film thickness,[101] charging voltage

and temperature,[102, 103] working environment,[98] etc. In addition to directly monitoring the surface potential of the charged films with voltmeter,[95] other experimental approaches such as thermal stimulated discharge (TSD),[104, 105] pulse electro acoustic (PEA),[106] and laser induced modulation (LIMM) [107] have been developed to precisely measure the charge distribution. These technologies may have tight requirements on materials properties and charging/discharging conditions.[85]

Corona charging is currently being broadly used in the polymer industry to improve surface adhesion, increase surface roughness, add oxygen-containing functional groups, enhance hydrophilicity, etc.[67] Compared to space charging, a wider range of polymers are capable of being corona charged, as it can electrify both polar and non-polar materials, e.g.: silica,[75] PMMA,[108] FEP,[109] HDPE,[110] LDPE,[81] PET,[98, 111] PFA,[112] PC,[113] PPS,[114] PTFE,[102, 115] PVDF,[109] acrylonitrile-butadiene-styrene (ABS),[116] chlorotri-fluoroethylene (CTFE),[117] polyvinyl formal (Formvar),[118] polyamide (Nylon), polybutylene terephthalate (PBT), polyetheretherketone (PEEK), polyetherimide (PEI),[119] polyimide (PI),[63] polypropylene (PP),[102] polystyrene (PS),[118] polyvinyl chloride (PVC),[120] styrene acrylonitrile (SAN),[121] ultra-high molecular weight polyethylene (UHPE),[122] etc. Porous polymer films, such as porous PP, PTFE, and PVDF films, can also be electrified.[79, 123, 124]

1.5.3 Comparison between space and corona charging

Table 1.2 compares space charging and corona charging methods. The advantage of space charging includes the high stability of surface voltage, since

polarization is achieved in the bulk volume; disadvantages include the non-uniformity of lateral charge distribution and the time-consuming softening/melting and solidify of polymer. Moreover, the surface structure may be damaged by the softening/melting process, which is unacceptable for transparent polymer films. It is only relevant to polar thermoplastics.

The corona charging method is simple and fast; use of heating element is optional. It can charge not only polar polymers, but also non-polar ones, as well as ceramics and glasses. The surface damages are usually invisible.

Table 1.2 Comparison between space charging and corona charging

	Space charging	Corona charging
Number of plate electrodes	2	1
Temperature	$T>T_g$, close to T_m	Any
Voltage/Electric field	Up to 200 MV/m (5kV/50 um)	Needle: 4kV~30 kV Gird: 200 V~3000 V
Major mechanism	Dipole alignment	Charge injection
Polymer type	Polar	Any
Charging time	Minutes to hours	Seconds to minutes
Surface condition	Thermal damage and breakdown	Minor chemical or physical changes, usually invisible

1.6 Contact electrification

Contact electrification (CE), also known as triboelectrification or static electrification, has been discovered for more than 2500 years; it is yet another process

through which a polymer can be electrified.[125] When two objects contact with each other, charge transfer may occur across the interface and after they are separated, both surfaces would have net charges. CE can happen between conductors, semiconductors, and insulators; the materials can be in liquid, gas, or solid phase.[126, 127] The contact-induced charges on a conductor dissipate rapidly, but the charges in insulators would remain, resulting in high surface voltages. [128, 129] Triboelectric series rank materials based on their empirically derived direction of charge transfer (Figure 1.7).[125] For instance, when silk is contacted with Teflon, silk will be charged positively and Teflon will carry negative charges. However, such orders can be altered by a number of factors, such as temperature, friction mode, etc. CE can also happen between nominally identical materials.[130]

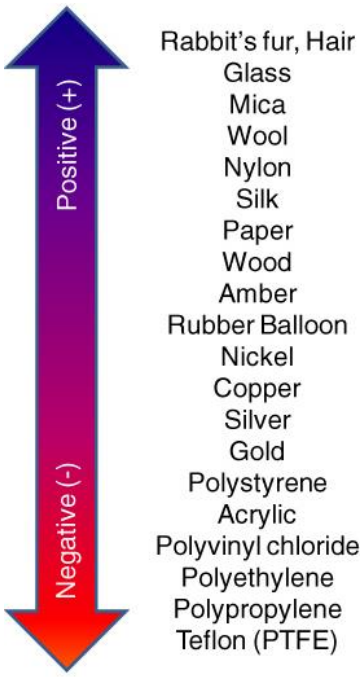

Figure 1.7 Experiential triboelectric series showing the direction of charge transfer.[125]

The understanding of the science underpinning contact electrification is still quite limited. Electrostatic charging, due to the complicated charge transfer/trapping processes and the large number of system variables, have many "unpredictable" aspects.[131] Usually, CE is explained as electron exchange, ion exchange, materials exchange, etc.[132-134]

Thanks to the high voltage and sometimes its high stability, CE has been applied in a large number of engineering areas, including photocopying, laser printing, electrostatic separations, transistors, to name a few.[133, 135] Recently, CE based energy harvesting devices received increasing attention, e.g. the systems based on dielectric polymers and water.[136, 137]

As we use polymer films to construct PAM, CE is inevitable. The surface voltages of electrified polymers must be controlled in a desired range, so as to keep the solid layers stably separated.

1.7 Outline of thesis

As discussed above, PAM may offer a promising solution of advanced thermal insulation, and find wide applications, e.g. for single-pane window retrofitting. PAM not only blocks heat radiation, but also reduces conductive and convective heat transfer. It has excellent cost-performance balance, high visual transmittance, low haze, and is lightweight.

In order to develop robust and resilient PAM structures, the air gaps among the polymer layers must be stably separated, especially for large-sized PAM with large layer

count. In the current study, we will focus on corona charging of polymer layers. It is envisioned that as polymer layers are permanent electrified, without affecting the visual transmittance, strong repulsive forces can be generate between like-charged polymer surfaces. To precisely control the system performance, the fundamental science must be systematically investigated.

In Chapter 2, we discuss the corona charging system that we constructed as well as the experimental methods. All the critical parameters are adjustable, offering the opportunity for a comprehensive study on the details of polymer electrification process.

In Chapter 3, we examine the dipolar component of charge distribution in corona-charged polymer films. Its stability and the influences of polymer properties, temperature, film thickness, and electrode voltage are analyzed in detail.

In Chapter 4, contact electrification between a variety of polymer films and liquids is investigated. The effects liquid composition on the charged state of polymer surface are tested under various conditions.

In chapter 5, based on the research in Chapters 3 and 4, we develop a novel approach to precisely control the surface voltage of electrified polymer. Specifically, free charge and dipolar charge components are adjusted quite independently.

In chapter 6, we present our conclusions and considerations of future work.

1.8 Acknowledgement

The thermal calculation in Section 1.3 are conducted by Professor Renkun Chen, Dr. Edward Dechaumphai, and Ms. Yun Zhou.

Chapter 2 Corona charging: system and key parameters

2.1 Introduction

Corona treatment has drawn much attention since it was first investigated by Verner Eisby in 1951.[138] In addition to the early applications related to adhesion and coating enhancement,[139] corona charging is currently being widely employed to manufacture electrets,[71] as key components for transducers,[68] electrophotography,[69] recording,[70] advanced filtration,[71] motors and generators,[72] dosimeters,[73] piezoelectric devices,[74] microphones,[64] energy harvesting systems,[54] among others. Compared to many other charging approaches,[76] corona charging is highly efficient, causes noun or only minor chemical or physical changes of polymer surfaces,[66] can be operated in a wide range of temperature, [140] and can treat most of dielectric materials.[141]

In general, because of the large potential gradient around a charged point or wire, air can be broken down and ionized. The ions are accelerated and separated by the strong electric field, leading to collision and electron avalanches.[142] Corona can be positive, by launching positive ions and attracting electrons; or negative, by repelling electrons from the launching point and attracting positive ions by the plate electrode. [84] The ionization energy is typically in the range of 1~3 eV.[82]

Early corona charging system consisted of only a corona point, a grounded plate electrode, and a high-voltage power supply. In such a system, the area and the

uniformity of charged surface cannot be well controlled.[83] Moreno and Gross developed triode corona charging system, by inserting a metallic grid in between the corona point and the grounded electrode. The grid much improves the uniformity and the controllability of the charging effects.[96] Usually, the grid is connected to a separate power supply with the same polarity but a lower voltage than the one charging the corona point. The surface voltage on charged sample tends to be uniform and equivalent to the grid voltage.[96] According to necessity, multiple corona points[89] or wire corona generators[143] can be used, to increase the charging area; the detailed electrification process of constant-current triode corona system can be better monitored. Literature data showed that silica,[75] PMMA,[108] FEP,[109] HDPE,[110] LDPE,[81] PET,[98, 111] PFA,[112] PC,[113] PPS,[114] PTFE,[102, 115] PVDF,[109] ABS,[116] CTFE,[117] Formvar,[118] polyamide, PBT, PEEK, PEI,[119] PI,[63] PP,[102] PS,[118] PVC,[120] SAN,[121] UHPE,[122] CYTOP,[144] piezoelectric porous PP,[145, 146] PTFE,[79] and PVDF[147, 148] have been successfully corona charged.

Corona discharging is complicated. A number of processes and mechanisms have not been fully understood. Particularly, there has not been a well-defined framework that can account for the effects of important processing parameters, such as the needle potential, the grid potential, charging time, and the polymer material. Cui et al. used 10 kV and 0.3 kV as needle and grid voltages, respectively, to charge PMMA for 2 min at 120 ℃;[140] the highest voltage that Stalk et al. used to charge FEP and PVDF films was 6 kV;[109] it was reported that PET was charged at -10 kV, -8 kV, or -6 kV by Rouagdia et al.[98] Charging time often varies from seconds to hours.[89, 149] The stability of the potential of the electrified surface is remarkably dependent on the initial

voltage,[150] humidity,[85] material,[95, 106] and temperature[102, 104]. A deeper understanding of these parameters can be greatly beneficial to the optimization of corona charging systems and operation. The initiating voltage and the applicable voltage range should be adjusted to minimize the power consumption; the component distance should be decoupled with the voltage setting for complex triode procedures.

In this chapter, we focus on the effects of key corona charging parameters. The potential distribution of samples charged by needle-plate corona system was mapped, to identify the corona initiate voltage, to trace potential distribution and its dependence on needle voltage, and to understand the influence of needle-plate distance. A grid was then utilized to build a triode corona system and the influence of grid and needle voltages, grid-electrode distance, grid-needle distance, charging time were examined. The controllability and uniformity of charging with grid were analyzed. Three different polymers were investigated.

2.2 Experimental

2.2.1 Corona charging system

A corona charging system (Figure 2.1) was built up to electrify selected polymer films. The setup consisted of a discharging needle electrode, an optional wire mesh grid, a grounded electrode, heating elements, and two high voltage power supplies. A sharp tungsten needle 0.75-inch-long and 0.059 inch in diameter was employed as the discharge needle electrode. The curvature of the needle tip was ~0.1 mm. A grid was

placed between the needle and the sample. It was made of stainless steel 304 wires, with the wire diameter of 0.016 inch and the mesh size #20. Polymer film samples, usually 6 inch × 6 inch large, were placed on the grounded electrode, a mirror-polished stainless steel plate. The distance between the needle and the grounded electrode, as well as the spacing between the grid and the grounded electrode can be adjusted separately by adjustable holders. The needle voltage and the grid voltage were controlled by two polarity switchable Glassman Co. Lt., FJ Series 120 Watt regulated high voltage DC power supplies, respectively, with the same polarity. The voltage could be adjusted in the range from 0 to ±40 kV for the needle, and from 0 to ±20 kV for the grid. Charging time was controllable in the range from a fraction of second to many hours; charging temperature could be adjusted by a hot plate underneath the grounded electrode, with less than 5 ℃ temperature gradient in 12-inch range.

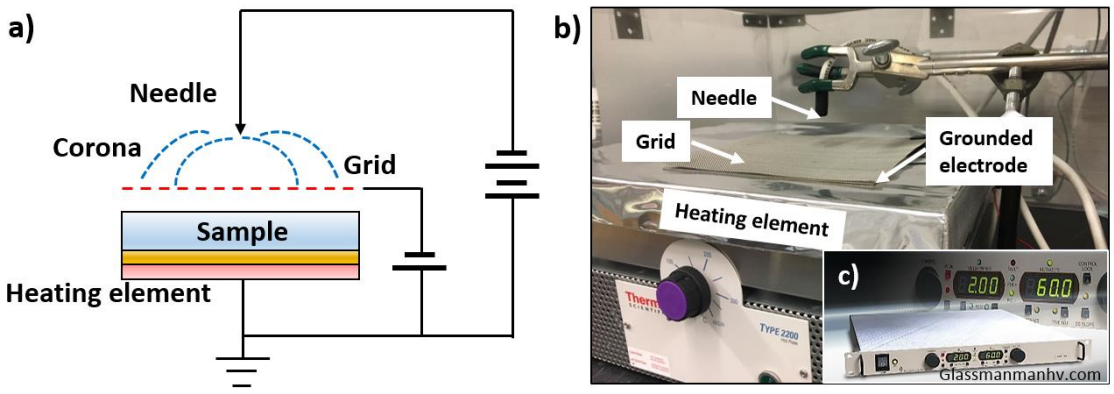

Figure 2.1 The corona charging system: a) schematic and b) the experimental setup, c) high-voltage power supply.

2.2.2 Corona charging process

PET, PC and PFA films with the thickness of 25 μm or 125 μm were cut into 6 inch × 6 inch samples. They were firstly ultrasonically cleaned in isopropyl alcohol (IPA) for 5 min and then in de-ionized (DI) water for another 5 min, followed by drying in a vacuum oven at 70 ºC for 24 hr. The film was first placed onto the grounded electrode. For a needle-plate corona charging setup, the needle was 1 cm, 2 cm, or 4 cm away from the grounded electrode, pointing to the center of the film. The voltage of the needle ranged from 0 to ±12 kV, within the high-accuracy range of the voltmeter.

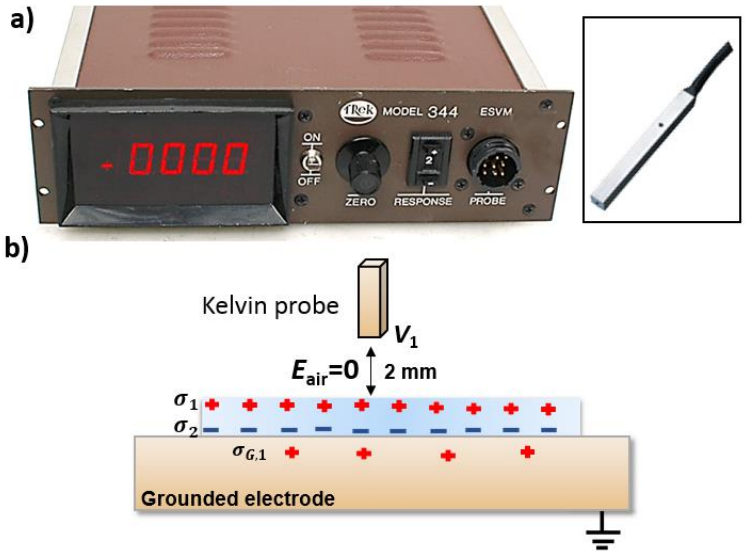

Figure 2.2 Voltmeter for characterization of electrified polymer films: a) Photos of the voltmeter and the Kelvin probe; b) the measurement mechanism.

As shown in Figure 2.1b, the 6 inch × 6 inch steel-wire grid could be inserted in between the grounded electrode and the needle. There was no ohmic contact between the grid and the needle or the sample. The grid voltage was offered by a second high-

voltage power supply. The highest grid voltage used in this experiment was less than ±3 kV. The grid-needle distance was either 4 mm, 12 mm, or 18 mm. The charging time was controlled by a timer, discussed below.

According to our data, positive and negative corona led to similar surface-voltage distributions of electrified polymer films, except for the polarity. In this chapter we report the data of negative corona. For the sake of simplicity, the negative signs of voltages in the following discussion are ignored.

2.2.3 Characterization of electrified polymer films

A Trek Model-344 electrostatic voltmeter (Figure 2.2) was used to measure the voltage distribution on electrified films. The polymer film was placed on the grounded electrode, and a Kelvin vibrating probe was positioned 5 mm above the sample. It can measure the average voltage over a small area less than 10 mm in diameter. Since the film is backed by the grounded electrode, the voltmeter reading reflects the voltage distribution of the side facing the probe. To avoid possible boundary effects, the measurement area was 0.5 inch away from the edges. The measurement spots were 0.5 inch away from each other. For each set of parameter setting, at least three nominally same samples were electrified and characterized. After the electrified side of the film had been scanned by the probe, the sample was turned over and the voltage along its back side was measured, with the electrified side firmly attached to the grounded electrode.

2.3 Results and Discussion

2.3.1 Needle-plate corona charging

Figure 2.3 shows a typical result of the surface voltage of a 125-μm-thick PET film charged at 7.5 kV, in the needle-plate corona charging configuration. It indicates the charge density distribution, fitting well the "bell jar" shape described in literature.[151] The highest voltage in the middle of the film reaches 2816 V; the voltage close to the edge is only 447 V. Clearly, needle-plate corona charged sample does not possess uniform potential distribution, but shows a higher potential in area closer to the needle electrode.

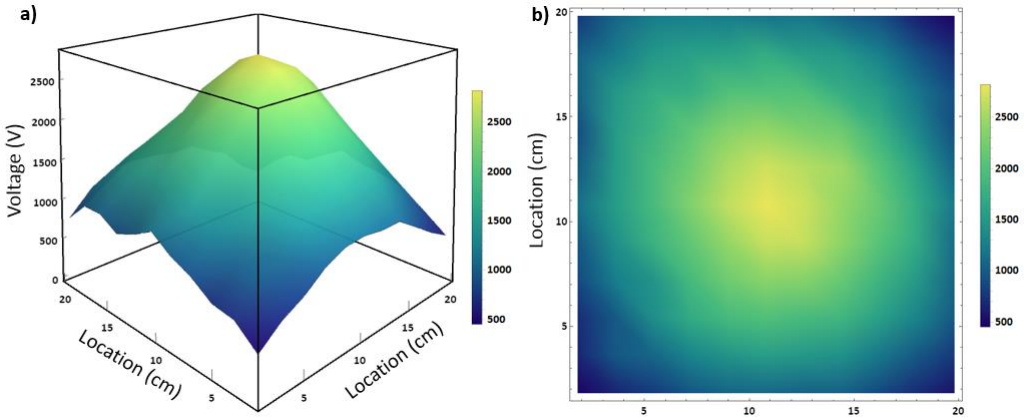

Figure 2.3 Potential distribution of the back side of a needle-plate charged 125-μm-thick PET film. The needle voltage is 7.5 kV; the needle-electrode distance is 4 cm; the charging duration is 60 s.

The needle voltage is varied in a broad range for different samples. As displayed in Figure 2.4a, the voltage distribution of films charged at higher voltages showed larger difference from the center to the edge. For 125-μm-thick PET films, when charged at 8

kV, the highest voltage at the center reaches 3280 V, while the voltage at the corner is only 740 V. For the same PET films charged at 5 kV, the highest point in the center is only 433 V, and the area above 200 V is only ~95 cm^2. Similar patterns were also observed for the positive voltages at the back sides of these samples, as shown in Figure 2.4b; that is, the surface voltage distributions on both sides of the film tend to be symmetric.

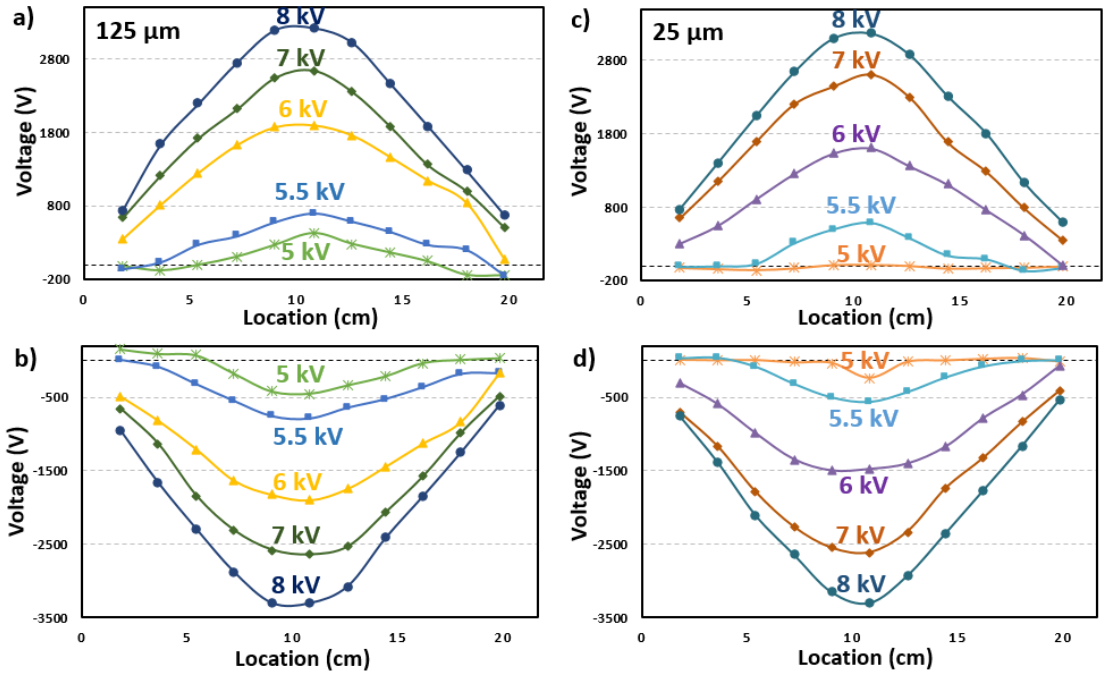

Figure 2.4 Voltage distribution of PET films charged with needle voltage from 5 kV to 8 kV: a) 125 µm thick, top side; b) 125 µm thick, bottom side; c) 25 µm thick, top side; d) 25 µm thick, bottom side. Needle-electrode distance: 4 cm; charging time: 60 s.

For the PET films with thickness of 25 µm and charged at the same parameters (Figure 2.4c), the voltage is slightly lower than that of 125 µm-thick-films and the voltage range from the center to the edges is narrower. Noticeably, at the needle voltage of 5 kV, no surface voltage can be detected on the thinner film. The difference between

the 25-μm-thick and 125-μm-thick films may be attributed to the charge escape as the films are peeled off from the grounded electrode after charging. The thinner films has a less capability of holding charges, as will be discussed in the following chapters.

The above data demonstrate that for a needle distance of 4 cm, the initiating voltage should be in the range of 5 kV to 6 kV, compatible with Peek's law below (Eq. 2.1). It describes the critical electric potential gap for triggering corona discharge between two electrodes:

$$e_v = m_v g_v r \ln(\frac{S}{r}) \qquad \text{(Eq. 2.1)}$$

where e_v is the corona inception voltage, m_v is the irregularity factor (m_v =1 for polished wires), r is the radius of the wires in centimeter, S is the distance between two electrodes, and g_v is the "visual critical" electric field given as:

$$g_v = g_0 \delta (1 + \frac{c}{\sqrt{\rho_0 r}}) \qquad \text{(Eq. 2.2)}$$

$$\delta = \frac{\rho}{\rho_{SATP}} \qquad \text{(Eq. 2.3)}$$

with ρ_0 being the air density with respect to SATP (25 ℃ and 76 cmHg), ~1 in ambient environment; g_0 the disruptive electric field around 30~32 kV/cm; and c the empirical dimensional constant around 0.301 $cm^{½}$. With the needle-electrode distance of 4 cm and needle radius of ~0.1 cm, the corona inception voltage is ~6 kV.

Altering the needle-electrode distance would also considerably affect the potential distribution. Figure 2.5 shows the voltage distribution along the diagonal lines of 25-μm-thick PET films charged at 6 kV. With a needle-electrode distance of only 1 cm, the electrified area is much smaller than that of larger needle-electrode distances,

with only ~40 cm^2 being charged and a sharp bell-like voltage distribution with the maximum value of 2767 V. Here, we set the needle voltage as 6 kV so that, with the small needle-electrode distance, the center voltage in electrified film did not exceed the accurate measurement range of the voltmeter (3300 V). If we move the needle farther form the grounded electrode to 2 cm, the charged area becomes significantly larger; the entire sample is covered by a smooth bell-shaped charge distribution. When the needle height is raised to 4 cm, the voltage in the center area can only reach 1600 V, ~900 V lower than the samples charged with needle height of 2 cm. Therefore, the optimum needle-electrode distance is ~2 cm, which leads to a better corona spreading compared with 1-cm needle height and a more effective corona capture compared with 4-cm needle height.

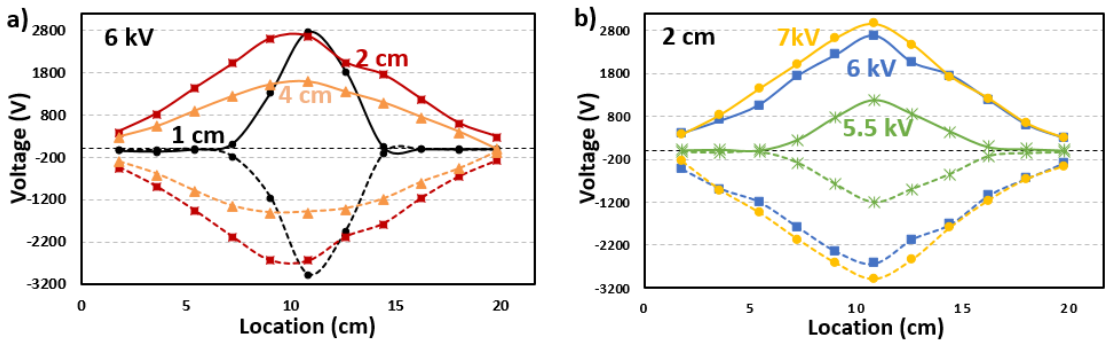

Figure 2.5 a) Influence of the distance between needle electrode and grounded electrode on the surface voltage distribution of electrified films, with the needle voltage of 6 kV. b) Effects of the needle voltage, with the needle-electrode distance of 2 cm. Material: 25-μm-thick PET film; charging time: 60 s.

In Figure 2.5b, samples were charged to various voltages with the needle-electrode distance set as 2 cm. When the needle voltage is 6~7 kV, the surface voltage level of electrified polymer is comparable with that of 8-kV needle voltage when the

needle-electrode distance is 4 cm. With a needle voltage of 5.5 kV, the highest surface voltage is 1175 V. With everything else the same except that the needle-electrode distance is 4 cm, the highest surface voltage is only 580 V; however, the charged area is larger.

2.3.2 Triode corona charging

The data in Section 2.3.1 indicate clearly that the surface voltage distribution of polymer electrified by needle-plate corona system is heterogeneous. Usually, inserting a metallic grid between the needle and the grounded plate electrode would significantly help homogenize the corona field. Such a triode corona system is displayed in Figure 2.1. Figure 2.6 demonstrates the influence of needle-electrode distance, with the grid voltage set as 2 kV. In Figure 2.6a, the needle-electrode distance is only 1 cm, and thus, the needle-grid distance is quite small so that the effective potential at grid is raised it from the set value (2 kV) to 2.5 kV. The uniformity of the surface voltage of electrified samples is poor.

When the needle-electrode distance is increased to 2 cm, the voltage control effect of the grid is much enhanced. Without the grid, the surface voltage of the charged films follows bell-shaped distribution, with the peak voltage around 2950 V; with the grid, the surface voltage in the central 12-cm^2 area is uniformly around 2 kV, the same as the grid voltage. When the needle height reaches 4 cm, the needle voltage can be set to as high as 8 kV without boosting the grid voltage. With the grid, the central 90-cm^2 area in electrified film has uniform 2-kV surface voltage, the same as the grid voltage.

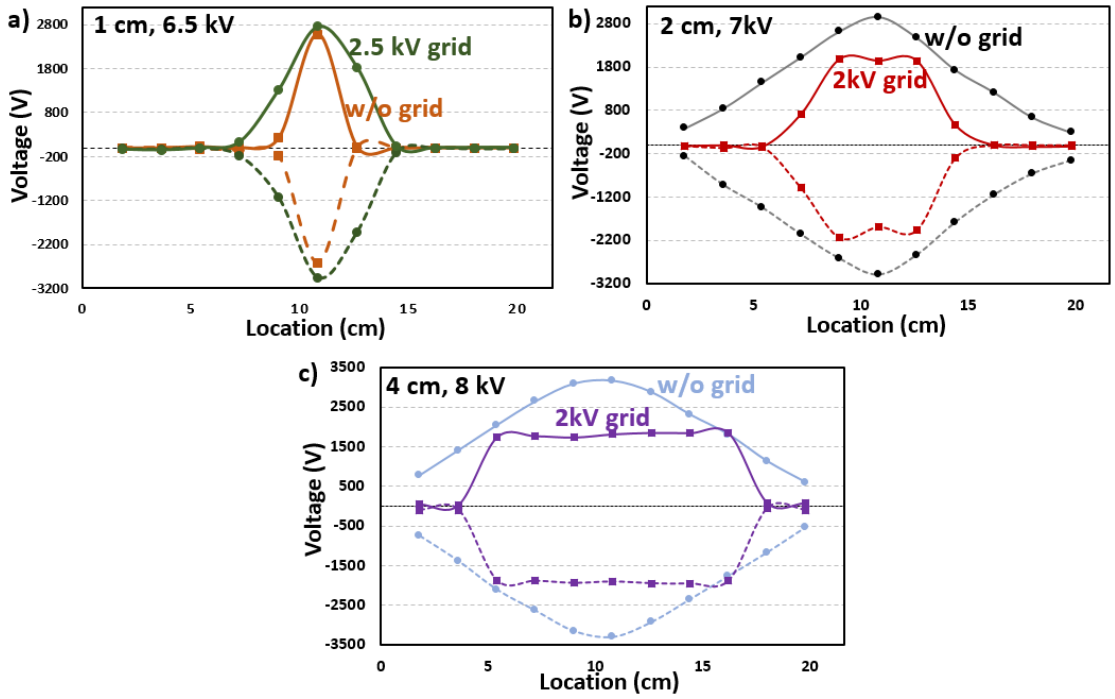

Figure 2.6 Influence of the grid at various needle-electrode distances (d_{ne}) and needle voltages (V_n). a) d_{ne} = 1 cm, V_n = 6.5 kV; b) d_{ne} = 2 cm, V_n = 7 kV; c) d_{ne} = 4 cm, V_n = 8 kV. The sample are 25-μm-thick PET films, charged for 60 s; the grid voltage is 2 kV; the grid-electrode distance is 4 mm.

In comparison, with all the other parameters the same yet without the grid, the surface voltage in the same area can be higher by more than 50% and follows a bell-shaped distribution. It is clear that if the needle-grid distance is too short, the effective grid voltage can be affected and the upper limit of needle voltage must be relatively low. For instance, if the grid voltage is set as 2 kV, when the needle-electrode distance is 2 cm, the highest voltage of the needle can only be 8 kV; otherwise the grid voltage would be raised and somewhat uncontrollable.

As shown in Figure 2.7a, as the needle voltage (V_n) is set to 8 kV, a larger central area of polymer film can be charged uniformly, compared to V_n = 7 kV. When the needle-electrode distance (d_{ne}) is increased to be 4 cm, the grid voltage is independent

of the needle electrode; the needle voltage can be as high as 11.5 kV without boosting the grid voltage (2 kV). Figure 2.7b shows the voltage distribution of samples charged with the same grid voltage (2 kV) and various needle voltages from 8 kV to 11.5 kV. It can be seen that the higher the needle voltage, the larger the central uniform area would be.

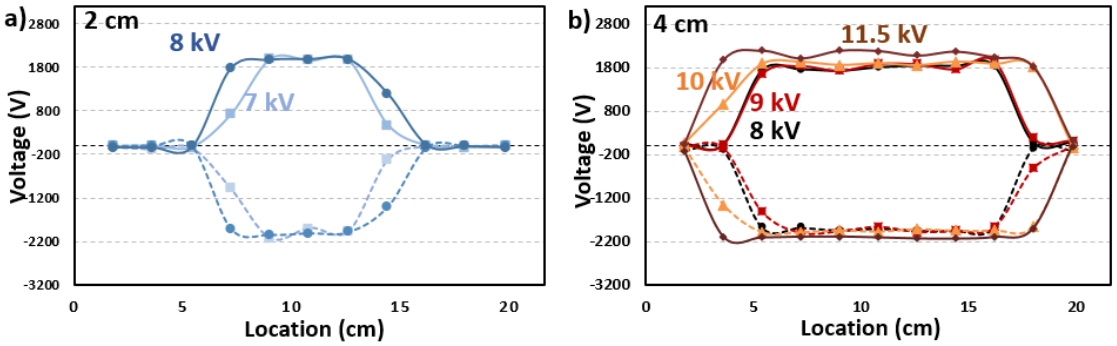

Figure 2.7 Influence of the needle voltage (V_n) and the needle-electrode distance (d_{ne}) on 25-μm-thick PET films charged by the triode system. a) d_{ne} = 2 cm; V_n = 7 kV or 8 kV. b) d_{ne} = 4 cm; V_n = 8 kV, 9 kV, 10 kV, or 11.5 kV. The grid voltage is 2 kV; the grid-electrode distance is 4 mm; the charging time is 60 s.

With all these factors being taken into account, the needle-grid distance should be sufficiently large to avoid unnecessary interaction between the needle and the grid; yet also sufficiently small to avoid high degree of heterogeneity of surface voltage of charged film (Figure 2.5a). The optimum needle-electrode distance is around 4 cm.

2.3.3 Chargeability of polymers

The chargeability of different polymers is tested (Figure 2.8). With the V_n being 8 kV and V_g as 2 kV, the surface voltage distributions of 125-μm-thick PC, PET and

PFA films are quite similar. The surface voltage of PC is slightly higher than that of PFA films; the surface voltage of PET is the lowest. However, if the V_n is increased to be 11.5 kV, the area with surface voltage higher than 1800 V on the PC film is considerably larger than that of PET. That is, PC has a better chargeability than PET.

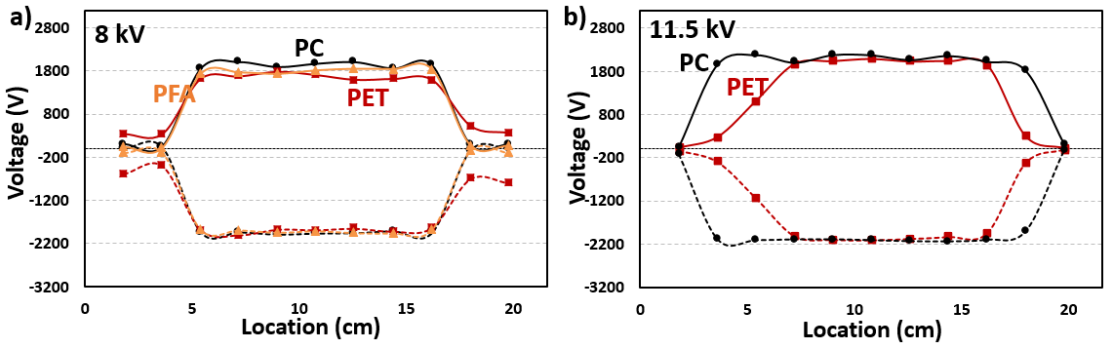

Figure 2.8 Chargeability and charge distribution. a) PC, PET, and PFA films charged at needle voltage of 8 kV, b) PC and PET films charged at needle voltage of 11.5 kV. The film thickness is 125 μm; the grid voltage is 2 kV; he needle-electrode distance is 4 cm; the grid-electrode distance is 4 mm; the charging time is 60 s.

The short-term stability of surface voltage of these polymer films are shown in Figure 2.9. There is almost no change in surface voltage distribution for PET and PC films after 10 min of charging; however, during the same period of time, the surface voltage of PFA film decreases significantly from an average value of -1894 V for the middle 7 measurement points on the front side and 1660 V for the back side to -1313 V and 1193 V, respectively, suggesting that the charge stability on PFA is quite poor.

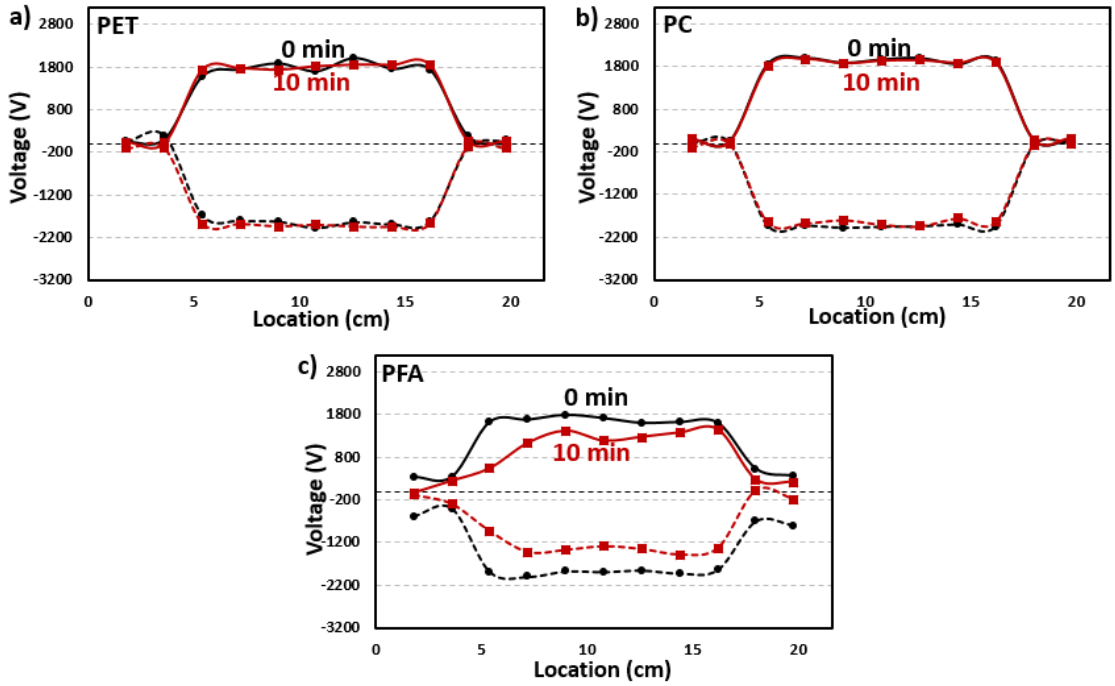

Figure 2.9 Surface voltage distributions immediately (0 min) and 10 min after charging: a) PET, b) PC, and c) PFA. The film thickness is 125 μm; the needle voltage is 8 kV; the grid voltage is 2 kV; the needle-electrode distance is 4 cm; the grid-electrode distance is 4 mm; the charging time is 60 s.

2.3.4 Effects of grid parameters

Among PET, PFA, and PC, PC has the best chargeability and surface voltage stability. To precisely control the electrification process, we tested a few key grid parameters.

The charged areas in electrified films, i.e. the areas where the surface voltages are within 200 V from the grid voltage, are dependent on V_g (Figure 2.10a): ~125 cm^2, ~92 cm^2, and ~64 cm^2 for grid voltage of 1 kV, 2 kV, and 3 kV, respectively. The charged area considerably decreases as V_g rises. In these tests, the needle voltage, V_n, is kept at 8 kV. When the needle voltage is increased to 9 kV, the charged area increases

to ~135 cm^2, ~95 cm^2, and 68 cm^2, respectively, for grid voltage of 1 kV, 2 kV, and 3 kV; that is, the effect of grid voltage is somewhat weaker. The reduction in charged area at higher grid voltage may be attributed to the larger repulsive field between the grid and the needle, which hinders the charge transport in corona.

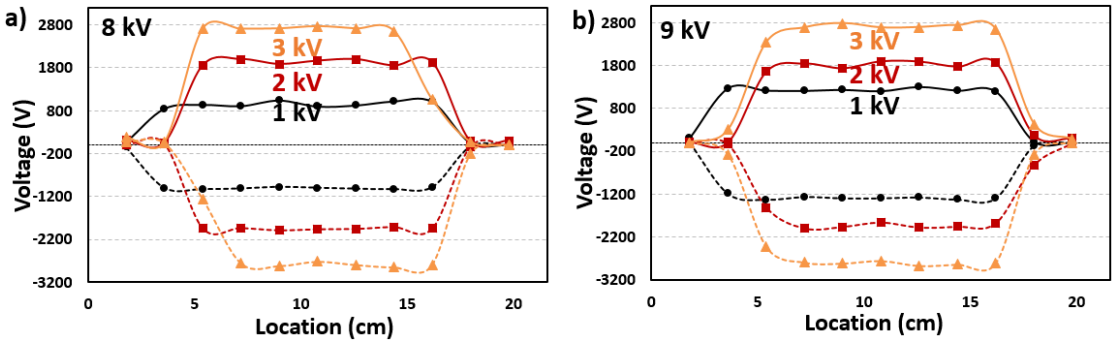

Figure 2.10 Influence of the grid voltage (1 kV, 2 kV, or 3 kV) on the surface voltage distribution of charged films with different needle voltage (V_n). a) V_n = 8 kV, b) V_n = 9 kV. The material is 125-µm-thick PC film; the needle-electrode distance is 4 cm; the grid-electrode distance is 4 mm; the charging time is 60 s.

The grid-electrode distance, d_{ge}, also affects the surface voltage distribution of electrified PC film. As shown in Figure 2.11, with the needle-electrode distance (d_{ne}) of 4 cm, when the d_{ge} is 4 mm, the charged area, i.e. the field where the surface voltage is higher than 1800 V, is ~125 cm^2; when d_{ge} is increased to 12 mm, the charged area decreases to ~90 cm^2; when d_{ge} further rises to 12 mm, the charged area is only ~35 cm^2 and the surface voltage tends to be much less uniform. Clearly, reducing when d_{ge} is beneficial to generate larger charged area with homogeneous surface charge distribution. Moreover, with a given needle-electrode distance, a smaller grid-electrode distance leads to a larger grid-needle spacing, so that the effective grid voltage is not influenced by the needle voltage.

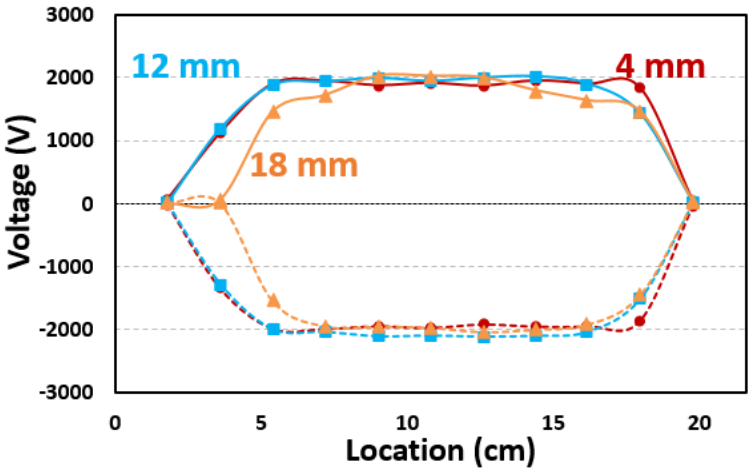

Figure 2.11 Influence of the grid-electrode distance (4 mm, 8 mm, or 12 mm) on the surface voltage distribution of electrified 125-μm-thick PC films. The needle voltage is 10 kV; the grid voltage is 2 kV; the needle-electrode distance is 4 cm; the charging time is 60 s.

2.3.5 Effects of charging time

Charging time, t_c, is another important parameter. In our experiment, PC films with the thickness of 125 μm were corona treated for different durations, ranging from 10 s to 180 s. As shown in Figure 2.12a, the charged area increases with the charging time.

Figure 2.12b, for instance, shows the surface voltage at the point 3.6 cm from both edges of electrified film. The surface voltage distribution also becomes more uniform as t_c is longer. There exists a critical t_c, around 10-20 s, below which the charged area rises rapidly with the charging time and above which the effect of t_c saturates. With the uniformity of surface voltage, charged area, energy consumption, and processing time being taken into consideration, the optimum charging time is 20 s to 60 s.

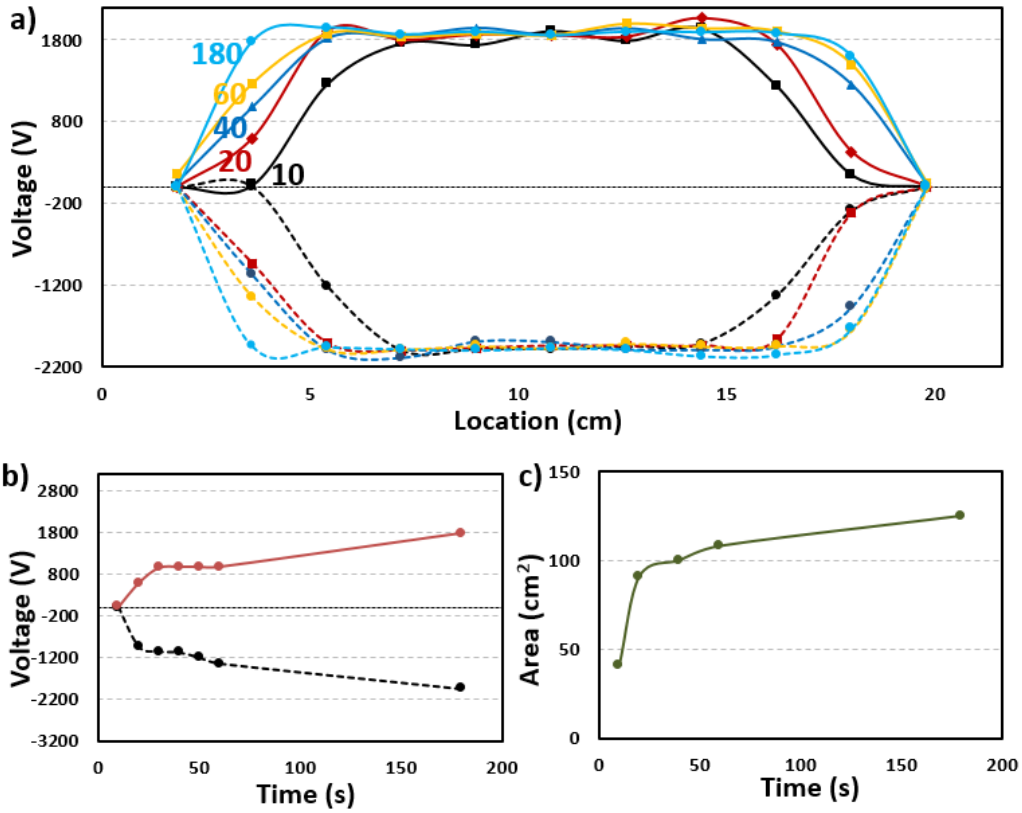

Figure 2.12 Effects of charging time. a) Surface voltage distribution of samples charged for 10 s, 20 s, 40 s, 60 s, and 180 s. b) Surface voltage at (3.6 cm, 3.6 cm) on the film. c) Charged area, i.e. the field where surface voltage is above 1600 V, as a function of the charging time. The material is 125-μm-thick PC film; the needle voltage is 10 kV; the grid voltage is 2 kV; the needle-electrode distance is 4 cm; the grid-electrode distance is 4 mm.

2.4 Concluding Remarks

A triode corona charging system was built up with controllable charging parameters: needle polarity and voltage, grid polarity and voltage, needle-electrode and grid-electrode distances, charging time, and temperature. On the front and back sides of electrified PC, PET, and PFA films, the polarity was opposite while the magnitude of

surface potential was similar. The initiate voltage of corona was around 5 kV to 5.5 kV for the 0.1-cm-radius needle electrode when the needle-electrode was 4 cm. The initiate voltage increased with the needle-electrode distance and the radius of curvature of the needle tip. With the same corona system setting, thicker PET films had higher surface potential than thinner ones. Decreasing needle-electrode distance led to a higher surface potential of electrified film, yet the charged area was reduced. Higher needle voltage led to a larger charged area, yet this effect saturated when the needle voltage exceeded a certain value.

Inserting a metallic grid between the needle electrode and the grounded plate electrode could significantly enhance the homogeneity of surface voltage of charged polymer films. The surface voltage of electrified film was typically close to, but slightly lower than the grid voltage. Increasing the needle voltage was beneficial to increasing charged area; however, when the needle-grid distance was small or the needle voltage was high, the grid voltage might be unstable or non-uniform. To achieve a large uniformly charged polymer surface, relatively large needle-electrode distance, small grid-electrode distance, large needle-grid distance, relatively high needle voltage are desirable. Increasing charging time could increase the charged area, but this effect saturated when the charging time was longer than 20 s. The optimum charging time is likely in the range from 20 s to 60 s. Among the investigated polymer materials, PC films had the highest chargeability and the most stable surface voltage. PFA films could hold the charges stably.

2.5 Acknowledgment

This chapter, in part, is a reprint of the material prepared to be submitted for publication, Corona charging: system and key parameters, authored by Ying Zhong, Rui Kou, Lewis Fowlergerace, Meng Wang, and Yu Qiao. The dissertation author was the primary investigator and first author of the paper.

Chapter 3 Corona charging: Dipolar charge distribution

3.1 Introduction

For corona charged polymer electrets, their long term stability,[152, 153] charging mechanisms and processes, charge distribution,[91, 146, 154] as well as electrical potential distribution [62, 155] have been extensively investigated. The study in this field provided important information of the interaction among charges and dielectric materials.

The surface-voltage decay of corona charged polymeric films has been commonly noticed.[106, 150, 156] A classic "cross-over" phenomenon was first reported by Ieda et al. in 1967, indicating that the surface voltage of polyethylene (PE) films charged with higher initial potential (V_i) decayed faster than that of lower V_i; eventually, PE films with lower V_i would have higher long-term surface voltage than higher V_i.[150] However, other dielectric materials may demonstrate different characteristics.[90] The surface-voltage decay time constant varies from minutes to years, depending on the material properties and the charging parameters.[87, 150] In general, the decay of surface voltage is a complex procedure that may involve surface conduction,[91] volume conduction,[93] atmospheric neutralization,[94, 95] external charge injection,[96] electric field polarization,[97] humidity and contamination attraction,[98] among others. To manufacture polymer electrets with stable surface voltages, it is imperative to systematically examine the effects of key parameters on the decay rate. Such parameters include polymer species,[99, 100] film thickness,[101] charging voltage and temperature,[102,

[103] working environment,[98] etc. Most of them come in by affecting the charge distribution and charging mechanism. In addition to directly monitoring the surface potential of the charged films with voltmeter,[95] other experimental approaches such as thermal stimulated discharge (TSD),[104, 105] pulse electro acoustic (PEA),[106] and laser induced modulation (LIMM) [107] have been developed to precisely measure the charge amount and distribution. However, those technologies often have tight requirements on materials properties and charging/discharging conditions.[85]

Currently, there are a few of charging models of electret formation, each capturing a subset of the observed phenomena: 1) Dipole alignment/polarization in polar polymers and polarizing electric field can be offered by the corona and/or the accumulated surface charges;[88, 89] 2) injection of charges from the surface into the bulk by the corona electric field and/or by the accumulated surface charges (the injection may happen at only one side or on both sides of the film);[90] 3) combination of polarization and charge injection.[86] These models shed much light on the nature of charging and discharging of polymer surfaces, having important relevance to the application of electrets in transducers,[68] electrophotography,[69] recording,[70] advanced filtration;[71] motors and generators;[72] dosimeters;[73] piezoelectric devices,[74] microphones,[64] energy harvesting systems,[54] etc.

In this Chapter, we investigate a few key processing parameters that govern the voltage stability of electrified polymer surfaces, e.g. the material, the film thickness, and the charging temperature. The charge distribution and its influence on electric potential distribution are analyzed in detail. Dipolar charge distribution caused by simultaneous

charge injection from both sides of polymer film is identified as the dominant charging mechanism for the parameter settings under investigation.

3.2 Experimental

3.2.1 Triode corona charging

A corona charging system (Figure 2.1) was built up to electrify selected polymer films. The setup consisted of a needle electrode, an optional metal-wire grid, a grounded plate electrode, heating elements, and two high-voltage power supplies. A 0.75-inch-long 0.059-inch-diameter tungsten needle was employed as the needle electrode. The curvature of the needle tip was ~0.1 mm. A grid was placed between the needle and the sample. It was made of stainless steel 304 wires, with the wire diameter of 0.016 inch and the mesh size of #20. The distance between the needle and the grounded plate electrode (d_{ne}) was set as 4 cm, and the spacing between the grid and the electrode (d_{ge}) was 4 mm. The needle voltage and the grid voltage were controlled by two polarity switchable Glassman Co. Lt., FJ Series 120 Watt regulated high-voltage DC power supplies, respectively, with the same polarity. The voltage could be adjusted in the range from 0 to ±40 kV for the needle, and from 0 to ±20 kV for the grid. Charging time was controllable in the range from a fraction of second to a few hours; charging temperature could be adjusted by a hot plate underneath the grounded electrode, with less than 5 ℃ temperature variation in the 12-inch range.

We investigated a few transparent polymer films commonly used in industry: PP, PET, PMMA, PC and FEP. The film thickness was 25 μm, 50 μm, or 125 μm. All the films were 3 inch × 3 inch large. They were ultrasonically cleaned first in isopropyl alcohol (IPA) for 5 min and then in de-ionized (DI) water for another 5 min, followed by drying in a vacuum oven at 70 ºC for 24 hr. During charging, a polymer film sample was placed onto the grounded electrode, with the grid 4 mm above and the needle pointing to the center of the film. According to the parameterized study in Chapter 2, the needle voltage, V_n, was set to 12 kV. The corona polarity was set as positive and the grid voltage, V_g, was set to 2 kV, except where specifically noted. After corona charging, the polymer films were at rest in a sealed dry keeper (H121227 Sanplatec Corp. Sanpla) at ambient temperature with the relative humidity (RH) around 40 %.

3.2.2 Potential measurement

After corona charging, the charged sample was characterized with voltmeter (Trek, Model 344 electrostatic voltmeter) and fieldmeter (Simco, FMX-004 electrostatic fieldmeter). For the voltmeter measurement (Figure 3.1a), the polymer film was placed on a grounded electrode, and a Kelvin vibrating probe was positioned 5 mm above the sample. It could measure the average surface voltage over a small surface area less than 10 mm in diameter. Since the film was backed by the grounded electrode, the voltmeter reading reflected the voltage distribution of the side facing the probe. With V_n= 12 kV, d_{ne}=4 cm, d_{ge}=4 mm, charging time t_c =60 s, and charging temperature T=65 ºC, we could charge the films uniformly with the voltage variation less than 50 V along the film

surfaces. Typically, for a charged sample we measured the surface voltage values at 5 points across the film, and calculated the average value. After the top side of the film (the side facing the needle and grid during charging) was measured, the sample was turned over and the voltage along its bottom side was measured, with the top side firmly attached to the grounded electrode.

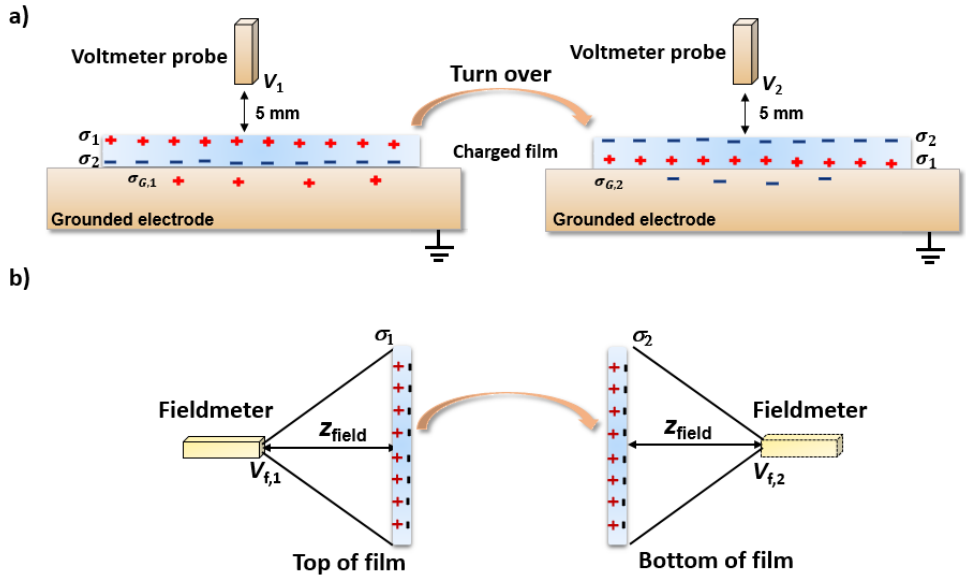

Figure 3.1 Measurement methods of surface voltage: a) Voltmeter and b) Fieldmeter.

In fieldmeter measurement (Figure 3.1b), the probe was placed 25 mm away from the polymer film, as the film was free-standing in air. The fieldmeter reading reflected the contributions from both sides of the film. Any contact between other objects with the charged surfaces was carefully avoided. For each parameter setting, at least 5 samples were charged and measured. Surface-voltage stability tests were carried out for 7 days, with the surface voltages being monitored once every 24 h.

3.2.3 Short-circuit discharge

To understand the charge distribution and charging mechanism of the electrified polymer films, we carried out short-circuit discharge experiments. A charged polymer electret film was firmly placed on a grounded plate electrode, which was connected to the negative end of a Keithley-2420 sourcemeter for current measurement. The positive end of the sourcemeter was connected to a 1.5 inch × 2 inch large 20-μm-thick aluminum (Al) foil. The Al foil was placed adjacent to the top side of the charged polymer film. Through induction, the charged polymer film attracted the flexible Al foil along the entire surface, forming a short circuit. Thus, discharge occurred, typically in less than 0.2 s. The short-circuit discharge current-time profile was recorded.

To test the discharge current direction and to understand the charge polarity distribution, one group of positively corona charged polymer film samples were measured with their top sides connected to the positive end of the sourcemeter; another group of samples were measured with their bottom sides connected to the positive end of the sourcemeter. Two other groups of samples charged with negative corona were also measured, along both directions. The total discharged charge amount was calculated by integrate the current-time curve. At least 5 samples were measured for each parameter setting.

3.3 Results and Discussion

3.3.1 Parameters affecting the charge stability

3.3.1.1. Effects of polymer material

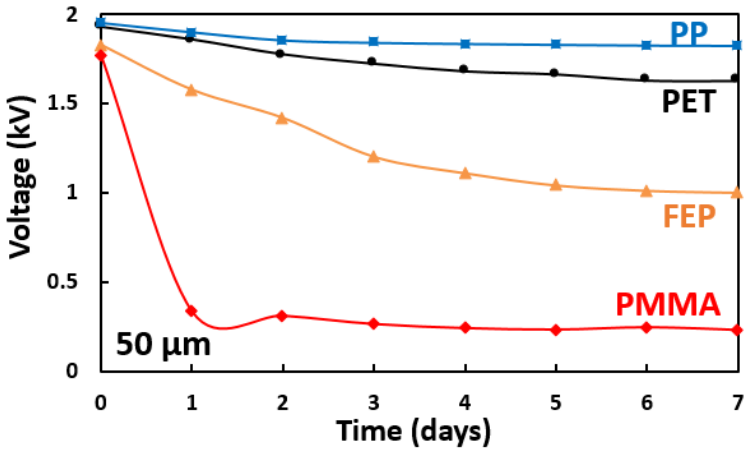

Figure 3.2 Comparison of surface-voltage stability of 50-µm-thick corona charged PP, PET, FEP and PMMA films. The needle voltage V_n = 12 kV; the grid voltage V_g = 2 kV; d_{ne} = 4 cm; d_{ge} = 4 mm; the sample size is 3 inch × 3 inch; the charging temperature T = 20 ℃; the charging time is 60 s.

The stability of surface voltages of corona charged films of various polymers is evaluated. Figure 3.2 compares the stability of surface voltages of 50-µm-thick PP, PET, FEP, and PMMA films charged with V_g = 2 kV for 60 s at 65 ºC. For PMMA and FEP, the surface voltage reduction are more than 80% and 12% after the first 24 h, respectively. PP and PET films can maintain more than 95% and 85% of their surface voltages after 7 days, respectively. The surface-voltage decay (ΔV_s) slowed down after the 4th day; from the 4th to the 7th day, ΔV_s is around 1%, 5%, 17% and 13% of the initial

value for PP, PET, FEP, and PMMA films, respectively. Clearly, in terms of voltage stability, PP is better than the rest three materials under investigation; PET is the second best; PMMA has the lowest performance. The top and the bottom sides of charged film have nearly the same amplitudes of surface voltage (V_v) over time, measured by the voltmeter.

3.3.1.2. Film thickness effects

Figure 3.3a shows the voltage stability of PET films with various thicknesses from 25 μm to 125 μm; all the other charging parameters are the same. It can be seen that the decay of surface voltage of 25-μm-thick PET films is quite fast, with only ~60% voltage left after 3 days. For films with thicknesses of 50 μm and 125 μm, the voltage reduction over the same period of time are only ~10% and ~6%, respectively. Especially, from day 3 to day 7, the surface voltage of 125-μm-thick film enters a steady-state, with the voltage reduction less than 20 V.

Surface voltage of FEP film is generally less stable that of PET film. As shown in Figure 3.3b, the voltage of 25-μm-thick FEP film is only ~45% of V_i after 7 days; the decay of voltage of thicker FEP films is much slower. The decay rates of 50-μm-thick and 125-μm-thick films are nearly identical, suggesting that the film thickness effect has saturated; for both thicker films, ~60% of V_i is kept to the end of the 7^{th} day.

It is clear that thicker polymer film tends to have a better surface-voltage stability in the ranges of parameters in the current study. The beneficial thickness effect saturates as the film thickness exceeds a certain critical value.

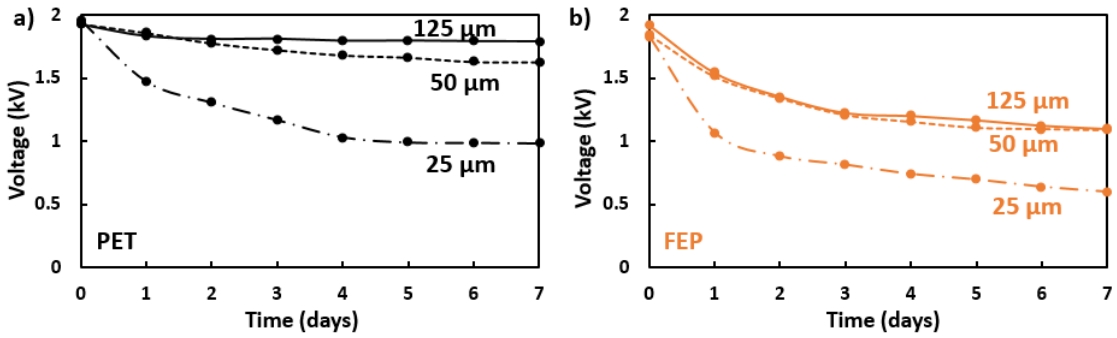

Figure 3.3 Influence of film thickness on voltage stability: a) PET films and b) FEP films. The film thickness is either 25 µm, 50 µm, or 125 µm. The needle voltage V_n = 12 kV; the grid voltage V_g = 2 kV; d_{ne} = 4 cm; d_{ge} = 4 mm; the sample size is 3 inch × 3 inch; the charging temperature T = 20 ℃; the charging time is 60 s.

3.3.1.3. Effects of initial surface voltage

PET films of various thicknesses are charged with different grid voltages (V_g), so that their initial surface voltages (V_i) distribute in a broad range, as shown in Figure3.4. Figure 3.4a indicates that the voltage stability of 25-µm-thick PET film charged with V_g = 3 kV is quite poor, compared to V_g = 2 kV and 1 kV. After 5 days, the voltages of the films with V_g = 3 kV and V_g = 2 kV both converge to ~1 kV, although the former has a much higher V_i. The films with V_g = 1 kV demonstrates the slowest voltage decay rate. For PET films with the thickness of 50 µm (Figure 3.4b) and 125 µm (Figure 3.4c), the voltage decay rates decrease as the thickness rises. After 7 days, more than 90%, 93% and 94% of V_i is maintained by 125-µm-thick films charged at V_g = 3 kV, 2 kV and 1 kV, respectively. Since the voltage decay rate of films with high V_i tends to be faster, the "cross-over" phenomenon is likely dominant when the film thickness (δ) is less than 50 µm.[150] For the thicker films (e.g. 125-µm-thick films) or

films having inherently high voltage stability (e.g. PP films), it may take a relatively long time for the "cross-over" phenomenon to occur.

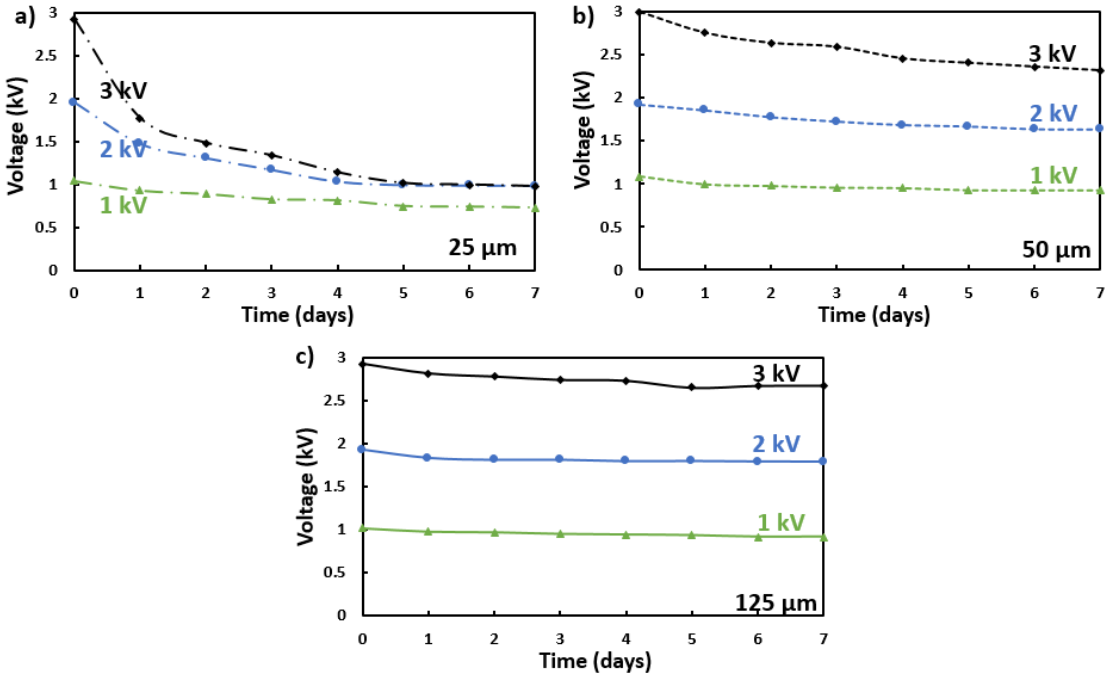

Figure 3.4 Influence of the initial voltage on the voltage stability of PET films with different film thicknesses: a) δ=25 µm, b) δ=50 µm, c) δ=125 µm. For samples charged with V_v =1 kV, the needle voltage V_n = 8 kV and the grid voltage V_g = 1 kV; for samples with V_v =2 kV, V_n = 12 kV and V_g = 2 kV; for samples with V_v =3 kV, V_n = 13 kV and the grid voltage V_g = 3 kV. For all the samples, d_{ne} = 4 cm; d_{ge} = 4 mm; the sample size is 3 inch × 3 inch; the charging temperature T = 20 ℃; the charging time is 60 s.

3.3.1.4. Effects of charging temperature

Charging temperature, T, is another important factor affecting the stability of surface voltage (Figure 3.5). For PET films with the thickness of 50 µm, if T = 100 °C is much higher than the glass transition temperature (T_g ~ 80 °C), the initial voltage after charging (V_i) is around 1.4 kV, much lower than the grid voltage V_g = 2 kV. When T is

lower than T_g, (e.g. T = 20 ℃ or 65 ℃), V_i is around 1.9 kV, close to the grid voltage. The low V_i at $T > T_g$ may be attributed to the high-temperature discharge that occurs when the film sample is dismounted from the grounded plate electrode. It is also noticed that for all the tested samples, the measured potential is always at least ~100 V lower than the grid voltage, which, again, should be related to the surface discharge during dismounting process after the charging has been completed. It may also be associated with the imperfection at the sample-electrode interface, during the voltmeter measurement.

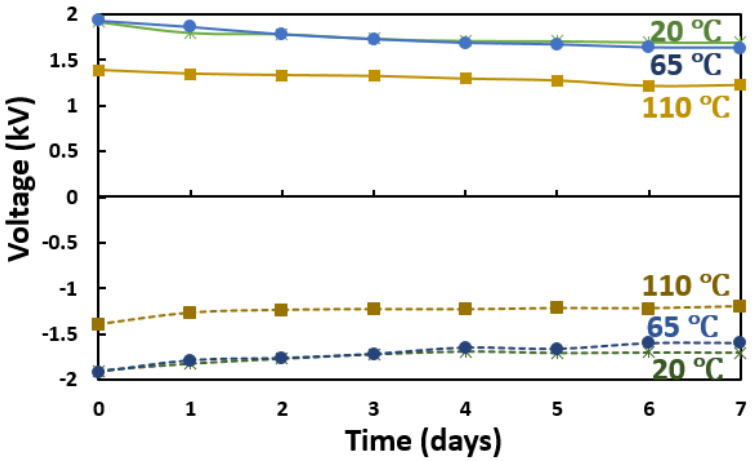

Figure 3.5 Influence of the charging temperature on the voltage stability of 50-μm-thick PET films charge with the grid voltage of 2 kV: the top side (up) and the bottom side (bottom). The needle voltage V_n = 12 kV; the grid voltage V_g = 2 kV; d_{ne} = 4 cm; d_{ge} = 4 mm; the sample size is 3 inch × 3 inch; the charging temperature is 20 ℃, 65 ℃, and 100 ℃ respectively; the charging time is 60 s.

The influence of the charging temperature on the voltage decay rate of charged films is secondary, regardless of the variation in V_i. This phenomenon is different from the V_i effect discussed in Section 3.3.1.3, where a higher V_i caused higher V_g would speed up the reduction in surface voltage, suggesting that the voltage stability depends

on not only the initial voltage, but also the history of charging, i.e. how the initial voltage is reached. In general, compared with $T > T_g$, when $T < T_g$ a higher V_i can be achieved with a relatively high voltage stability.

3.3.2 Dipolar component of surface charges

Many previous studies on electrets were based on voltmeter measurement of voltages of electrified films on grounded electrodes. In our tests, we also analyzed surface voltages of free-standing electret films from both sides by using fieldmeter, with the probe 25 mm away from the film surface.

As extensively discussed in literature,[83, 98, 143] the surface voltages of electrets processed under nominally same conditions varied in broad ranges; in some cases even the polarity could be different. For instance, in Figure 3.6a, immediately after charging with the same parameter setting, one PP film had the surface voltage (measured by the fieldmeter), V_{ft}, of 10.2 kV on the top side and V_{fb} 8.9 kV on the bottom side; the V_f values of another PP film were 8.4 kV and 7.1 kV, respectively. All the ten charged samples demonstrated different surface voltages.

Figure 3.6 shows the decay profiles of surface voltages. The insets in Figure3.6a and Figure3.6b demonstrate magnified views. It is remarkable that, while the absolute values of surface voltage of films charged under the same condition can be vastly distinct, the voltage different between the front and the bottom sides, ΔV_f, are nearly identical; over time, it rapidly converges to a steady-state after the first 24 h. The ratio between ΔV_f and the voltmeter measurement result, V_v, is shown in Figure 3.6c, d. For

instance, for the two PP films shown in Figure 3.6a,c, ΔV_f immediately after charging are both 1.3 kV, and V_v on the top and the bottom sides are 1.91 kV and -1.86 kV, respectively; after 7 days, ΔV_f becomes 1.15 kV and V_v decrease to 1.80 kV and -1.79 kV, respectively. The ratio between ΔV_f and V_v is around 1.5~1.6 during the entire process. For the two PMMA films shown in Figure 3.5b, d, ΔV_f reduces from 1.2 kV to 0.17 kV after 7 days; V_{vt} reduces from 1.709 kV to 0.268 kV, and V_{vb} decreases from -1.658 kV to -0.214 kV. Note that the decay rates of ΔV_f and V_v remain similar from day 1 to day 7, and the ratio between them, $R = V_v/\Delta V_f$, is approximately a constant.

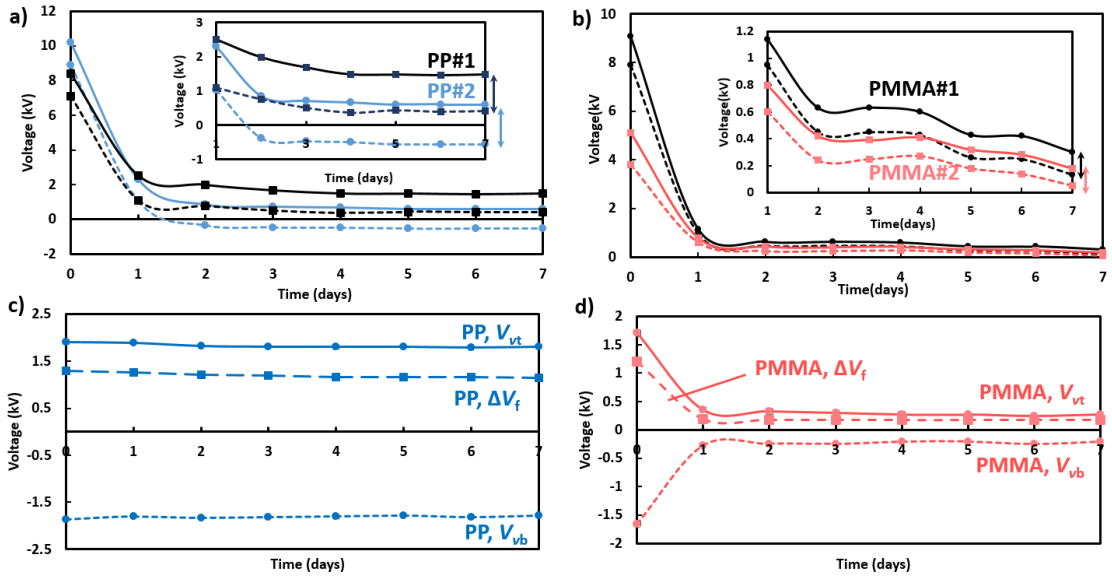

Figure 3.6 Comparison between voltmeter and fieldmeter measurement data. a) Fieldmeter measured top-side voltage, V_{ft}, and the back-side voltage, V_{fb}, of two 50-μm-thick PP films charged with the same parameters. b) V_{ft} and V_{fb} of two 50-μm-thick PMMA films charged with the same parameters. Comparison of voltmeter measured results of top side (V_{vt}) and bottom side (V_{vb}) of c) PP films and d) PMMA films. The needle voltage V_n = 12 kV; the grid voltage V_g = 2 kV; d_{ne} = 4 cm; d_{ge} = 4 mm; the sample size is 3 inch × 3 inch; the charging temperature T = 20 ℃; the charging time is 60 s.

Figure 3.7 shows the decay profiles of ΔV_f for PP, PET, FEP and PMMA films. The decay trend is compatible with Figure 3.2, with R being ~1.5 over the period of measurement for all the films. That is, the R ratio is a system constant, quite independent of the material properties and the surface voltage decay. It reflects the dipolar charge distribution in the films, detected by the voltmeter and the fieldmeter through different mechanisms, discussed in Section 3.3.4 below. The variations of the R values of PMMA and FEP films are mostly related to the uneven decay rates along film surfaces.

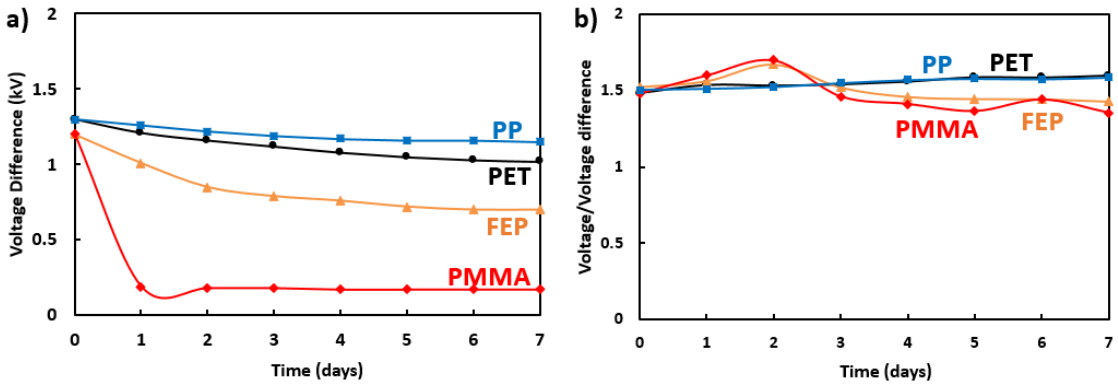

Figure 3.7 a) Voltage decay profile of ΔV_f of 50-μm-thick PP, PET, FEP and PMMA films. b) The change in ratio $R = V_v/\Delta V_f$. The needle voltage V_n = 12 kV; the grid voltage V_g = 2 kV; d_{ne} = 4 cm; d_{ge} = 4 mm; the sample size is 3 inch × 3 inch; the charging temperature T = 20 ℃; the charging time is 60 s.

3.3.3 Short-circuit discharge on PC films

Based on the aforementioned testing results, we hypothesize that the charges on the top and the bottom sides of a film are mainly injected from the corona and the compensating grounded electrode, respectively. The majority of the charges accumulate

in the surface zones, with the rest small portion of charges entering into the interior. Even if polarization could happen, its effect is secondary.

To validate this hypothesis, short-circuit discharge experiment was conducted, as shown in Figure 3.8. For PC film charged with positive corona, when the negative (bottom) side of film is connected to the positive end of the ammeter, electrons escape from the negative side to the positive side of film through ammeter. If connections of positive and negative ends of ammeter are shifted, the discharge current direction would be reversed. That is, the positive charges on the top side of the film are from the positive corona, and the negative charges on the bottom side are from the compensating grounded electrode, rather than the polarization in the interior. Similar results are obtained on films charged with negative corona.

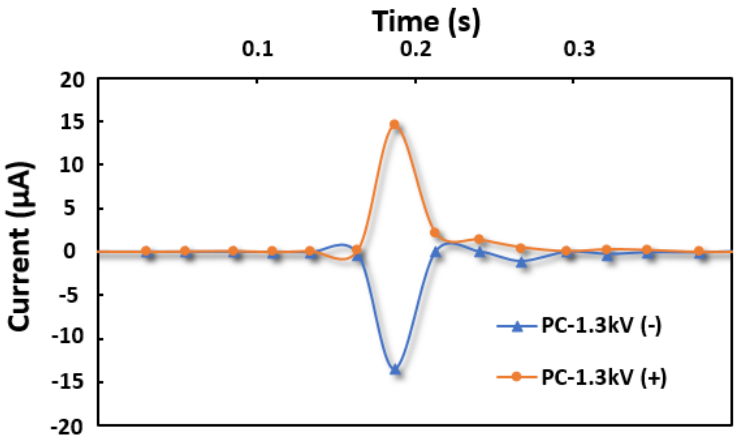

Figure 3.8 Discharge profiles of two 125-μm-thick PC films charged with positive corona, and top side or bottom connect to positive side of the ammeter, respectively. The initial surface voltages of both films are 1.3 kV.

The short-circuit discharge profiles of films of various V_i are shown in Figure 3.9. The discharge happens instantaneously after the formation of short circuit, within

0.1 s. By integrating the discharge current over time, it can be seen that the discharged charge amount increases with V_i. Moreover, after the discharge current vanishes, a relatively low residual potential (~200 V) remains on the surfaces of all the tested samples, which should be attributed to the charges in the interior.[107]

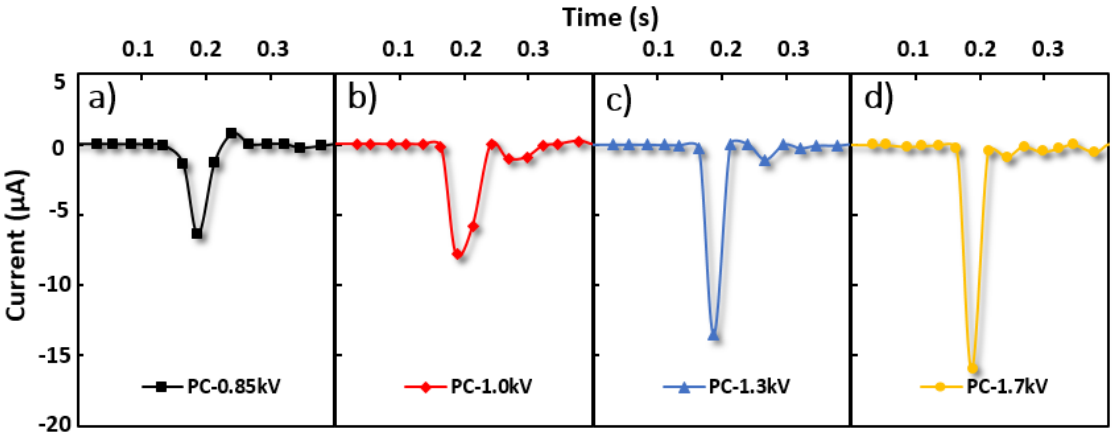

Figure 3.9 Discharge profiles of 125-μm-thick PC films charged with negative corona with different initial surface voltages: a) 0.85 kV, b) 1.0 kV, c) 1.3 kV, and d) 1.7 kV.

3.3.4 Model of dipolar charge distribution

3.3.4.1. Charge density and voltmeter measurement result

The fact that the R ratio is nearly constant regardless of the large variation in V_i and the voltage decay may be explained by the model of dipolar charge injection: Consider a polymer film charged with positive corona; the top side is positively charged with the surface charge density of σ_1, and the bottom side is negatively charged with the charge density of σ_2, as shown in Figure 3.1. The magnitudes of σ_1 and σ_2 should be similar. The sample is firmly placed on a grounded electrode for voltmeter

measurement. The density of the induced charges in the electrode is $\sigma_{G,1}$ when the positively charged top side faces upwards, and $\sigma_{G,2}$ when the bottom side faces upwards. The voltmeter readings are denoted as V_1 and V_2 for the two cases, respectively.

Assume that the surface charge distribution is continuous. The overall surface voltage can be calculated as the summation of the contributions from all the charges, dq, with the potential at infinity set to zero. The electrical potential caused by dq at a location r away from the charge is

$$V = \frac{1}{4\pi\varepsilon_0}\frac{\mathrm{d}q}{r} \qquad \text{(Eq. 3.1)}$$

where ε_0 is the permittivity.

The sample is square-shaped, with the size of L. A representative small area carries dq=σdxdy, with σ being the average charge density and dx and dy the length and the width, respectively. If the film is at (x, y, 0) and the probe, M, is located at (0, 0, z), the voltage offered by a single charged surface is

$$V(\sigma, z) = \int_{-L/2}^{L/2}\int_{-L/2}^{L/2}\frac{\sigma}{4\pi\varepsilon_0\sqrt{x^2+y^2+z^2}}\,\mathrm{d}x\,\mathrm{d}y \qquad \text{(Eq. 3.2)}$$

Integration of Eq. 3.2 gives

$$V(\sigma,z) = -\frac{\sigma}{2\pi\varepsilon_0}\left(2z\bullet\mathrm{ArcTan}\left[\frac{L^2}{4z\sqrt{\frac{L^2}{2}+z^2}}\right] + L\left(\ln\left[-\frac{L}{2}+\sqrt{\frac{L^2}{2}+z^2}\right] - \ln\left[\frac{L}{2}+\sqrt{\frac{L^2}{2}+z^2}\right]\right)\right) \qquad \text{(Eq. 3.3)}$$

Denote the film thickness as t and the height of voltmeter probe as z_{volt}. As shown in Figure 3.1b, the potential measured by the voltmeter is the summation of the potential offered by the top side of charged film $V(\sigma_1, z_{volt})$, the potential offered by the bottom

side $V(\sigma_2,(z_{volt}+t))$, and the inducted potential on the grounded electrode $V\left(\sigma_{G,1},(z_{volt}+t)\right)$. Thus, Eq. 3.4 gives the electric potential V_1 measured by the voltmeter for the top side, and Eq. 3.5 gives V_2 measured by the voltmeter from the other side:

$$V_1 = V(\sigma_1, z_{volt}) + V(\sigma_2,(z_{volt}+t)) + V\left(\sigma_{G,1},(z_{volt}+t)\right) \quad \text{(Eq. 3.4)}$$

$$V_2 = V(\sigma_2, z_{volt}) + V(\sigma_1,(z_{volt}+t)) + V\left(\sigma_{G,2},(z_{volt}+t)\right) \quad \text{(Eq. 3.5)}$$

As the bottom side of the film is in contact with the grounded electrode,

$$0 = V(\sigma_1,-t) + V(\sigma_2,0) + V\left(\sigma_{G,1},0\right) \quad \text{(Eq. 3.6)}$$

$$0 = V(\sigma_2,-t) + V(\sigma_1,0) + V\left(\sigma_{G,1},0\right) \quad \text{(Eq. 3.7)}$$

The parameters involved in Eq. 3.1 to Eq. 3.7 are given in Table 3.1, based on the experimental measurement. It can be shown that the surface charge density, σ and the electric potential measured by voltmeter, V_v, are linear to each other (Figure 3.10a). In Figure 3.10b, the parameters of an electrification test of PP film are used: the needle voltage is 12 kV; the grid voltage is -2 kV; the charging temperature is 60 ℃; the charging time is 60 sec; the sample size is 3 inch; the sample thickness is 125 μm; the surface voltages measured by voltmeter form the top and the back sides are ~2 kV and -2 kV, respectively.

Table 3.1 Parameters used in Eq. 3.1 to Eq. 3.7

Parameter (unit)	Values
ε_0 (F/m)	8.85×10^{-12}
t (m)	50×10^{-6}
z_{volt} (m)	5×10^{-3}
z_{field} (m)	25×10^{-3}
L (m)	0.076

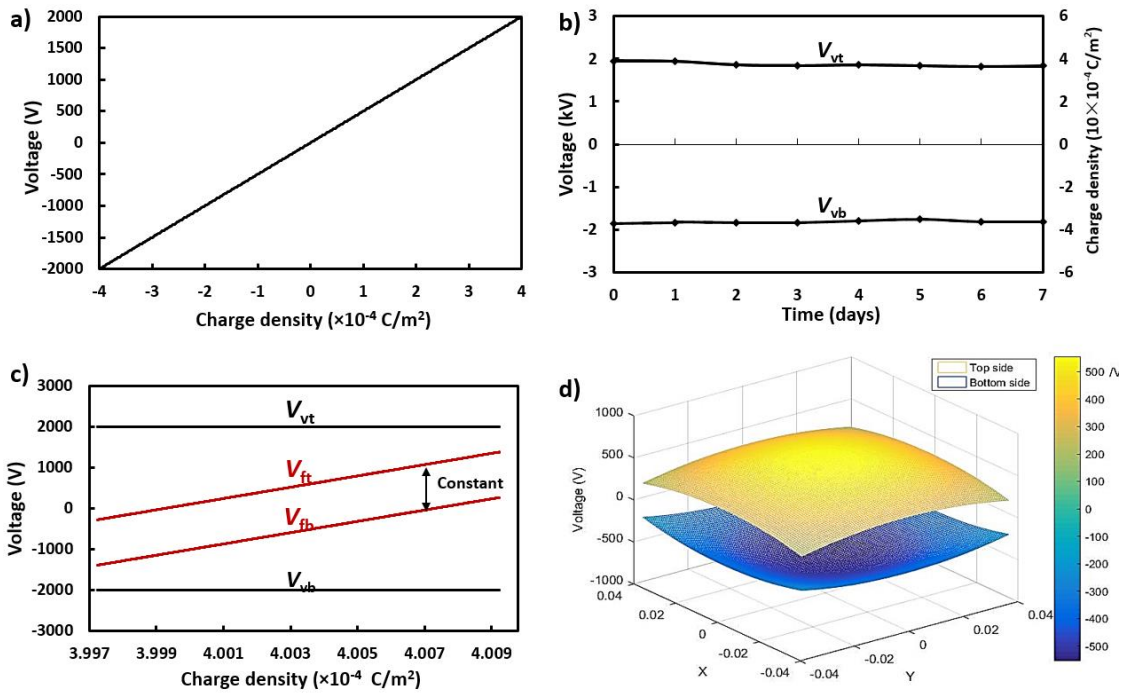

Figure 3.10 a) Calculated relationship between the surface charge density (σ) and the voltages measured by voltmeter (V_v). b) Decay profiles of V_v and σ of a corona charged 50-μm-thick PP film. c) The effect of σ_f on V_{vt}, V_{vb}, V_{ft}, and V_{fb}.

According to our experimental results, $V_1 \approx -V_2$ and $\sigma_1 \approx -\sigma_2$; the top side of the polymer film shares the same polarity with the corona, and the bottom side is oppositely charged. For polymer film charged with the grid voltage of 2 kV, the magnitude of surface voltage measured by voltmeter should be ~2 kV. Combination of Eq. 3.3 to Eq. 3.7 indicates that the surface charge density on the top side of the sample in Figure3.10b is $\sigma_1 = 4.003\times10^{-4}$ C/m^2, and $\sigma_2 = -4.003\times10^{-4}$ C/m^2 on the bottom side.

If we assume that the corona charging is based on polarization,[97] the charges of the top side should have opposite sign compared with the corona, contradictory to our experimental result. If we assume that the majority charges are obtained through charge

injection from each side of the film, the top side should share the same polarity with the corona, and the bottom side has the opposite inducted charges form the grounded electrode, fitting well with our observations. Polarization may still take place in the interior, but its contribution to surface voltage is much less than that of charge injection.

In the above discussion, σ_1 and σ_2 are represent a dipolar charge distribution, since they have opposite signs. It explains why ΔV_f and its ratio to voltmeter reading are constant over time for different films. More details will be elaborated below.

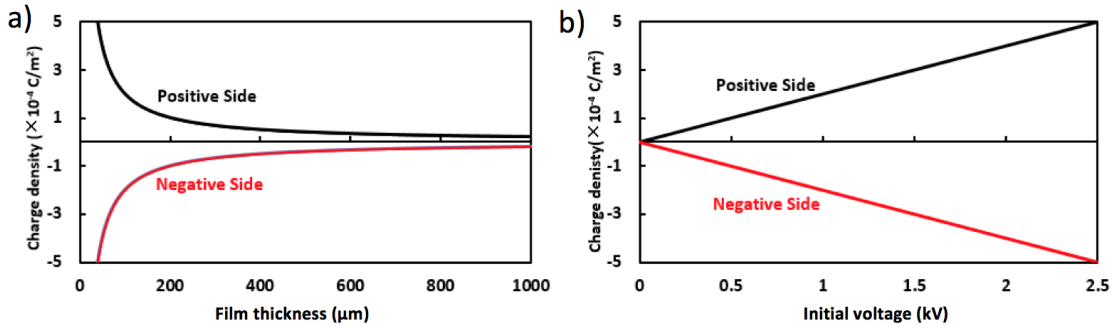

Figure 3.11 a) The relationship between the surface charge density and the film thickness. b) The relationship between the surface charge density and the initial surface voltage. Size: 3 inch × 3 inch. Charge uniformly distributed.

From Eq.3.4 to Eq.3.6, we can obtain the relationship among the surface charge density, the film thickness, and the grid voltage, as shown in Figure 3.11. With the same measured surface voltage, a thinner film must have a higher charge density, since the distance between the oppositely charged top and bottom layers is shorter. With a given film thickness, the surface charged density is proportional to the initial voltage. It is consistent with our experimental results that the surface voltages of thinner films or films with higher initial potentials decay faster. That is, polymer film of a larger surface

charge density tends to have a higher voltage decay rate, which can explain the well-known "cross-over" phenomenon.

3.3.4.2. Effects of free charges on surface voltage

While $\sigma_1 \approx -\sigma_2$, in an actual film sample there would always be a relatively small difference between them, denoted as σ_f; i.e. $\sigma_f = \sigma_1 + \sigma_2$. It will be referred to as free charge in the following discussion; its magnitude is much smaller than the dipolar charge density σ_1 and σ_2. However, even a small σ_f can cause a large fieldmeter measurement result of surface voltage.

As shown in Figure 3.1a, the fieldmeter reading captures the electric potential of the entire charged film. Fieldmeter measurement is conducted at a constant distance z_{field} (25 mm in our experiments) away from the film surface. Based on Eq. 3.3, the fieldmeter result on both sides of the film can be respectively calculated as

$$V_{f,1} = V(\sigma_1, z_{field}) + V(\sigma_2, (z_{field} + t)) \quad \text{(Eq. 3.8)}$$

$$V_{f,2} = V(\sigma_2, z_{field}) + V(\sigma_1, (z_{field} + t)) \quad \text{(Eq. 3.9)}$$

In order to examine the effects of σ_f, we set σ_2 as a constant value, and vary σ_1 in a narrow range around $-\sigma_2$. The variations of surface voltages measured by voltmeter and fieldmeter associated with the slight change in σ_1 are shown in Figure 3.10c. The fieldmeter measurement result changes drastically in a broad range and can even change its polarity, with a σ_f as small as $0.1\%\sigma_2$. For example, when σ_1 changes from 3.997×10^{-4} C/m^2 to 4.009×10^{-4} C/m^2, V_{ft} increases from -268 V to 1384 V and V_{fb} varies

from -1369 V to 270 V. Note that the potential difference between the top side and the bottom side (ΔV_f), the voltmeter measurement result (V_v), and the R ratio do not change with σ_f, fitting well with the experimental phenomena.

According to Eq. 3.1, the Columbic potential at (x', y', z') caused by a uniformly charged layer at (x, y, 0) is

$$V_{arb}(x', y', z', \sigma) = \int_{-y\prime-L/2}^{L/2-y\prime} \int_{-x\prime-L/2}^{-x\prime+L/2} \frac{\sigma}{4\pi\varepsilon_0\sqrt{x^2+z^2+y^2}} \mathrm{d}x\,\mathrm{d}y \qquad \text{(Eq. 3.10)}$$

Integration of Eq. 3.10 gives

$$\begin{aligned} V_{arb}(x', y', z', \sigma) = & \sum_{j=1,-1}\sum_{k=1,-1}(j\cdot k)\ln\left[\frac{j\cdot L}{2}+\sqrt{z'^2+\left(\frac{k\cdot L}{2}-x'\right)^2+\left(\frac{j\cdot L}{2}-y'\right)^2}-y'\right]\left(-\frac{L}{2}-x'\right) \\ & + \sum_{j=1,-1}\sum_{k=1,-1}(j\cdot k)\ln\left[\frac{j\cdot L}{2}+\sqrt{z'^2+\left(\frac{j\cdot L}{2}-x'\right)^2+\left(\frac{k\cdot L}{2}-y'\right)^2}-x'\right]\left(-\frac{L}{2}-y'\right)-z' \\ & \cdot \sum_{j=1,-1}\sum_{k=1,-1}(j\cdot k)\,\mathrm{ArcTan}\left[\frac{\left(\frac{j\cdot L}{2}-x'\right)\left(\frac{k\cdot L}{2}-y'\right)}{z'\sqrt{z'^2+\left(\frac{j\cdot L}{2}-x'\right)^2+\left(\frac{k\cdot L}{2}-y'\right)^2}}\right] \end{aligned} \qquad \text{(Eq. 3.11)}$$

Hence, the electrostatic potential caused by square electret with dipolar charge distribution can be obtained as

$$V_f(x', y', z') = V_{arb}(x', y', z', \sigma_1) + V_{arb}(x', y', (z'+t), \sigma_2) \qquad \text{(Eq. 3.12)}$$

The surface voltage of a 3 inch × 3 inch film charged with 2 kV grid voltage is calculated by Eq. 3.12 and the results are shown in Figure 3.12. We assume that the charges injected by corona charging distribute on the film surface uniformly, and the polarities of the front and back sides are opposite. Figure 3.12a shows the potential distributions with σ_f=0, at z=25 mm or z=-25 mm. It can be seen that the potential near edge is lower than that of at central area, and the distribution is symmetric on each side.

The potential distribution at plane $Y = 0$ is shown in Figure 3.12b. Positive potential is indicated by the yellow color, and negative potential is in blue. The potential decreases with z and the distance to the center. When σ_f=0, the potential measured at z=±25 mm are 0.556 kV and -0.556 kV, respectively. If a charge density of σ_0=0.362 μC/m^2 is added onto the top side of the film, the potential distribution will significantly change (Figure 3.12c); the potentials at z=±25 mm become, respectively, 1.056 kV and -0.056 kV; the yellow positive area is broader than the blue negative area. If the added charge density is further increased to 0.724 μC/m^2 (Figure3.12d), the potential on both sides of the film rise by another 0.556 kV; at the top side, the positive potential is higher and the positive-potential area is larger, and at the back side the negative-potential area is much smaller. At z=-25 mm, the polarity even switches from -0.056 kV to +0.444 kV. If -0.362 μC/m^2 is added on the back side, the potential at top side changes from 0.556 kV to -0.056 kV and larger negative-potential areas can be seen on both sides (Figure 3.12e). If -0.724 μC/m^2 is added on the back side, the negative potential is more intense and its area is broader (Figure 3.12f). Noted that 0.362 μC/m^2 is just ~0.1% of the charge density caused by corona charging. Such a small density of free changes can already drastically change the absolute values of the surface voltages on both front and back sides, even their polarities; however, the voltage difference across the film thickness is not affected, as the much larger corona induced charge density change much slower.

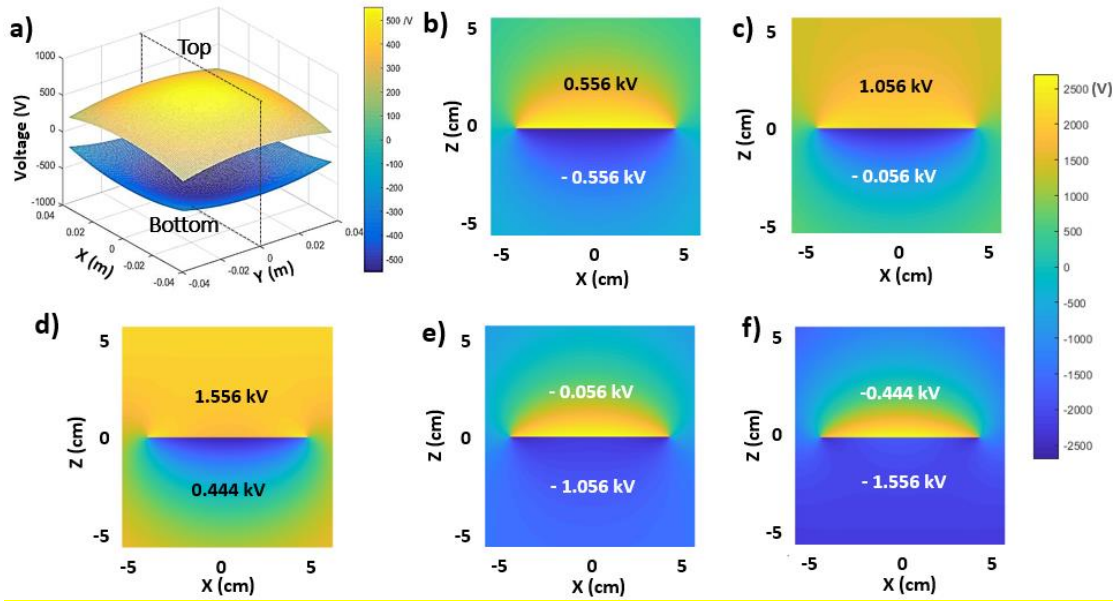

Figure 3.12 Modeling of potential distribution of 3 inch × 3 inch electrified polymer film with V_v=2 kV: a) Potential distribution on each side of the film, 25 mm away from the film surface. Potential distributions of the film at plane Y=0 in the central 5 cm × 5 cm area of the film, when b) σ_f =0, c) σ_0=0.362 μC/m^2 is added to the top side, d) σ_0=2×0.362 μC/m^2 is added to the top side, e) σ_0=-0.362 μC/m^2 is added to the top side, f) σ_0=-2×0.362 μC/m^2 is added to the top side.

3.4 Conclusion Remarks

Upon corona charging, various polymer films have different surface voltage stability. Among the tested materials, the voltage decay rates of PP and PET are much lower than those of PC, FEP, and PMMA. Surface voltage of thicker film tends to be more stable than thinner film, yet this effect saturates as the thickness increases. When initial surface voltage rises with the grid voltage, the voltage decays faster. Charging polymer film at $T > T_g$ leads to an initial surface voltage much lower than the grid voltage, while the decay rate is similar as that of films charged at $T < T_g$.

The fieldmeter measurement results of initial surface voltages of polymer films charged under nominally same condition can vary in a broad range. Remarkably, the potential differences between the top and the bottom sides of the films are nearly and do not vary much over time, even with a relatively large voltage decay; moreover, the ratio of the voltage difference measured by fieldmeter to the surface voltage measured by voltmeter is independent of the film material, charging condition, and decay rate and time. This phenomenon can be explained by the model of dipolar charge injection, which is confirmed by the short-circuit discharge experiment. In this framework, the well-known "cross-over" phenomenon can be attributed to that a film with a larger surface charge density tends to have a higher voltage decay rate. While the dipolar charge distribution results in stable surface voltages on both sides of the film, a small variation in free charge, which can be around 0.1% of the dipolar charge density, may drastically vary the absolute value of surface voltage, even changing the polarity.

3.5 Acknowledgment

This chapter, in part, is a reprint of the material prepared to be submitted for publication. Ying Zhong, Rui Kou, Lewis Fowlergerace, Meng Wang, and Yu Qiao. Corona charging: Dipolar charge distribution and potential shifting. The dissertation author was the primary investigator and first author of the paper.

Chapter 4 Contact electrification of polymer films

4.1 Introduction

In addition to corona charging[83] and thermal charging,[75] contact electrification (CE),[125] often also referred to as triboelectrification, is another important process that involves charge transfer at surfaces of electrically nonconductive materials.[157] CE happens when two nonconductive surfaces are separated.[134] It is a major mechanism that causes the free charges discussed in Chapter 3, responsible to the potential shifting behaviors of corona charged polymer films. With a surface density of free charges as low as 0.1% of that of dipolar charges, the absolute value of surface voltage can vary in a broad range and even the polarity may change.

The first experimental demonstration of CE was probably performed by Thales more than 2500 years ago, as he moved amber against wool.[158] Since then, it has been discovered that CE played an important roles in a large number of areas: for instance, CE is a major reason of dust accumulation;[159-161] it may result in breakdown of electric insulting materials;[162] CE can trigger explosion if sufficient charges are accumulated;[163] it offers powerful mechanisms for advanced filtration, materials selection,[53, 164] electrophotography, enhanced adhesion; surface conditioning;[165, 166] it was recently argued that CE might be a key factor in the origin of life associated with synthesis of amino acids.[167]

There are a few models and theories of CE; each captures a subset of the wide variety of observed phenomena.[128] The fundamental driving force of charge transfer is still under investigation[125, 133] and it has not been fully conclusive what species are actually being transferred during CE; possible candidates, such as electrons,[168] radicals,[133] ions,[134] and atoms and molecules,[169] are being studied. Moreover, testing data and discussions in literature on the influence of temperature and humidity may not be always compatible with each other.[134]

According to the theory of electron transfer, when a metal and an insulator contact each other, their Fermi levels are equalized upon touching. Electrons tend to transfer from the metal side to the dielectric material side across the interface.[170, 171] According to the theory of radical transfer, the distribution of "mosaic" charges is tightly relate to the free radicals on the surfaces, which explains quite well the electrification at interfaces of identical materials.[130] In the ion transfer theory, humidity is the dominant factor; as water molecules are ionized by the strong electric filed at the interface, ions with different polarities are left on opposite surfaces.[134] In all the theories, the surface potential is governed by the net surface charge density.[133] The impurity, contamination,[172] and defects in the materials may also have critical effects.[173] On a highly charged surface, e.g. when the surface charge density is ~1 $\mu C/m^2$, the charging process and the charge distribution would be quite sensitive to the adjacent defects and as a result, the repeatability of CE can be poor.[125]

While CE commonly occur on surfaces of nonconductive materials, it can also be observed on conductors and semiconductors, where the major difference from nonconductive materials is that the charges dissipate much faster.[128] CE takes place at

interfaces among solids, liquids, and gases.[174] CE of solid interfaces can be analyzed through triboelectric series.[175, 176] As one material is placed in contact with its counterpart, the more electronegative one tends to carry negative charges, and the other side of the interface would be positively charged.[177] Note that the series depends on a large number of materials and environmental parameters, such as surface treatment, contact and separation rates, temperature, humidity, etc.[175] When liquid flows along a solid surface, the liquid and the solid may obtain net charges of different polarities.[178] If the electricity is harvested, it may power commercial LED.[136],[179] Comparing with solid-solid CE,[180, 181],[1] liquid-solid CE is generally more reproductive, since the actual contact area is controllable and the liquid composition is more homogeneous.[182, 183]

Because free charges may induce polarity change of electrified polymer films, as discussed in Chapter 3, and CE can lead to a significant CE charge density, it offers a possible approach to precisely control the surface voltage of electret, specifically rendering the potential distribution purely dipolar. In this chapter, we treated various polymer films with selected liquids and measured their surface voltages (V_{CE}). The stability of V_{CE} was evaluated. We also discovered that if CE between liquid and polymer took place in an external electric field, the potential of polymer film could be precisely adjusted. A series of experiments were conducted to examine the effects of the strength of external electric field. The repulsive forces among contact-electrified films were characterized.

4.2 Experimental

4.2.1 Contact electrification between polymer film and liquid

Contact electrification (CE) experiments were carried out on a variety of liquids and polymer films. Isopropyl alcohol (IPA) solutions were prepared by ultrasonically mixing IPA with DI water for 5 min. The IPA concentration, C_{IPA}, was 0, 5, 10, 20, 30, 50, or 100 vol.%. Aqueous solutions of sodium chloride (NaCl) were prepared by ultrasonically dissolving NaCl in DI water for 5 min; the NaCl concentration, C_{NaCl}, was 0, 0.5, 1, 2, 5, or 10 wt.%. 125-μm-thick PET, PC and FEP films were cut into 3 inch × 3 inch squares. They were ultrasonically cleaned in IPA for 5 min and in DI water for another 5 min, followed by drying in a vacuum oven at 70 ºC for 24 hr. Immediately before testing, the polymer film was exposed to a static eliminator (Keyence SJ-F2000) for 10 sec; the initial surface voltage was measured by a fieldmeter (Simco-ion FMX-003) from both sides and confirmed to be 0. The polymer film was then vertically immersed in a selected liquid for 3 sec and pulled out, with the velocity of ~2.5 cm/s. After the liquid has evaporated, the CE-induced surface voltage (V_{CE}) was measured by the fieldmeter, with the probe distance being z_{field} = 25 mm. Since the charging conditions were the same on both sides, the surface voltage measurement result was not dependent on the measurement direction. At least 5 samples were tested for each parameter setting.

In another set of tests, we simultaneously applied different NaCl solutions on the front and the back sides of the same film, respectively. The NaCl concentration,

C_{NaCl}, of the solutions on both sides of the film differed by 0-10 wt%. The two liquids were respectively applied on the two sides of the film through rinsing. At least 5 samples were tested for each parameter setting.

To test the stability of V_{CE}, all the samples were preserved in an environmental chamber, with the relative humidity (RH) being 45%. Both sides of the films were exposed to air, not in contact with any solid or liquid objects. Their surface voltages were measured by the fieldmeter every 24 h for 7 days.

4.2.2 Effects of external electric field

In our CE tests, we noticed that polymer films rinsed by IPA tended to have zero surface voltage, if the IPA rinsing was performed in an external electric field, the surface voltage might change. CE-induced surface voltage under the influence of external electric field will be denoted as V_{CE}' in the following discussion.

The polymer films under investigation were 125-μm-thick 3 inch × 3 inch PET layers. An electric field was produced by a contact-electrified 125-μm-thick 5.5 inch × 5.5 inch FEP film. The electric field $\boldsymbol{E}$ could be altered by adjusting the surface potential (V_f) of the FEP film and its distance to the PET film (d_E). The PET film was fully covered by a liquid layer of IPA and placed in parallel concentrically to the charged FEP film, with d_E being 25 mm, 50 mm, 75 mm, or 100 mm. After ~7 min, the IPA liquid layer fully evaporated. The surface potential of the treated PET film (V_{CE}') was measured by the fieldmeter, with the probe distance of 25 mm.

4.2.3 Repulsive force between contact-electrified polymer films

A measurement system was developed to characterize the repulsive forces among contact-electrified polymer films, F (Figure4.1). It consisted of an analytical balance (Ohaus Explorer Scale-220 grams with resolution of 0.0001 grams), two polycarbonate (PC) racks as sample holders, and a glass shielding cage. Before testing, the surface electrostatic of all the components was eliminated by an electrostatic eliminator. The bottom rack was fixed on the sample plate of the balance. The upper rack was affixed on the ceiling of the cage. The height of both racks was more than 5 inch, to avoid the influence from the environment. When the rack size changed, the changes in measurement data were less than 1%, as long as the rack length was more than 5 inch. The distance between the upper and the lower racks was 3 mm.

A set of 25-μm-thick 3 inch × 3 inch PC films were contact electrified by various liquids to obtain different surface voltages, through a similar procedure as in Section 4.2.1. One electrified PC film was first placed on the bottom rack, and the scale was calibrated to zero. Another PC film of the same surface voltage was then attached onto the upper rack, with the edges aligned with the bottom film. The samples were carefully handled such that their surfaces were not in contact with any solid or liquid objects, except for the holding points of the racks.

The measurement results of the balance were recorded. Each pair of PC films were measured for 4 times, with the orientation of the upper film being turned by 90° clockwise every time. At least 3 pairs of samples were measured for each parameter setting.

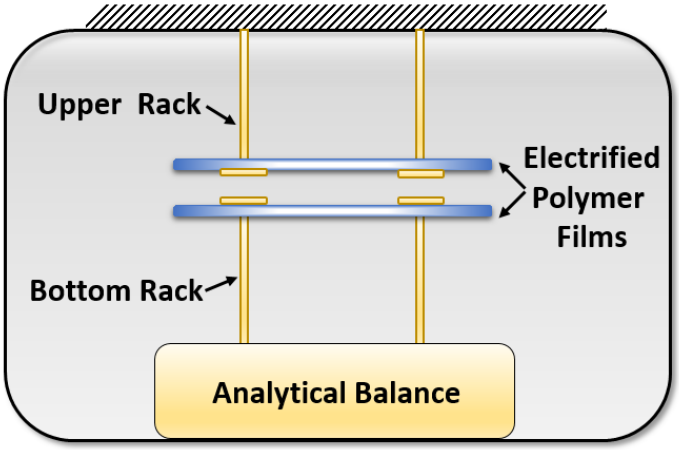

Figure 4.1 Schematic of the repulsive force measurement system

4.3 Results and discussion

4.3.1 Contact electrification between polymer films and liquids

When a PC film is dipped in DI water, the CE-induced surface voltage can be quite high, around -1.5 kV. After the same PC film is immersed in IPA, the surface voltage would be low, undetectable by using the fieldmeter. The contact angle between PC and water is ~82°, and ~75° between PET and water. After immersion in water, no residual liquid remains on the film surface when the surface voltage is measured. IPA wets PC films quite well; after immersion, we need to wait for at least 7 min for the IPA to entirely evaporate from the film surface.

Figure 4.2 shows the results of V_{CE} of PC, PET and FEP films with mixtures of IPA and DI water, with various C_{IPA}. After contacting with DI water, PC, PET, and FEP films would develop significant surface voltages around -1.5 kV, -1.0 kV, and -6.5 kV,

respectively. The corresponding charge density (σ) can be calculated as -1.06 μC/m^2, -0.73 μC/m^2, and -0.47 μC/m^2, respectively, by using Eq. 3.3.

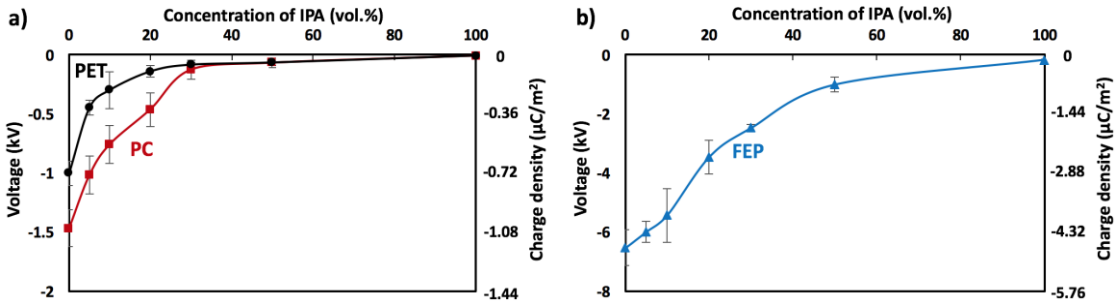

Figure 4.2 Influence of IPA concentration (C_{IPA}) on the surface voltage (V_{CE}) of: a) PC and PET films, and b) FEP films.

Addition of 5 vol.% IPA into the liquid reduces V_{CE} of PC and PET by ~30% and ~55%, respectively. When C_{IPA} is increased to 10 vol.%, V_{CE} is reduced to -0.76 kV (σ = -0.55 μC/m^2) for PC and -0.30 kV (σ=-0.22 μC/m^2) for PET, respectively. From C_{IPA} = 10 vol.% to C_{IPA} = 30 vol.%, PC films demonstrate a larger reduction in V_{CE} than PET films. Eventually, when C_{IPA} > 30 vol.%, the surface voltages of both PC and PET films converge to below ~0.1 kV. From Figure 4.2b, it can be seen that with DI water, FEP films develop a much higher V_{CE} than PC and PET films, around -6.55 kV. The surface voltage decreases rapidly as the IPA concentration rises. When C_{IPA} = 5 vol.%, V_{CE} is -6.00 kV (σ=-4.34 μC/m^2); when C_{IPA}=10 vol.%, V_{CE} is lowered to -5.43 kV; when C_{IPA}=20 vol.%, V_{CE} is largely decreased to -3.47 kV. However, even when the IPA concentration is as high as 30-50 vol.%, the surface voltage of FEP is quite high, ranging from -2.48 kV to -1.02 kV.

Figure 4.3 shows the surface voltage measurement results of CE between polymer films and aqueous solutions of NaCl. Compared to DI water, as 0.5 wt.% NaCl

is added, there is a sharp decrease in V_{CE} of both PC and PET films: V_{CE} of PC is reduced from -1.47 kV (σ=-1.06 μC/m^2) to -0.57 kV (σ=-0.41 μC/m^2); V_{CE} of PET is reduced from -1.00 kV (σ=-0.72 μC/m^2) to -0.66 kV (σ=-0.48 μC/m^2). When C_{NaCl} exceeds 10 wt. %, V_{CE} of PC and PET is lowered to less than -0.10 kV. For FEP films, V_{CE} reduces relatively smoothly as C_{NaCl} increases; when C_{NaCl} is 10 wt. %, V_{CE} of FEP film remains at -2.12 kV, higher than those of PET and PC films.

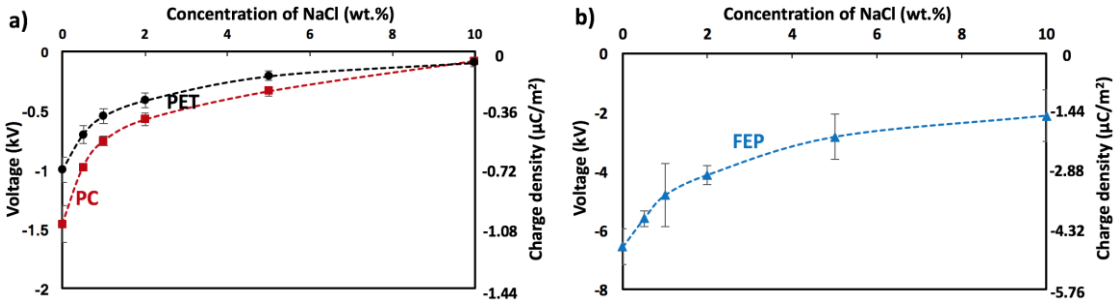

Figure 4.3 Influence of concentration of NaCl (C_{NaCl}) on the surface voltage (V_{CE}) of: a) PC and PET films and b) FEP films.

The testing data indicate that by adjusting liquid composition, we can control V_{CE} in broad ranges: -1.5 kV to 0 for PC films; -1.0 kV to 0 for PET films; and -6.5 kV to 0 for FEP films. The surface voltages of PC and PET films are sensitive to C_{IPA} and C_{NaCl} when they are in the ranges from 0 to 30 vol.% and 0 to 10 wt.%, respectively. For FEP films, V_{CE} is highly controllable in broader ranges of C_{IPA} (0 to 100 vol.%) and C_{NaCl} (0 to 35.9 wt.%); 35.9 wt% is the solubility of NaCl in DI water at room temperature. The relationship between V_{CE} and the liquid composition is nonlinear, with a higher sensitivity when the IPA or NaCl concentration is relatively low.

4.3.2 Stability of surface voltage of contact-electrified polymer film

The stability of the CE-induced surface voltages of polymer films are shown in Figure 4.4. Polymer films with higher initial surface voltage (V_i) tend to have higher surface-voltage decay rates, especially in in the first 72 hours. For PC films (Figure 4.5a), V_i is around -1.5 kV (CE with DI water), -1.0 kV (CE with aqueous solution of 5 vol.% IPA) or -0.57 kV (CE with aqueous solution of 0.5 wt.% NaCl). After 72 hours, the surface voltages reduce by 37%, 36%, and 30%, respectively. After 7 days, the surface voltages decrease to -0.71 kV, -0.42 kV, and -0.26 kV, respectively. The surface-voltage decay rates of PET films (Figure 4.5b) are somewhat similar with those of PC films, except that V_i of PET films induced by aqueous solutions of 0.5 wt.% NaCl is higher while V_i induced by DI water and aqueous solutions of 5 vol.% IPA are lower. The initial surface voltages (V_i) of PET films are around -1.0 kV, -0.45 kV, and -0.66 kV when the working liquids are DI water, aqueous solution of 5 vol.% IPA, and aqueous solution of 0.5 wt.% NaCl, respectively. After 72 hours, the surface voltages decrease by ~35%, ~24%, and ~25%, respectively; after 7 days, the surface voltages are lowered to around -0.4 kV, -0.3 kV, and -0.4 kV, respectively. PC film treated with 5 vol.% IPA aqueous solution shares similar V_i (-1 kV) with PET film treated with DI water; after 7 days, they have similar final surface voltages around -0.4 kV. That is, V_i is the dominant factor of the surface-voltage decay rate, and the effects of polymer properties are secondary.

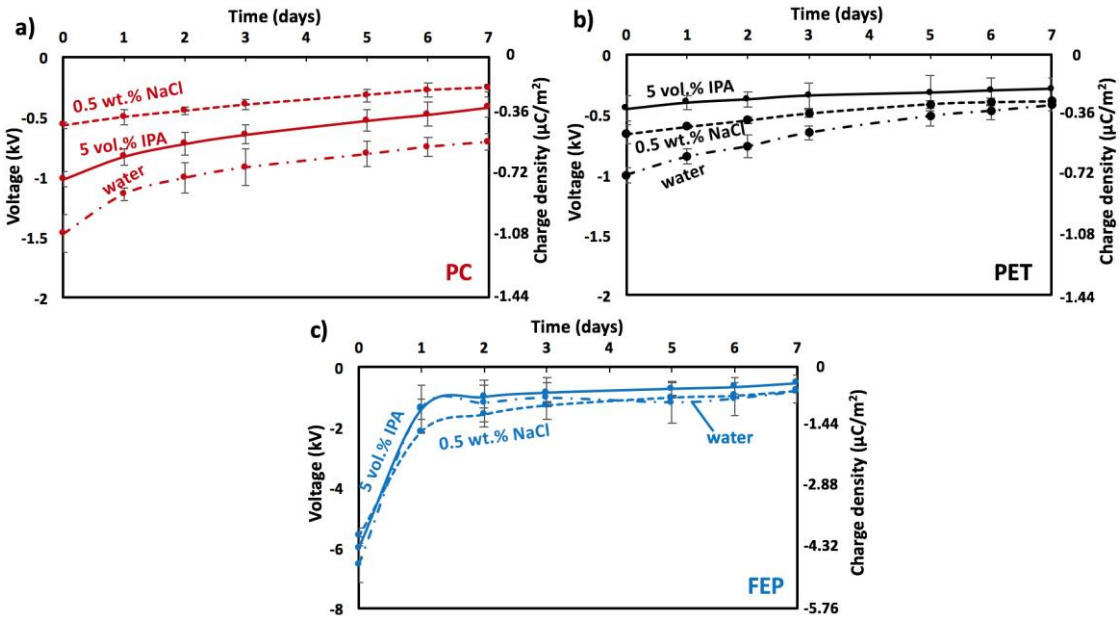

Figure 4.4 Decay of CE-induced surface voltage in 7 days: a) PC films, b) PET films, and c) FEP films. The liquid phase is DI water, aqueous solution of 5 vol.% IPA, or aqueous solution of 0.5 wt.% NaCl.

The V_i of FEP films are much higher than those of PC and PET films by nearly -6 kV, with the same liquid phases. In all the cases, the surface voltages of FEP films rapidly decrease to below -2 kV after 24 h, after which the surface-voltage decay rate, dV_{CE}/dt, converges to the similar level as PC and PET films. Again, this testing result suggests that V_i is mainly determined by the liquid composition and the polymer specie, and dV_{CE}/dt is governed by V_i.

Upon contact with neat IPA, the surface charges on polymer film are neutralized, so that V_i becomes 0; if the liquid phase is DI water, the polymer film would gain negative charges, and the surface voltage of PC is higher than that of PET. With an aqueous solution of IPA or NaCl, the liquid composition strongly influence V_i; the initial surface voltage is lowered to near zero when the IPA or NaCl concentration exceeds 30

vol.% and 10 wt.%, respectively. Under the same contact electrification condition, FEP film has a much higher V_i than PC and PET films. For all the polymer films, dV_{CE}/dt is mainly related to V_i; other factors, such as the liquid and polymer materials, are secondary. In general, V_{CE} can be adjusted by choosing appropriate liquid composition and its decay rate is faster than that of corona charged films.

4.3.3 Simultaneous contact electrification with multiple liquids

Polymer film can be simultaneously treated by two different liquids on both sides, leading to distinct V_i at each surface. As shown in Figure 4.5a, if one surface of PC film is thoroughly rinsed by DI water and the other is exposed to aqueous solution of NaCl, with C_{NaCl} being 0.5 wt.%, 1 wt.%, 2 wt.%, 5 wt.%, or 10 wt.%, the surface voltages measured by fieldmeter, V_i, are -1.46 kV, -1.28 kV, -1.26 kV, -1.05 kV, -0.86 kV, and -0.66 kV, respectively, exhibiting a similar characteristic as in Section 4.3.2 that a higher NaCl concentration results in a lower surface voltage, yet the magnitude of V_i tends to be higher than if the same NaCl solution is used at both sides. When DI water is changed to NaCl solution, V_i would be reduced as the NaCl concentration increases on either side. Similar phenomena are observed for FEP films (Figure 4.6b), while V_{CE} of FEP is lower than those of PC films charged with the same NaCl solutions. For all the films, the overall V_{CE} is close the average value of the contributions from both surfaces.

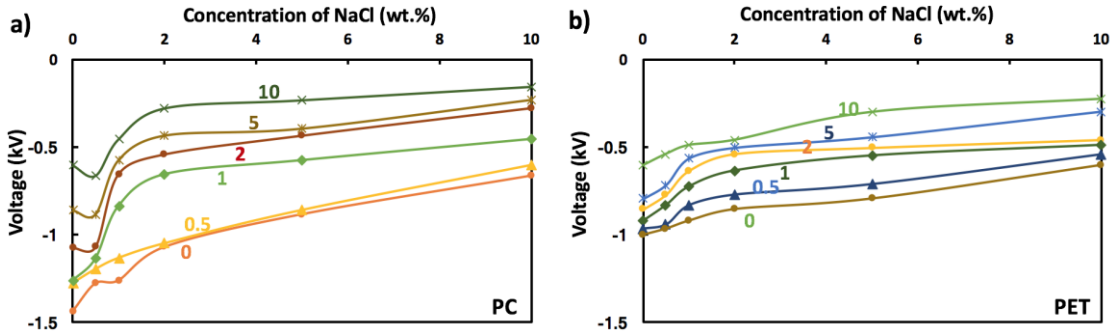

Figure 4.5 Surface voltages of polymer films simultaneously exposed to aqueous solutions of NaCl of different C_{NaCl} on both sides: a) PC films and b) PET films. The horizontal axis shows C_{NaCl} on one side and the numbers indicate C_{NaCl} on the other side.

4.3.3 Effects of external electric field

When a PC or PET film is immersed by neat IPA, the surface charges can be reduced to near zero. During the treatment, because IPA wets polymer very well, the polymer surfaces can be fully covered by a thin layer of IPA and under ambient condition, it takes about 7 min to fully evaporate it. However, if the drying procedure is influenced by an external electric field, V_{CE} would no longer be zero but dependent on the strength of the electric field, E.

As shown in Figure 4.4, FEP film can develop a high VCE upon contact with NaCl solution. We rinsed a 5.5 inch × 5.5 inch 125-μm-thick FEP films in NaCl solution and used it to provide an external electric field for a 3 inch × 3 inch PET film. The surface voltage of FEP film, Vf, was in the range from -1 kV to -7 kV, depending on the CNaCl used for its processing. The PET film was immersed in neat IPA, and placed next to the charged FEP film with its surfaces fully wetted with IPA. The FEP and the PET films were in parallel, with the edges and the centers aligned with each other. The

distance between them ranged from 25 mm to 100 mm, as depicted in Figure4.6. After the IPA layers on both sides of the PET film had entirely evaporated, the surface voltage of PET (VCE′) was measured by a fieldmeter.

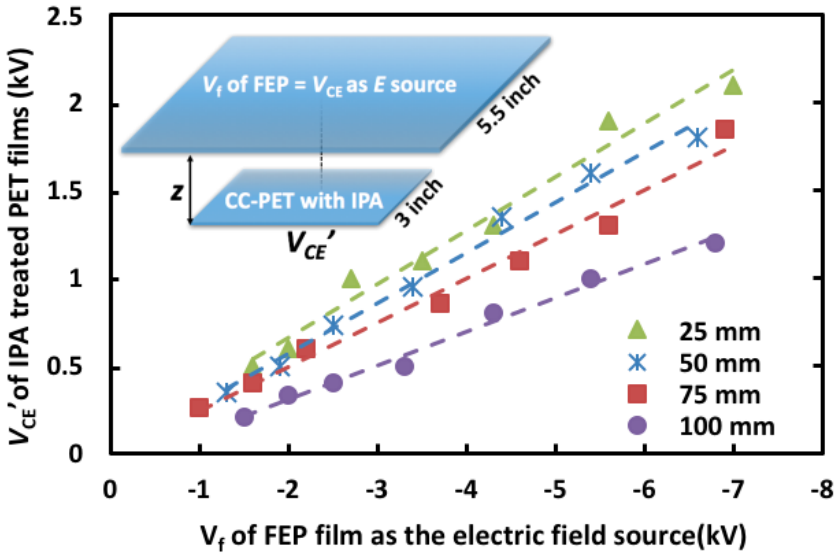

Figure 4.6 The influence of the surface voltage (V_f) and distance (z) of FEP film on the surface voltage of IPA rinsed PET film (V_{CE}'). The FEP film provides an external electric field. The PET-PET distance (z) is 25 mm, 50 mm, 75 mm, or 100 mm. The inset depicts the experimental setup.

It can be seen that V_{CE}' increases nearly linearly with V_f, and decreases as z rises. Remarkably, under all the testing conditions, V_{CE}' is positive, contradictory to the results of aqueous solutions of IPA without external electric field. For instance, if the PET film is placed 75 mm away from the charged FEP film with V_f being -4.6 kV, it would develop a V_{CE}' = +1.1 kV as the IPA layer evaporates.

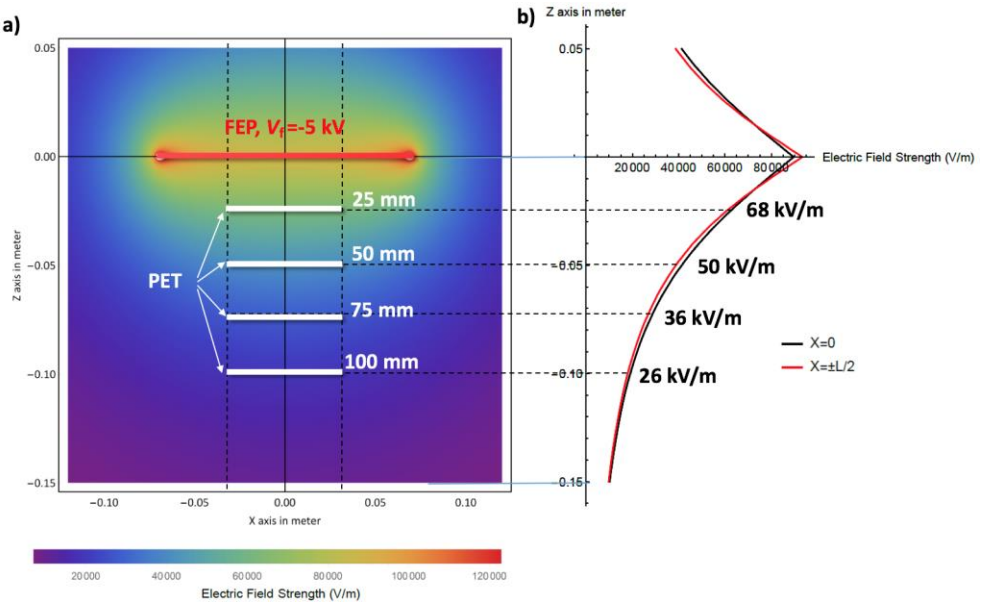

Figure 4.7 The calculated electric field strength of a 5.5 inch × 5.5 inch large FEP film, with V_f = -5 kV: a) along surface Y = 0 and b) at (0, 0, z) and ($\pm L_{PET}$, 0, z) along the Z axis. The size of PET film, L_{PET}, is 3 inch.

From Eq.3.3, when the surface voltage of FEP film (V_f) is known, the corresponding surface charge density (σ_s) can be calculated. According to Eq.3.11, the FEP film would cause a distribution of electric potential in the space surrounding it, $V\ (x, y, z, \sigma_s)$, with (x, y, z) indicating the location. The associated electric field, $\boldsymbol{E}$, can then be obtained as

$$\boldsymbol{E} = -\nabla V \qquad \text{(Eq. 4.1)}$$

and the strength of the electric field is

$$|\boldsymbol{E}| = \sqrt{\left(\frac{\partial V}{\partial x}\right)^2 + \left(\frac{\partial V}{\partial y}\right)^2 + \left(\frac{\partial V}{\partial z}\right)^2} \qquad \text{(Eq. 4.2)}$$

Consider a FEP film with V_f = -5 kV. The surface of FEP film is set at (x, y, 0), with the center of the film being at the origin. According to Eq.3.3, since L_{FEP} =5.5 inch and z_{field} = 25 mm, the surface charge density of the FEP film can be calculated as σ_s = -

1.59 μC/m^2, where L_{FEP} is the FEP film size and z_{field} is the distance of the fieldmeter probe to the film surface. The strength of the electric field surrounding the FEP film, $|\boldsymbol{E}|(x, y, z)$, is shown in Figure4.7a. The electric field strength at (0, 0, 25 mm), (0, 0, 50 mm), (0, 0, 75 mm), and (0, 0, -100 mm) where the PET film would locate are around 68 kV/m, 50 kV/m, 36k V/m, and 26 kV/m respectively, as shown in Figure 4.7b. Since the PET film size is L_{PET} = 3 inch and the electric field strength along ($\pm L_{PET}$, 0, z) is close to that of (0, 0, z), the FEP film is sufficiently large to offer a relatively uniform electric field to the PET film. By changing the distance between the PET film and FEP film or changing the surface potential of FEP film, the electric field strength at the surface of the PET film can be adjusted in a broad range.

The solid lines in Figure 4.8 show the calculated relationship between V_f and $|\boldsymbol{E}|$, when the distance between the PET film and the FEP film (z) is 25 mm, 50 mm, 75 mm, or 100 mm; the dotted lines show the calculated electric field strength at the central point of the IPA treated PET film caused by its own surface voltage, V_{CE}'. It can be seen that at the PET film surface, the magnitude of the strength of local electric field associated with V_{CE}' ($|\boldsymbol{E}_{\mathbf{PET}}|$) is nearly the same as the electric field strength offered by the FEP film ($|\boldsymbol{E}_{\mathbf{FEP}}|$), but the signs are opposite. It should be attributed to that IPA tends to neutralize local electric field. Under the influence of $\boldsymbol{E}_{\mathbf{FEP}}$, it generates surface charges on PET film surface such that $\boldsymbol{E}_{\mathbf{PET}} = -\boldsymbol{E}_{\mathbf{FEP}}$. When E_{FEP} is removed, the residue ions remain on the PET film, resulting in the measured surface voltage, V_{CE}'. That is, external electric field offers an additional degree of freedom to modify CE-induced surface voltage of polymer film. The relatively small difference between the calculated (Figure4.8) and the measured (Figure4.6) E_{PET} may be related to the data scatter of the

fieldmeter, the misalignment of the films, the variation in z, as well as environmental factors such as temperature and humidity.

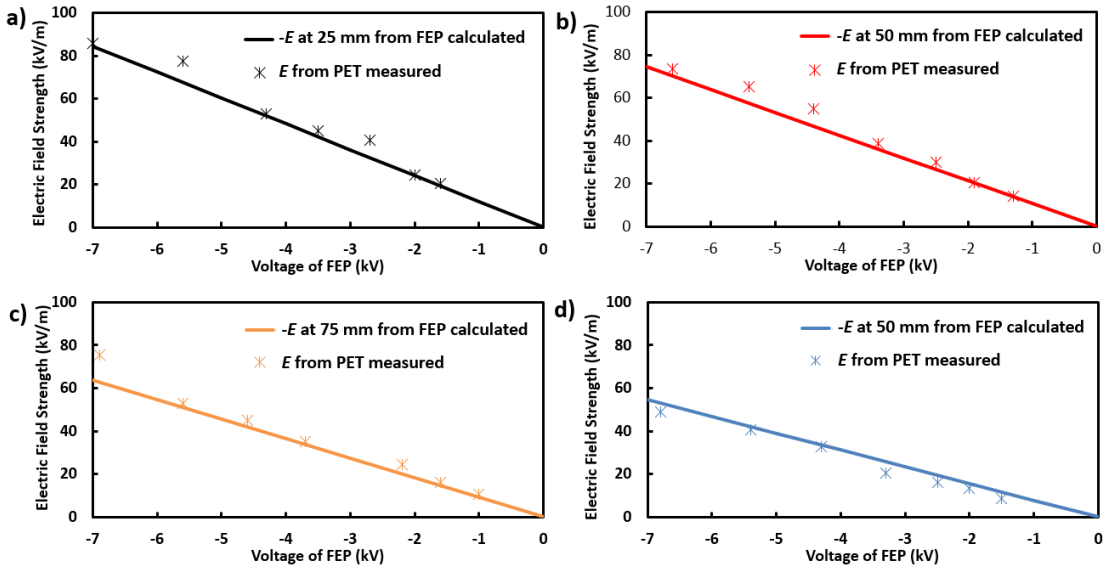

Figure 4.8 The calculated electric field strength produced by the 5.5-inch × 5.5-inch FEP film (E_{FEP}) and the measured electric field strength (E_{PET}) of the 3-inch × 3-inch PET film treated with IPA: a) z = 25 mm, b) z = 50 mm, c) z = 75 mm, and d) z = 100 mm.

4.3.4 Repulsive force between electrified polymer films

Once two polymer films are like charged and placed in proximity, there would be a repulsive force, F, between them. In our measurement, the gap between the two polymer film samples, d, is 3 mm. Based on the fieldmeter-measured surface voltage, V_f, the electric field around the films can be calculated by using Eq. 4.2 and Eq. 3.11, and F can be assessed as

$$F = \int_{-L/2}^{L/2} \int_{-L/2}^{L/2} E_z(x, y, d)\sigma(x, y)\, \mathrm{d}x\, \mathrm{d}y \qquad \text{(Eq. 4.3)}$$

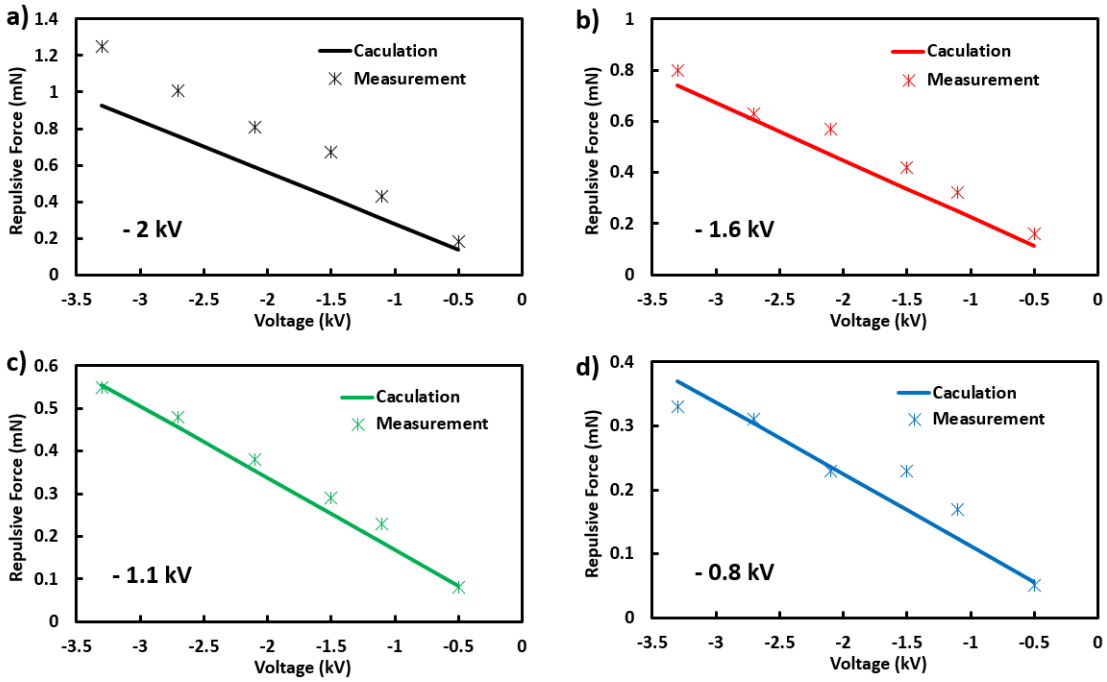

Figure 4.9 The experimental (data points) and the calculated results (solid lines) of the repulsive force between contact electrified polymer films

The measured and calculated results are compared in Figure 4.9. An electrified PC film with V_f = -2 kV (Figure 4.7a), -1.6 kV (Figure 4.7b), -1.1 kV (Figure 4.7c), or -0.8 kV (Figure 4.7d) is used as the bottom layer, and another PC film with the same or a different surface voltage (V_f') is placed on the top, 3 mm away from the first film. The relationship between F and V_f' can be analyzed through Eq.4.2, Eq.4.3, and Eq.3.3. It can be seen that the testing data fit with the theoretical prediction quite well. The repulsive force increases quite linearly with V_f'. The experimental data of F tend to be slightly higher than the theoretical prediction, which may be attributed to the over-assessment of the fieldmeter measurement results of surface voltage and the induction between the two charged films.

4.4 Conclusion Remarks

Surface voltage of generated through contact electrification between polymer film and liquid is dependent on the liquid composition, the polymer material, and the external electric field. Upon contact with DI water, the surface potentials of PC, PET, and FEP films are -1.5 kV, -1.0 kV and -6.5 kV, respectively. When the liquid is neat IPA, the surface voltages of all the films are neutralized to zero. As IPA or NaCl is dissolved in water, the solute concentration has a significant effect on the surface voltage of the electrified film. The surface charge density of the electrified polymer films is on the scale of a fraction to a few $\mu C/m^2$, linear to the surface voltage. Simultaneously treating the two sides of a polymer film with different liquids offers another approach to adjust the surface voltage, as the average effects of the two electrified surfaces dominate. The stability of the surface voltages of contact electrified polymer films is lower than that of corona charged films. After a polymer film is dipped in neat IPA, if the IPA liquid layers evaporate in an external electric field, a significant surface voltage can be developed, which offsets the external electric field along the film surface. The repulsive force between two like charged polymer films is linear to their surface voltages.

4.5 Acknowledgment

This chapter, in part, is a reprint of the material prepared to be submitted for publication. Ying Zhong, Rui Kou, Lewis Fowlergerace, Meng Wang, and Yu Qiao.

Contact electrification and surface potential control of polymeric films. The dissertation author was the primary investigator and first author of the paper.

Chapter 5 Surface voltage control of electrified polymer films

5.1 Introduction

Polymer electrets have find wide applications in a variety of areas. The attraction at oppositely charged polymer surfaces can enhance adhesion,[184] xerography,[185] precision printing,[65, 186], advanced filtration,[187] layer-by-layer assembly,[188] etc. The repulsive forces at like-charged surfaces are immensely useful for colloid processing,[189] prevention of particle agglomeration,[190] particle screening and separation,[191] electrostatic actuation,[192] micro-electromechanical systems processing,[193] friction-free motion,[194] micro-bearings,[195] among others. The interaction among charged objects is determined by their charge density, charge distribution, and size.[196] However, study on precise control of surface voltage is still at its early stage.[197] It is desirable to accurately adjust the surface voltage of electrets so as to achieve target interaction force, through a low-cost, effective, and fast method.

Corona charging offers a high-speed, cost-efficient, and highly effective approach to electrify polymer films.[151] As discussed in Chapter 3, corona charged polymer films exhibits dipolar component of charge distribution, caused by charge injection from both sides of the film. It results in a stable surface-voltage difference across the film thickness (ΔV_f), which can be characterized by using a fieldmeter. In a triode corona charging system with adjustable grid voltage, we can precisely control ΔV_f in a relatively broad range. However, ΔV_f itself does not fully determine the absolute

value of surface voltages on the front and the back sides of the film, as a relatively small amount of free charges can cause drastic changes in surface voltages, even when the free charge density is only ~1% of injected charges. Polarity of surface charges can become different, without changing ΔV_f.

As discussed in Chapter 4, contact electrification (CE) is a convenient method to control the surface voltage associated with free charges, with an excellent cost-performance balance and high throughput rate.[133] However, the reliability and reproducibility of CE treatment can be poor, as the surface voltage is sensitive to a large number of system parameters, such as surface condition of polymer,[172] contact and separation rates,[125] temperature and humidity,[134] choice of the initiative material.[125]-[175] Compared to solid-solid CE, liquid-solid CE is generally more controllable.[136]

In this Chapter, we combine the corona charging (CC) and the contact electrification (CE), so as to precisely control the surface voltage of polymer film. PET and PC films are first corona charged to achieve desired ΔV_f; then, aqueous solutions of IPA or NaCl are used to obtain an appropriate surface voltage, V_{CE}, on the side of the polymer film being treated, without much affecting ΔV_f. The stability of the surface voltages of these films is tested.

5.2 Experimental

5.2.1 Triode corona charging

A triode corona charging system (Figure 2.1) was built up to electrify selected polymer films. The setup consisted of a needle electrode, a 6 inch × 6 inch wire mesh grid, a grounded electrode, heating elements, and two high voltage power supplies. A sharp tungsten needle 0.75-inch-long and 0.059 inch in diameter was employed as the needle electrode. The curvature of the needle tip was ~0.1 mm. A grid was placed between the needle and the sample. It was made of stainless steel 304 wires, with the wire diameter of 0.016 inch and the mesh size #20. The distance between the needle and the grounded plate electrode (d_{ne}) was set as 4 cm, and the spacing between the grid and the electrode (d_{ge}) was 4 mm. The needle voltage (V_n) and the grid voltage (V_g) were controlled by two polarity switchable Glassman FJ Series 120 Watt regulated high voltage DC power supplies, respectively, with the same polarity. The voltages could be adjusted in the range from 0 to ±40 kV for the needle, and from 0 to ±20 kV for the grid.

The polymers under investigation were PET and PC films with the thicknesses of 125 μm. All the films are cut into 3 inch × 3 inch square sheets. They were ultrasonically cleaned first in isopropyl alcohol (IPA) for 5 min and then in de-ionized (DI) water for another 5 min, followed by drying in a vacuum oven at 70 ºC for 24 hr. During charging, a polymer film was placed onto the grounded electrode, with the needle pointing to its center. According to the parameterized study in Chapter 2, V_n was set to -8.5 kV for samples charged at V_g=-1 or -1.5 kV, and -12 kV for samples charged

at V_g=-2, -2.5, or -3 kV. The corona polarity was kept negative; the charging time was 60 sec; the charging temperature was room temperature.

5.2.2 Contact electrification of corona charged films

Aqueous solutions of isopropyl alcohol (IPA) were prepared by ultrasonically mixing IPA with DI water for 5 min. The IPA concentration, C_{IPA}, was 0, 5, 10, 20, 30, 50, or 100 vol.%. Aqueous solutions of sodium chloride (NaCl) were prepared by ultrasonically dissolving NaCl in DI water for 5 min; the NaCl concentration, C_{NaCl}, was 0, 0.5, 1, 2, 5, or 10 wt.%.

Only one side of corona charged film was treated by the NaCl or IPA solution, as the liquid flew through the film surface with a constant rate around 1 mL/s. PET and PC films charged with Vg=-1, -1.5, -2, -2.5, and -3 kV were treated with DI water or IPA; PET and PC films charged with V_g=-2 kV were treated with aqueous solutions with various C_{IPA} or C_{NaCl}. The surface voltage was measured by a fieldmeter (Simco-ion FMX-003) from both sides of the CC and CE (CCCE) treated film, with the measurement distance z_{field}=25 mm. At least 5 samples were tested and characterized for each parameter setting. All the CCCE-treated samples were preserved at ambient temperature in an environmental chamber, with the relative humidity (RH) being 45%. Both sides of the films were exposed to air. The surface voltages of both sides of the films were measured by the fieldmeter every 24 h for 7 days.

5.2.3 Effects of external electric field

The polymer films under investigation were corona charged 250-μm-thick 3 inch × 3 inch PET layers, with V_g =-2kV; the charging procedure was similar to the description in Chapters 2 and 3. An electric field was produced by a contact-electrified 125-μm-thick 5.5 inch × 5.5 inch FEP film. The CE procedure was similar to the description in Chapter 4. Its electric field $\boldsymbol{E}$ was adjusted by altering the surface potential (V_f) and its distance to the PET film (d_E). One side of the PET film was fully covered by a liquid layer of IPA and placed in parallel concentrically to the charged FEP film, with the liquid layer facing the FEP film; d_E was 25 mm, 50 mm, 75 mm, or 100 mm. After ~7 min, the IPA liquid layer fully evaporated. The surface voltage on each side of the treated PET film (V_{CE}') was measured by the fieldmeter, with the probe distance of 25 mm.

5.3 Results and Discussion

5.3.1 IPA treatment of electrified polymer films with various voltage differences

As shown in Chapter 4, the surface voltage of an IPA treated non-electrified polymer film tends to be zero. If the polymer film has been corona charged, Figure5.1 shows the combined result of CC and CE with IPA. In the experiment, both PET and PC films are corona charged with the grid voltage V_g of -1 kV, -1.5 kV, -2 kV, -2.5 kV, or -3 kV. Measured by the fieldmeter, the surface-voltage differences between the top

sides and the back sides of the films (ΔV_f) are around -0.67 kV, -1.00 kV, -1.33 kV, -1.67 kV, and -2.00 kV, respectively. For all the samples, ΔV_f is equal to the surface voltage of the top side (V_{ft}) minus the surface voltage of the back side (V_{fb}); for the films charged by negative corona, ΔV_f<0.

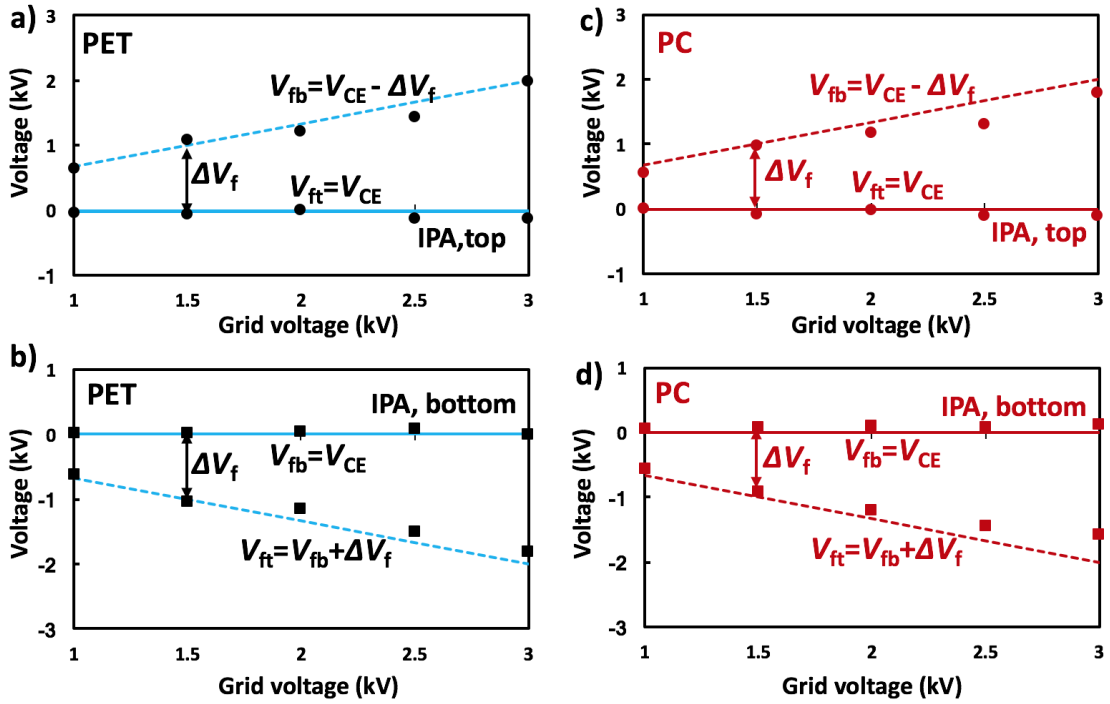

Figure 5.1 IPA treated PET and PC films, which have been corona charged with various grid voltages (V_g=-1 kV, -1.5 kV, -2 kV, -2.5 kV, or -3 kV): a) The top sides of corona charged PET films are treated with IPA; b) The back sides of corona charged PET films are treated with IPA; c) The top sides of corona charged PC films are treated with IPA; d) The back sides of corona charged PC films are treated with IPA.

If the top side of corona charged PET film is treated with IPA (Figure 5.1a), V_{ft} would be reduced to zero, as the surface charges are neutralized. Under this condition, it can be measured that V_{fb} = 0.67 kV, 1.00 kV, 1.33 kV, 1.67 kV, and 2.00 kV for films charged with V_g =-1 kV, -1.5 kV, -2 kV, -2.5 kV and -3 kV, respectively. If the corona charged PET film is treated with IPA on the back side (Figure 5.1b), V_{fb} would be

reduced to zero and V_{ft} changes to -0.67 kV, -1.00 kV, -1.33 kV, -1.67 kV, and -2.00 kV, respectively. The black lines in Figure 5.1 a, b demonstrate the measured data, and the dotted blue lines are the predicted values, agreeing with each other quite well. Similar results are obtained for IPA treated, corona charged PC films, as shown in Figure 5.1c, d.

We also tracked the potential evolution of IPA treated PET films with various ΔV_f (Figure 5.2). The top-side surface voltages, $V_{ft,0}$, of all the PET films are near zero (Figure 5.2a); the bottom-side surface voltage always follows $V_{fb,0}$=-$\Delta V_{f,0}$≈-V_g/1.5. For instance, for films charged with V_g=-2 kV, $V_{ft,0}$ is 0 and $V_{fb,0}$=1.3 kV ≈ -V_g/1.5. Here, the number in subscript indicates the date of measurement after the IPA treatment. After 72 h, for all the polymer films, $V_{ft,3}$ shifts to a negative value, and $V_{fb,3}$ becomes smaller; the values of $V_{ft,3}$ of all the films with different ΔV_f are close to each other, with the average value of -0.22 kV, although initially they are charged with different V_g. Note that $V_{fb,3}$=$V_{ft,3}$-$\Delta V_{f,3}$ is still satisfied, with $\Delta V_{f,3}$ being similar to $\Delta V_{f,0}$, and $\Delta V_{f,0}$ being dependent only on V_g. This phenomenon can be clearly seen in Figure5.2a as the blue lines move downwards to the orange lines, without being affected by ΔV_f. After 7 days (the black lines in Figure5.2.a), V_{ft} keeps moving downwards to $V_{ft,7}$=-0.39 kV, and $V_{fb,7}$ shifts together with it. That is, no matter how much V_g is, the decay in ΔV_f is nearly non-detectable, as V_{ft} and V_{fb} simultaneously change with the same amount.

For PET films treated with IPA on the back sides, the surface voltages measured from the top sides are around ΔV_f, as the back side surface voltages have been reduce to nearly zero. Hence, the surface voltages shift upwards in Figure5.2b. Compared to the opposite shifting direction in Figure 5.2a ($|V_{fb}| > |V_{ft}|$) being taken into consideration,

$|V_{ft}|$ is larger than $|V_{fb}|$, for which the decay of CE-induced free charges on the top sides is the major driving force. Similar behaviors are also observed for PC films, as shown in Figure 5.2c, d.

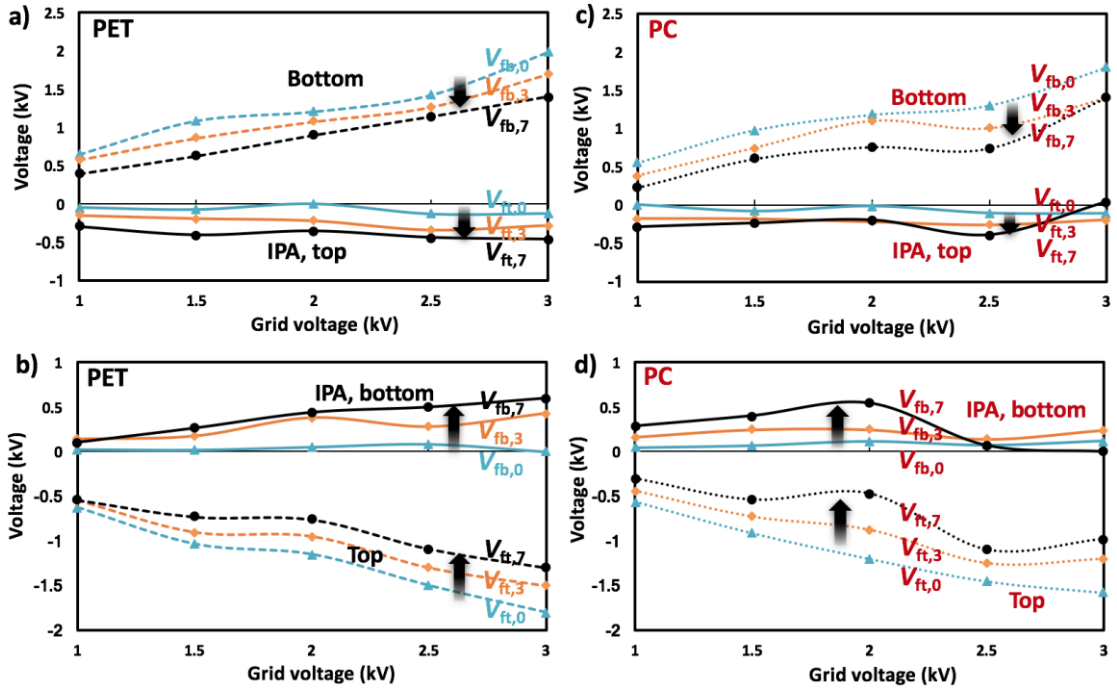

Figure 5.2 The change in surface voltage (day 0, day 3, and day 7) of IPA treated PET and PC films, which have been corona charged with various grid voltages (V_g=-1 kV, -1.5 kV, -2 kV, -2.5 kV, or -3 kV): a) The top sides of corona charged PET films are treated with IPA; b) The back sides of corona charged PET films are treated with IPA; c) The top sides of corona charged PC films are treated with IPA; d) The back sides of corona charged PC films are treated with IPA.

CE-induced charges and CC-induced charges decay simultaneously. The stability of CE-induced free charges is much lower than the stability of CC-induced dipolar charges; i.e. $dV_{CE}/dt >> d\Delta V_f/dt$, consistent with the results of Chapter 4. Figure 5.3 shows the surface-voltage decay of PET and PC films with different ΔV_f treated by IPA. From Figure 5.3a, it can be seen that no matter how much ΔV_f is, if the top side of polymer film is treated with IPA, $V_{ft,0}$ would be almost zero and $V_{fb,0}$ =-ΔV_f. Both V_{ft} and

V_{fb} reduce over time, compatible with Figure 5.1a. The distance between the top line and the bottom line ($\Delta V_{f,i}$, where i = 0,1,2…) is nearly the same for all the samples, as $dV_{CE}/dt >> d\Delta V_f/dt$. Figure 5.3b demonstrates the surface-voltage decay profiles of PET treated on the back sides. Similar behaviors as Figure 5.3a are observed, except that the curves move upwards. The absolute value of the slope for each sample is larger for higher ΔV_f, fitting well with our previous finding. The surface-voltage decay profiles in Figure 5.3c, d are for PC films, having the same characteristics as those of PET films.

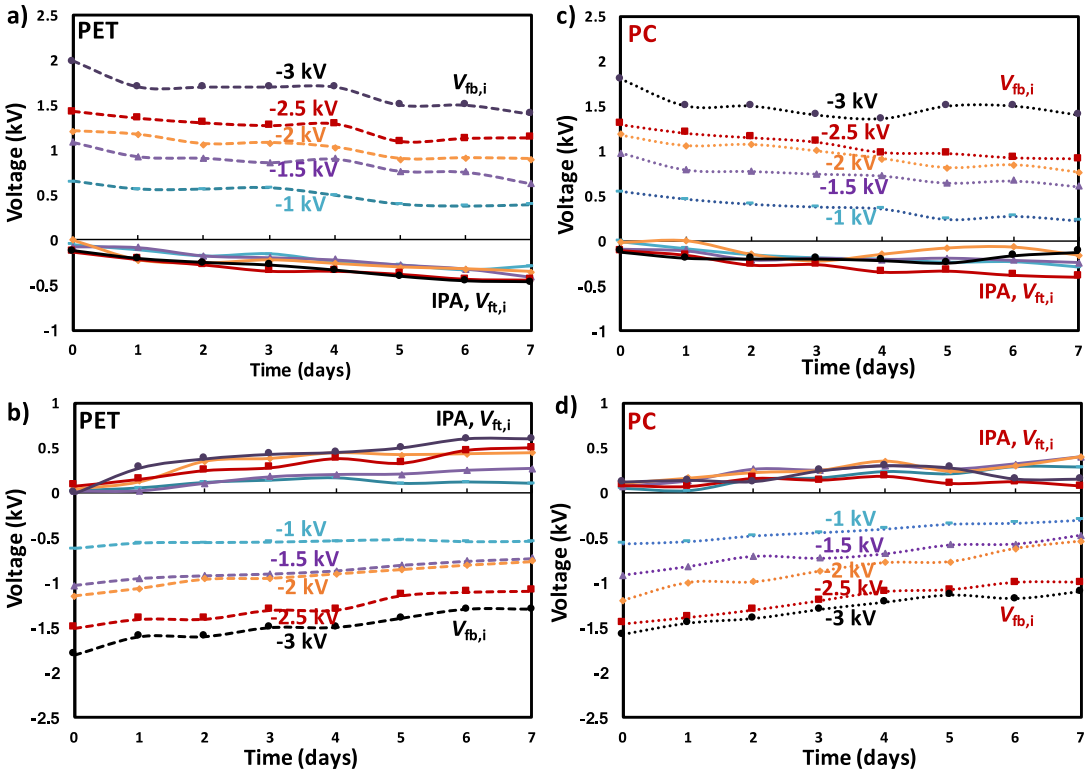

Figure 5.3 Surface-voltage decay of IPA treated PET and PC films that have been corona charged with different grid voltages (V_g=-1 kV, -1.5 kV, -2 kV, -2.5 kV, or -3 kV): a) The top sides of corona charged PET films are treated with IPA; b) The back sides of corona charged PET films are treated with IPA; c) The top sides of corona charged PC films are treated with IPA; d) The back sides of corona charged PET films are treated with IPA.

5.3.2 DI water treatment of electrified polymer films

Figure 5.4 shows the surface voltages of PET and PC films treated with DI water. As discussed in Chapter 4, DI water treatment of non-electrified PET films should lead to a surface voltage around -1 kV. For instance, if the top side of PET film is treated with DI water, it would have a surface potential $V_{ft} \approx$-1 kV; since ΔV_f is stable, the back side would have a surface voltage $V_{fb}=V_{ft}-\Delta V_f \approx -1-\Delta V_f$, as predicted by the blue dotted lines in Figure 5.4a. The measured values are shown by the black lines in Figure 5.4a, fitting well with the predicted ones. Thus, we can obtain PET film with its top side charged at -1 kV and the back side charged at -1 kV- ΔV_f. Note that ΔV_f can be quite easily controlled by the grid voltage, V_g.

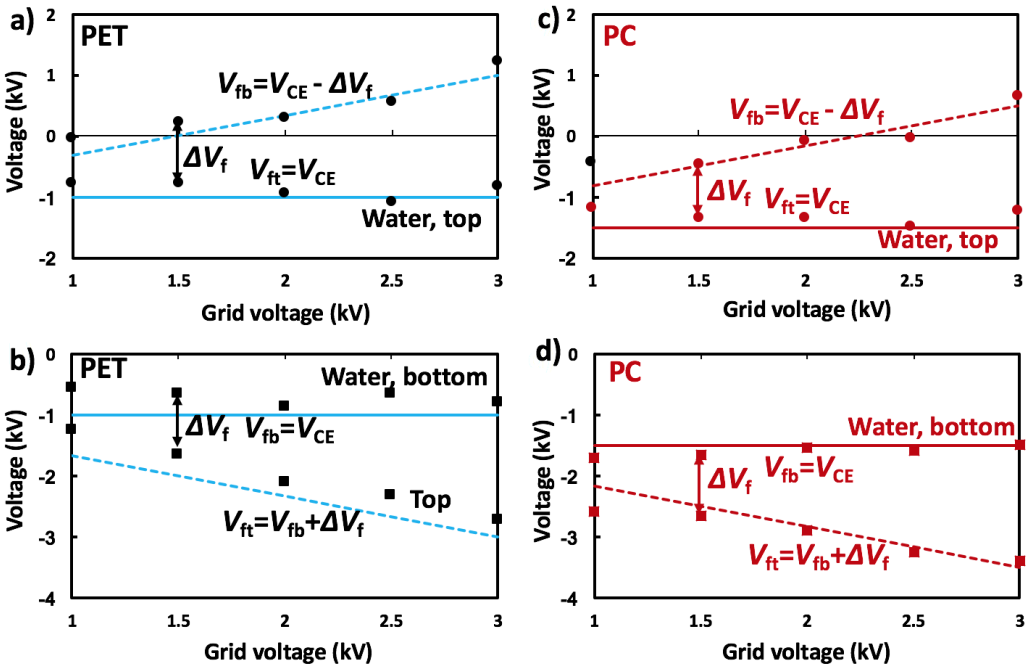

Figure 5.4 DI water treated corona charged PET and PC films with various grid voltages (V_g=-1 kV, -1.5 kV, -2 kV, -2.5 kV, or -3 kV): a) The top sides of corona charged PET films are treated with DI water; b) The back sides of corona charged PET films are treated with DI water; c) The top sides of corona charged PC films are treated with DI water; d) The back sides of corona charged PET films are treated with DI water.

For PET films with back sides treated by DI water, as shown in Figure 5.4b, the surface voltages at back sides should be around -1 kV, and the surface voltages at top sides should be -1 kV+ ΔV_f (the blue dotted lines in Figure 5.4b). The testing data shown by the black lines in Figure 5.4b fit with the prediction quite well.

Similar trend is detected for PC films (Figure 5.4 c, d); the only major different from PET films is that DI water treatment on PC films leads to a surface voltage around -1.5 kV; i.e. V_{ft}=-1.5 kV, and the back side would have a surface voltage around -1.5 kV-ΔV_f. When the back side is treated to be -1.5 kV, the top side surface voltage would be -1.5 kV+ ΔV_f. Hence, for either PET or PC film, we can use a liquid to treat one of its surface, so that the surface voltage changes to V_{CE}; the surface voltage on the other side would become V_{CE} - ΔV_f or V_{CE} +ΔV_f, depending on whether the treated surface is top side or back side. Note that ΔV_f can be adjusted by changing V_g.

Figure 5.5 demonstrates the voltage evaluation of the films shown in Figure 5.4, from day 0 to day 7 after DI water treatment. The date of measurement is indicated by the numbers (i = 0, 3, or 7) in the subscripts of $V_{ft,i}$ and $V_{fb,i}$. For the samples in Figure 5.4a, when V_g is lower than -3 kV, $|V_{ft}|$ is larger than $|V_{fb}|$ and an upward voltage shifting is observed. When V_g=-3 kV, $|V_{fb}|$ is larger than $|V_{ft}|$ and over time, the surface voltage moves downwards in the figure. After $|V_{ft}|=|V_{fb}|$ is reached, the surface voltages become relatively stable. Under this condition, the influence of free charges is minor and the dipolar charge distribution dominates. It should be related to the calculation in Chapter 3, which suggests that the surface density of CE-induced free charges is only a small fraction of the surface density of CC-induced dipolar distribution. Moreover, free charges tend to be unstable, because like charged particles repel each other; dipolar

charges tend to be stable, since the large Coulomb force strongly bond the oppositely charged particles across the thin film, yet the charges cannot move across the film thickness, due to the large electric resistivity of polymer. For PET films treated by DI water at the back side (Figure 5.5b), compared with Figure 5.5a, because $|V_{ft}|$ is larger so that the reduction of $|V_{ft}|$ tends to be faster. Figure 5.5c, d indicate that PC films exhibit similar characteristics under similar treatment conditions.

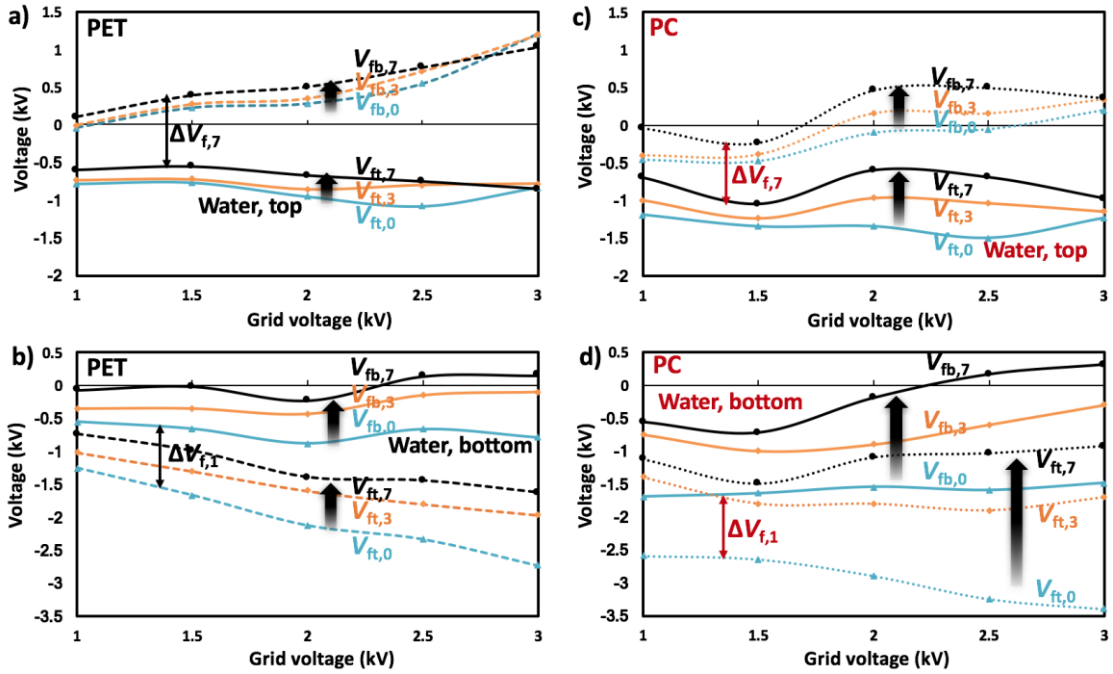

Figure 5.5 Change in surface voltage of DI water treated PET and PC films that have been corona charged with various grid voltages. The numbers in subscript indicate the date of measurement after DI water treatment. a) The top sides of corona charged PET films are treated with DI water; b) The back sides of corona charged PET films are treated with DI water; c) The top sides of corona charged PC films are treated with DI water; d) The back sides of corona charged PC films are treated with DI water.

Figure 5.6 shows the surface-voltage decay of DI water treated PET films that have been corona charged with various grid voltages (V_g). If treated with DI water on the top side, no matter how much ΔV_f is, immediately after the treatment, the surface

voltage of the top side ($V_{ft,i}$, with i = 0,1,2…indicating the date of measurement after the DI water treatment) always changes to around -1 kV, and reduces to about -0.7 kV after 7 days. The back sides of these films always show surface voltages $V_{fb,i}=V_{ft,i}-\Delta V_{f,i}$; the higher the $\Delta V_{f,i}$, the higher the $V_{fb,i}$. For the films charged with V_g lower than -2.5 kV, $|V_{ft,i}|$ is larger than $|V_{fb,i}|$, and the voltage tends to shift upwards; for films charged with V_g of -2.5 kV or -3 kV, $|V_{ft,i}|$ is smaller than $|V_{fb,i}|$ and the voltage tends to shift downwards. This result is compatible with Figure 5.5. When $|V_{ft,i}|=|V_{fb,i}|$, the voltages would be stable on both sides.

For the PET samples treated at the back side (Figure 5.6b), both V_{fb} and V_{ft} are negative, and $|V_{ft}|=|V_{CE}|+|\Delta V_f|$. The relatively high $|V_{ft}|$ offers a strong driving force for the evident upward shifting of the V_{ft} and V_{fb} curves. For instance, for films charged with V_g=-2 kV, $V_{ft,0}$=-2.1kV and $V_{fb,0}$=-0.88 kV; both are higher than if treated at the top side ($V_{ft,0}$=-0.96kV and $V_{fb,0}$=-0.28 kV). After 7 days, $V_{ft,7}$ becomes -1.45 kV and $V_{fb,7}$ becomes -0.15 kV, compared to, respectively, -0.75 kV and 0.78 kV of PET films treated on the top side. Again, over time, V_{ft} converges to $-V_{fb}$.

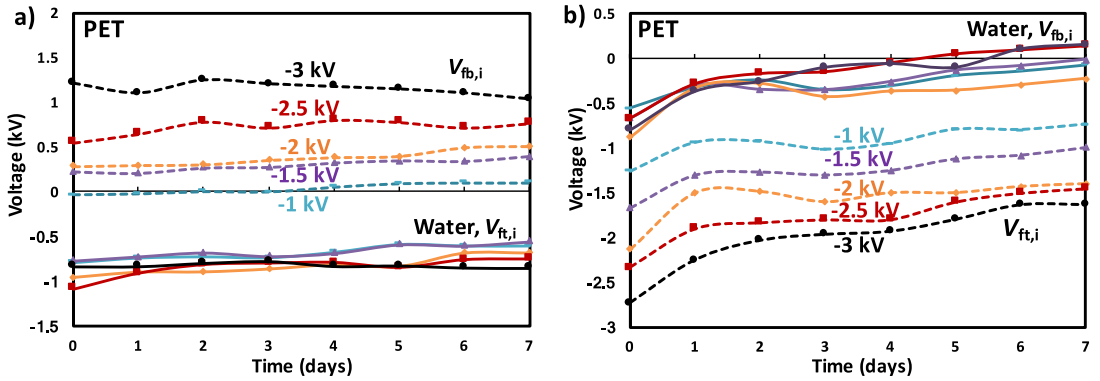

Figure 5.6 Surface voltage change of DI water treated PET films that have been corona charged with various grid voltages: a) The top sides and b) the back sides are treated by DI water.

5.3.3 Treating electrified films with aqueous solutions of IPA

As discussed in Chapter 4, applying aqueous solutions with different IPA concentrations to PET and PC films leads to different V_{CE}. Figure 5.7 shows the influence of IPA concentration, C_{IPA}, on V_{fb} and V_{ft} of PET and PC films. Prior to the IPA solution treatment, the films have been corona charged with V_g=-2 kV, with $\Delta V_f \approx$ -1.33 kV. The dotted blue lines in Figure 5.7a,b are for the influence of C_{IPA} on V_{CE} of PET films obtained in Chapter 4, and the predicted $V_{fb} = V_{ft}-\Delta V_f = V_{CE}-\Delta V_f$ for the films treated at top sides (Figure5.7a) and $V_{ft} = V_{fb} + \Delta V_f = V_{CE} + \Delta V_f$ for the films treated at back sides (Figure 5.7b). The black lines are the experimental results, well matching with the predicted data. For instance, when 5 vol.% IPA is applied to the top side of corona charged PET film, V_{ft} is changed as $V_{ft} = V_{CE}$ =-0.45 kV, and the surface voltage at the back side is shifted to 0.88 kV, same as the predicated $V_{fb} = V_{ft} - \Delta V_f = V_{CE} - \Delta V_f$ =-0.45-(-1.33)=0.88 kV.

When 5 vol.% IPA is applied to the back side of the corona charged PET film, V_{fb} is altered to $V_{fb} = V_{CE}$ =-0.3 kV, and the surface voltage of the top side is shifted to -1.53 kV, only slightly lower than the predicted $V_{ft} = V_{fb} + \Delta V_f = V_{CE} + \Delta V_f$ =-0.3+(-1.33) = -1.66 kV. Compatible with the results in Chapter 4, V_{CE} deceases with the increase in C_{IPA}, and the surface voltages on both sides shift together with it. Similar phenomena are observed on corona charged PC films, except that V_{CE} of the PC films have higher absolute values compared to the PET films. That is, by applying IPA solutions with various C_{IPA} onto corona charged PET and PC films, we can adjust V_{ft} and V_{fb}, through controlling V_{CE} and ΔV_f.

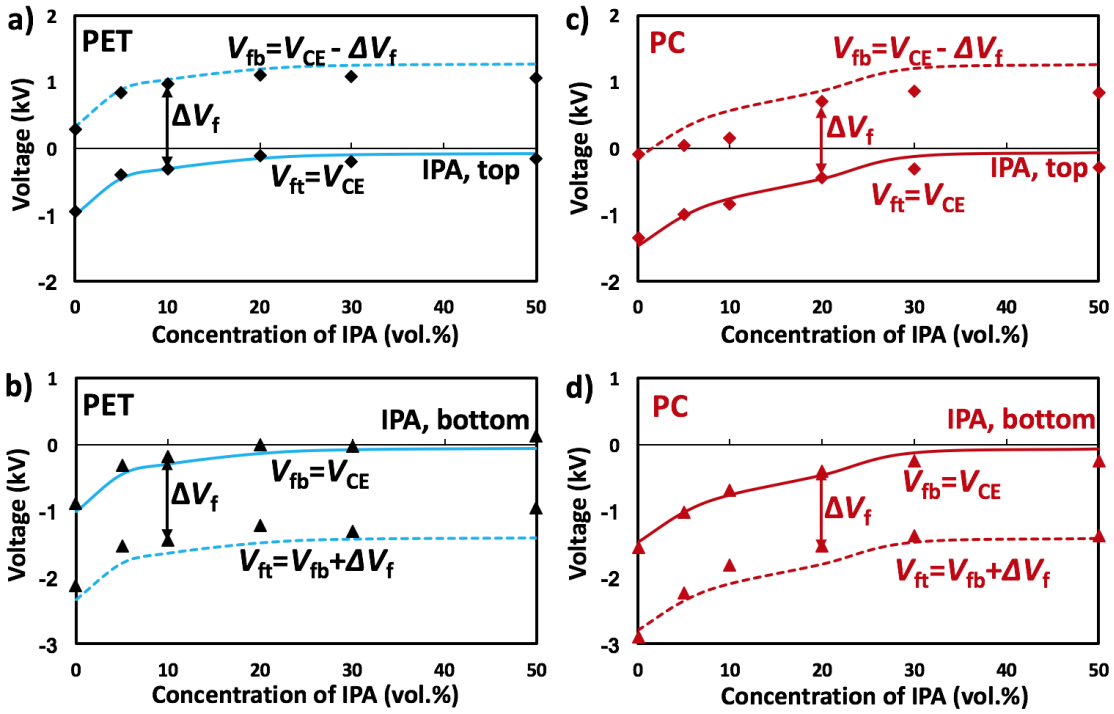

Figure 5.7 Surface voltages of corona charged PET and PC films (V_g=-2 kV) treated with aqueous solutions of IPA of various C_{IPA}: IPA solution is applied to a) the top sides and b) the back sides of PET films. IPA solution is applied to c) the top sides and d) the back sides of PC films.

Figure 5.8 shows the surface-voltage evolution of PET and PC films first corona charged with V_g=-2 kV and then rinsed by aqueous solutions of IPA of various C_{IPA}. For the PET films rinsed by IPA solutions on the top sides (Figure 5.8a), $|V_{fb}|$ is larger than $|V_{ft}|$, and V_{fb} is positive. With the change of ΔV_f being negligible, the major change of surface voltages is the downward shifting of the curves. The higher the $|V_{fb}|$, the more pronounced the shifting would be. For PET films treated with IPA solutions on the back sides (Figure5.8b), $|V_{ft}| > |V_{fb}|$, leading to the upward shifting of the curves. Similar behaviors are observed for PC films (Figure 5.8c and Figure 5.8d).

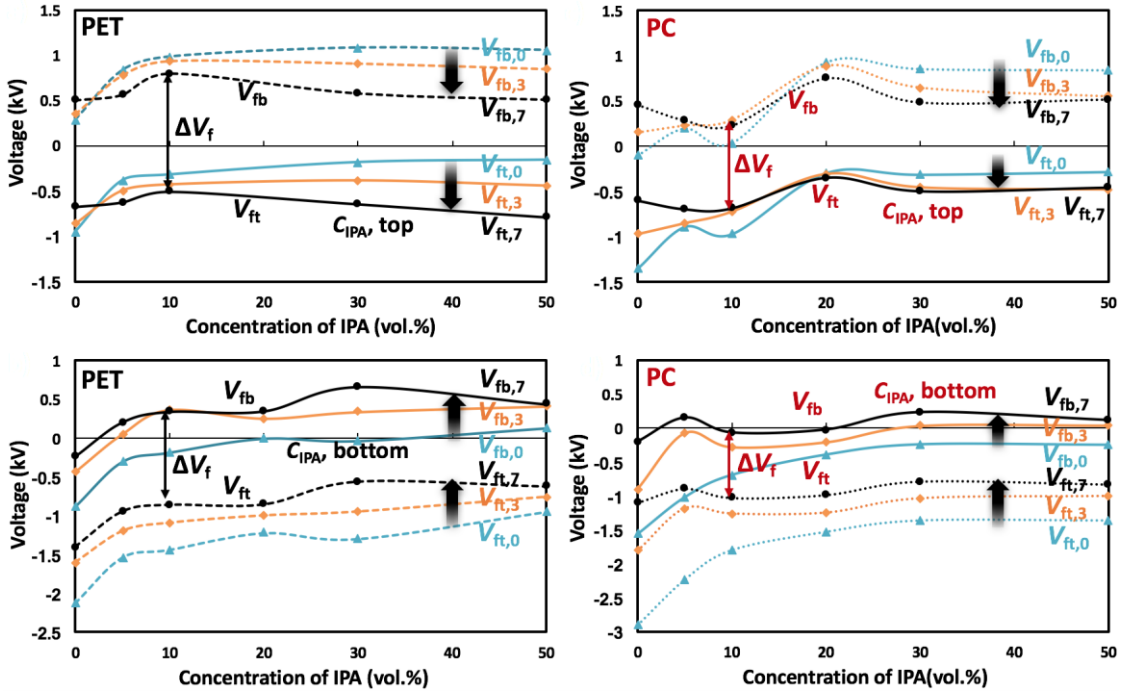

Figure 5.8 Surface-voltage evolution of PET and PC films first corona charged with V_g=-2 kV and then rinsed by aqueous solutions of IPA with various C_{IPA}. The numbers in subscript indicate the date of measurement after the IPA solution treatment. a) Top sides and b) back sides of PET films are treated with IPA solutions. c) Top sides and d) back sides of PC films are treated with IPA solutions.

Figure 5.9 shows the surface-voltage decay profiles of DI water treated, corona charged PET and PC films. In Figure 5.9a, when DI water is applied on the top sides of PET films, V_{ft} is conditioned to -1 kV and V_{fb} shifts to 0.28 kV. As $|V_{ft}| > |V_{fb}|$, $|V_{ft}|$ tends to reduce and $|V_{fb}|$ tends to increase over time, as indicated by the blue lines marked as "0" (i.e. $C_{IPA} = 0$). When the top side of PET film is treated with IPA solution of C_{IPA}=10 vol.%, V_{ft} is only -0.32 kV and V_{fb} is 0.98 kV, rendering $|V_{fb}| > |V_{ft}|$. Different from the results of $C_{IPA} = 0$, V_{fb} tends to reduce and V_{ft} tends to increase its absolute value. The V_{ft} offered by C_{IPA}=30 vol.% and C_{IPA}=50 vol.% are slightly lower than that of C_{IPA}=10

vol.%, and the surface-voltage voltages curves are similar. In general, the higher the C_{IPA}, the faster the changing rate of surface voltage.

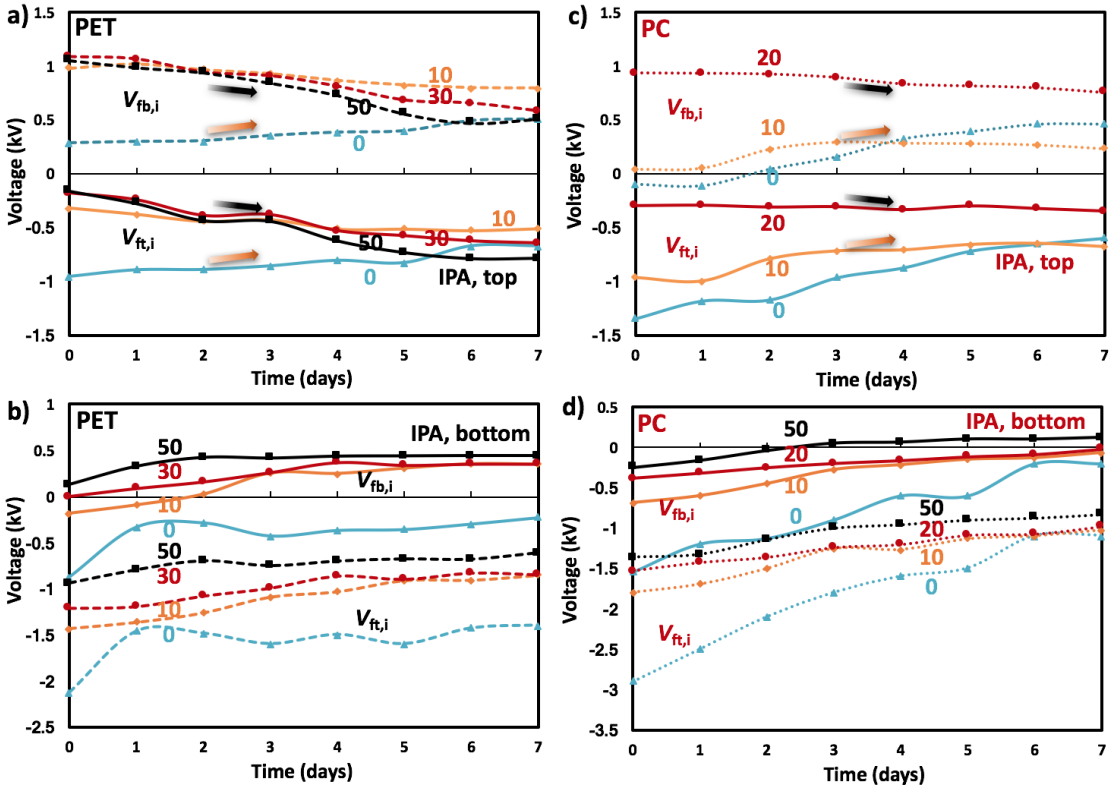

Figure 5.9 Surface-voltage profiles of PET and PC films first corona charged with V_g=-2 kV and then rinsed by aqueous solutions of IPA with various C_{IPA}: a) Top sides and b) back sides of PET films are treated with IPA solutions. c) Top sides and d) back sides of PC films are treated with IPA solutions.

For the PET films treated with IPA solutions on the back sides, $|V_{fb}|$ decreases with the increase in C_{IPA}, so that $|V_{ft}|$ is also lowered. $|V_{ft}|$ is larger than $|V_{fb}|$ for all the samples, and the surface-voltage profiles shift upwards over time. For the PC films with the top sides being treated by IPA solutions in Figure 5.9 c, when C_{IPA} < 10 vol.%, $|V_{ft}| > |V_{fb}|$ and the surface-voltage profiles shift upwards. When C_{IPA} exceeds 20 vol.%, $|V_{ft}| < |V_{fb}|$ and the surface-voltage profiles shift downwards. Note that the shifting of surface-

voltage profiles of the samples treated with 50 vol.% IPA solution ceases after 48 h, as $|V_{ft,2}|$ approaches $|V_{fb,2}|$. When the back sides are treated with IPA solutions (Figure 5.9d), the PC films behave similarly as the PET films, but with larger $|V_{fb}|$ and $|V_{ft}|$.

5.3.4 Treating corona charged polymer films with NaCl solutions

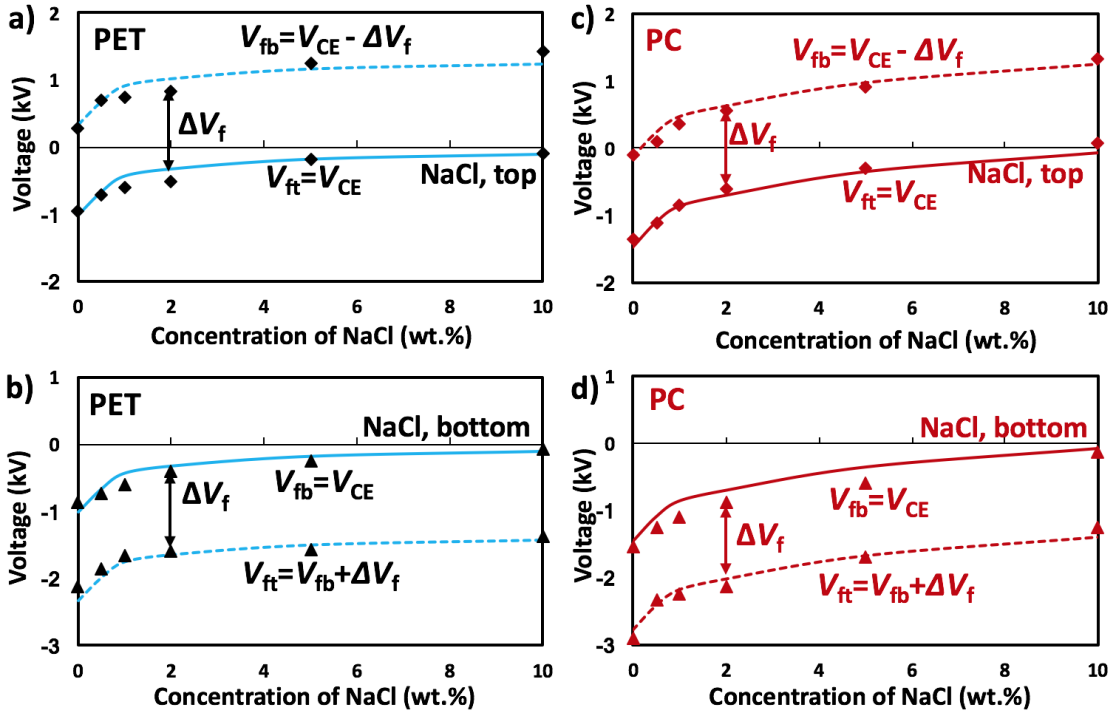

Figure 5.10 Surface voltages of corona charged PET and PC films (V_g=-2 kV) treated with NaCl solutions: NaCl solution is applied on a) the top sides and b) the back sides of corona charged PET films; NaCl solution is applied on a) the top sides and b) the back sides of corona charged PC films.

Figure 5.10 shows the influence of C_{NaCl} on V_{fb} and V_{ft} of corona charged PET and PC films. The grid voltage was -2 kV, resulting in $\Delta V_f \approx$ -1.33 kV. The results are similar as Figure 5.7: V_{ft} is controlled by C_{NaCl} for the films treated on the top sides and

$V_{fb}=V_{ft}-\Delta V_f$; V_{fb} is controlled by C_{NaCl} for the films treated on the back sides and $V_{ft}=V_{fb}+\Delta V_f$. As discussed in Chapter 4, V_{ft} and V_{fb} decrease with the increase in C_{NaCl}.

Over time, as shown in Figure 5.11, the basic characteristics of surface voltage change are similar to those of the samples treated with IPA solutions. The dominant factor is $|V_{ft}|$ or $|V_{fb}|$, whichever is larger; the surface voltages of the films shift to the direction in favor to reducing the larger value. The larger the magnitude of the surface voltage is, the faster it would vary.

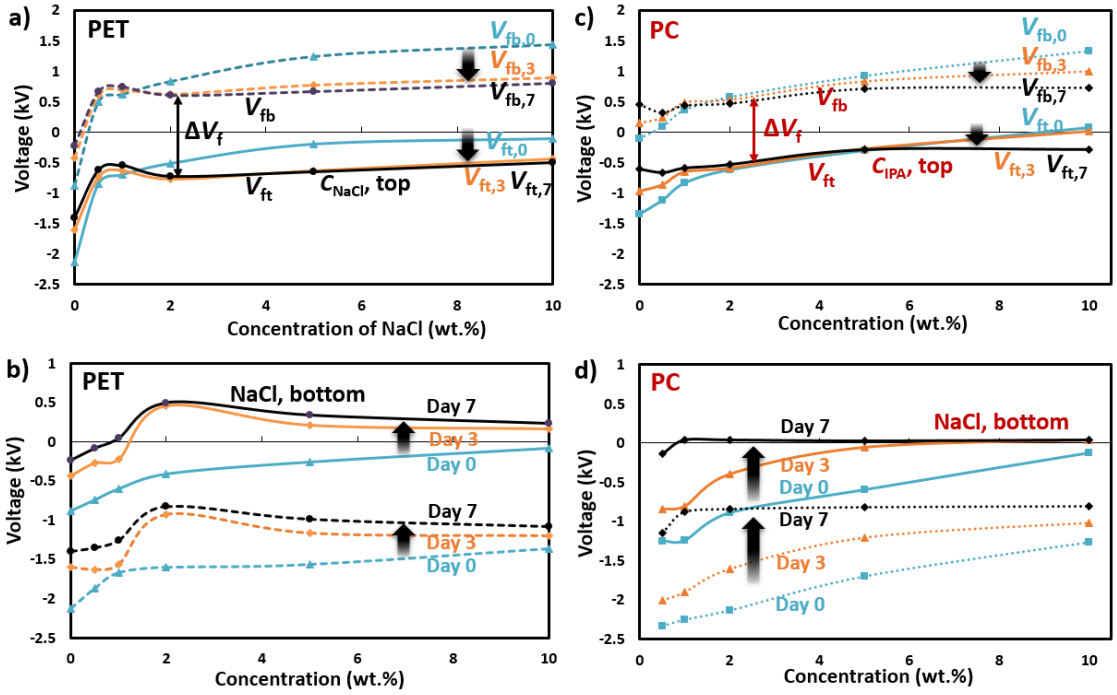

Figure 5.11 Surface-voltage change of PET and PC films first corona charged with V_g=-2 kV and then rinsed by NaCl solutions with various C_{NaCl}: a) Top sides and b) back sides of PET films are treated with NaCl solutions; c) top sides and d) back sides of PC films are treated with NaCl solutions.

Figure 5.12 shows the surface-voltage decay of the same samples as in Figure 5.10. The materials behaviors are somewhat similar as Figure 5.9. For PET films treated

at top sides, C_{NaCl} must be less than 1 wt% for the curves to shift upwards. When C_{NaCl} = 1 wt.%, the shift of surface-voltage curves is negligible. When C_{NaCl} = 5 wt. % or 10 wt.%, $|V_{fb}| > |V_{ft}|$ and the surface-voltage curves shift downwards over time. For PET films treated on the back sides, they show similar results as Figure 5.9b, with all the profiles shifting upwards. For PC film treated at top sides in Figure 5.9c, the critical C_{NaCl} of negligible profile shifting is also ~1 wt.%. Below it, $|V_{ft}| > |V_{fb}|$ and the profiles tends to shift upwards; above it, $|V_{fb}| > |V_{ft}|$ and the shifting is downward. For PC films treated at back sides, the results are similar to Figure 9d, but with higher surface voltage values.

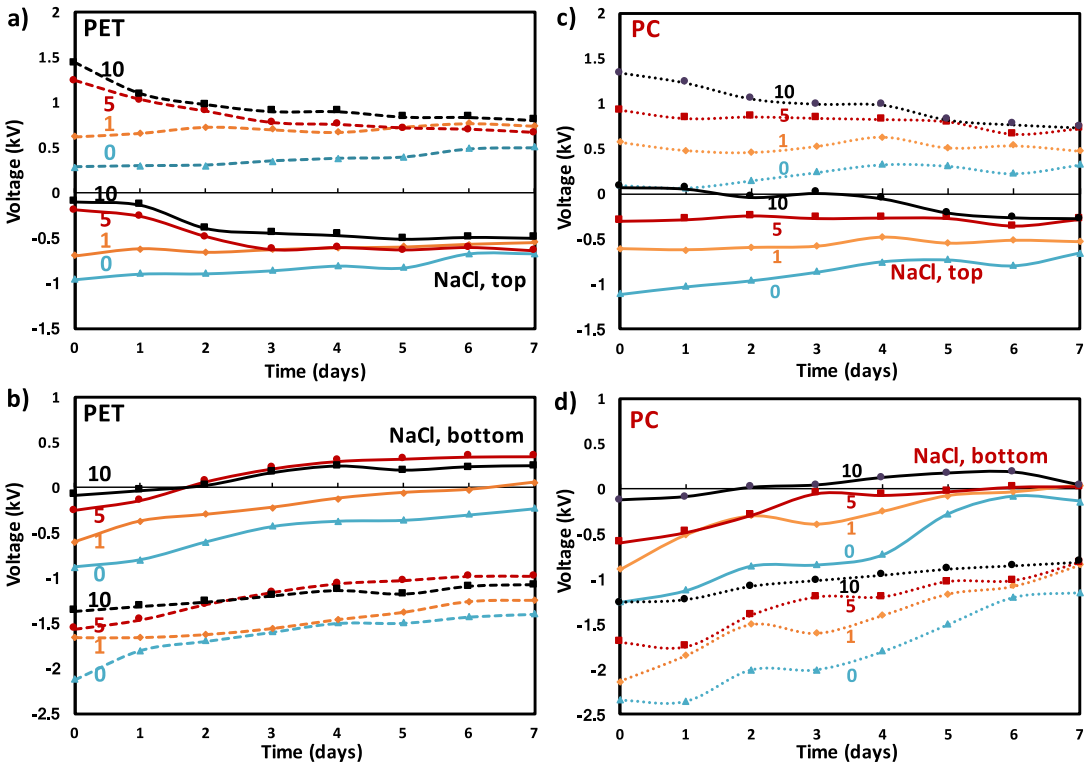

Figure 5.12 Surface-voltage profiles of PET and PC films first corona charged with V_g=-2 kV and then rinsed by NaCl solutions with various C_{NaCl}: a) Top sides and b) back sides of PET films treated with NaCl solutions; c) top sides and d) back sides of PC films treated with NaCl solutions.

5.3.5 Influence of external electric field

When a PC or PET film is rinsed by neat IPA, the surface potential of the rinsed side, V_{CE}, would be reduced to nearly zero. During the treatment, because IPA wets polymer very well, the polymer surface is fully covered by a thin liquid layer of IPA, which, under ambient condition, evaporates in about 7 min. If the drying takes place in in an external electric field, the surface voltage, V_{CE}', would no longer be zero but depend on the strength of the electric field, E. We rinse a 5.5 inch × 5.5 inch 125-μm-thick FEP film in NaCl solution and use it to provide external electric field for 3 inch × 3 inch PET films. The surface voltage of the FEP film, V_f, is in the range from -1 kV to -7 kV, depending on C_{NaCl}. The PET film is first corona charged with V_g=-2 kV, and one side of it is then rinsed by neat IPA. The PET film is placed next to the charged FEP film, while its surface is still fully wetted with IPA. The FEP and the PET films are in parallel, with the edges and the centers aligned with each other. The distance between them range from 25 mm to 100 mm. After the IPA layer has entirely evaporated, the surface voltages the PET films (V_{CE}') are measured by a fieldmeter from both sides.

It can be seen in Figure 5.13 that V_{CE}' increases nearly linearly with V_f, and decreases as z rises. Remarkably, under all the testing conditions, V_{CE}' is positive, contradictory to the tests without external electric field. For instance, if the PET film is placed 75 mm away from the charged FEP film with V_f = -4.5 kV, it would develop a V_{CE}' = +1.06 kV as the IPA layer evaporates.

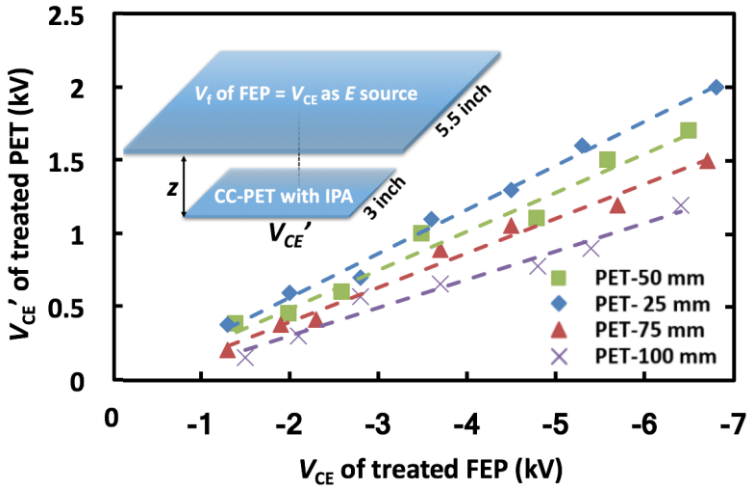

Figure 5.13 The influence of the surface voltage (V_f) and the distance (z) of FEP film on the voltage of corona charged PET film (V_{CE}'), measured from the side rinsed by IPA solution. The FEP film provides an external electric field. The PET-PET distance (z) is 25 mm, 50 mm, 75 mm, or 100 mm. The inset depicts the experimental setup.

According to Eq.3.4~3.7, based on the voltmeter reading (V_v), the charge density associated with dipolar component (σ_d) on the positive side and -σ_d on the negative side can be calculated. According to Eq.3.11, σ_s can be obtained based on the measurement of the surface voltage of PET films (V_{ft} and V_{fb}). When σ_d and σ_s are known, by using Eq.3.12, the distribution of electric potential in the space surrounding the CCCE-treated film, $V(x, y, z, \sigma_d, \sigma_s)$, can be calculated, with (x, y, z) indicating the location. Here, we define σ_1=σ_d+σ_s and σ_2 =-σ_d. The associated electric field, $\boldsymbol{E}$, and the strength of the electric field can be obtained based on Eq.4.1~4.2, for V_v=-2 kV, t=250 μm, and L=3 inch.

Define $\boldsymbol{E}_{\mathbf{PET,CC}}$ as the electric field caused by the CC-induced dipolar charge distribution and $\boldsymbol{E}_{\mathbf{PET,CE}}$ as the contribution from the CE-induced free charges. The summation of them is defined as $\boldsymbol{E}_{\mathbf{PET}}$. IPA tends to neutralize $\boldsymbol{E}_{\mathbf{FEP}}$ and $\boldsymbol{E}_{\mathbf{PET,CC}}$, by inducing free charges (σ_f) on the treated surface so that $\boldsymbol{E}_{\mathbf{PET,CC}}$+$\boldsymbol{E}_{\mathbf{PET,CE}}$=-$\boldsymbol{E}_{\mathbf{FEP}}$. When

there is no external electric field, $-\boldsymbol{E}_{\mathbf{FEP}}$ is zero and $\boldsymbol{E}_{\mathbf{PET,CC}} + \boldsymbol{E}_{\mathbf{PET,CE}}=0$. If $\boldsymbol{E}_{\mathbf{FEP}}$ is non-zero, $\boldsymbol{E}_{\mathbf{PET,CC}}+\boldsymbol{E}_{\mathbf{PET,CE}}$ is balanced by $-\boldsymbol{E}_{\mathbf{FEP}}$. When measured by the fieldmeter, the measurement result is caused by $\boldsymbol{E}_{\mathbf{PET,CC}}+\boldsymbol{E}_{\mathbf{PET,CE}}$. The solid lines in Figure 5.14 show the calculated relationship between V_f and $|\boldsymbol{E}|$ and the data points are our experimental results. Compared to the calculation results in Figure 4.8, we can see that the effect of the electric field induced by PET film is negligible. The charge density from CE is different with the result in Chapter 4, as the total charge density is from both CC and CE and σ_d is much larger than σ_f. Similar results of V_{CE}' on the IPA rinsed side can be obtained. On the other side of PET film, the voltage equals to V_{CE}'+ΔV_f or V_{CE}'-ΔV_f. That is, the external electric field offers an additional degree of freedom to modify CE-induced surface voltage.

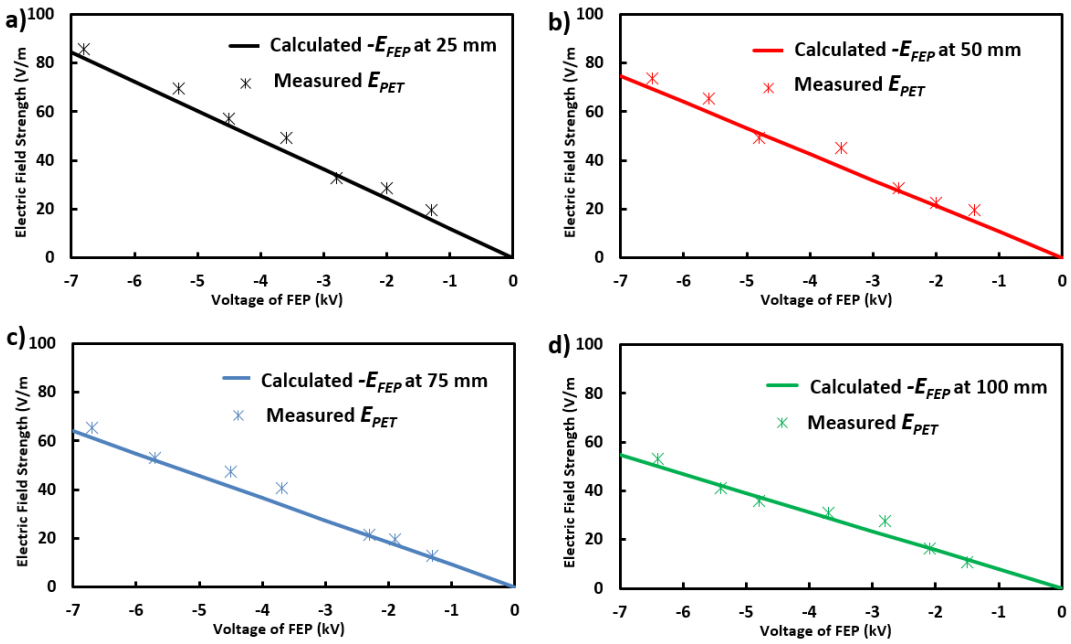

Figure 5.14 The calculated electric field strength produced by a 5.5-inch × 5.5-inch FEP film (E_{FEP}) and the measured electric field strength (E_{PET}) at the rinsed side of the 3-inch × 3-inch corona charged PET films: a) z = 25 mm, b) z = 50 mm, c) z = 75 mm, and d) z = 100 mm.

5.4 Conclusion Remarks

By performing contact electrification (CE) on corona charged (CC-ed) polymer films, we can control the surface voltages of both sides of the polymer films. The effect of CE always leads to the same surface voltage (V_{CE}) on the side being treated, quite independent of the corona charging. The surface voltage of the other side of the film is $V_{CE}+\Delta V_f$ or $V_{CE}-\Delta V_f$, depending on which side is exposed to CE treatment.

The CE-induced surface voltage (V_{CE}) decreases with the increase in the concentration of solute. It decays much faster than ΔV_f. Over time, the change in surface voltages of polymer film tends to reduce the difference between the absolute values of the voltages on both sides. Eventually, dipolar charge distribution is the most energetic favorable configuration.

With the influence of an external electric field on CE, the measured surface voltage of the rinsed side is mostly controlled by the external field, while the charge density is controlled by both CC and CE. The surface voltage of the other side is $V_{CE}'+\Delta V_f$ or $V_{CE}'-\Delta V_f$, depending on which side is exposed to CE treatment.

5.5 Acknowledgment

This chapter, in part, is a reprint of the material prepared to be submitted for publication. Ying Zhong, Rui Kou, Lewis Fowlergerace, Meng Wang, and Yu Qiao. Surface potential and interaction force control of polymer films. The dissertation author was the primary investigator and first author of the paper.

Chapter 6 Conclusions and future work

A triode corona charging system was built up, having controllable processing parameters. The surface voltages of electrified polymer films were typically close to the grid voltage. Increasing the needle voltage was beneficial to increasing the charged area; however, when the needle-grid distance was small or the needle voltage was high, the grid voltage might be unstable or non-uniform. To produce a large uniformly charged polymer surface, relatively large needle-electrode distance, small grid-electrode distance, large needle-grid distance, relatively high needle voltage, and relatively long charging time more than 20 sec are desirable.

When measured by a voltmeter, the surface voltages on the front and back sides of electrified polymeric film had opposite signs but nearly the same magnitude. Corona charging (CC) induced surface voltage could vary over time. Among the tested materials, the voltage change rates of PP, PET, and PC were much lower than those of FEP, PFA and PMMA. Increasing film thickness and lowering initial surface voltage helped increase the stability of surface potential. Charging polymer film at $T > T_g$ led to a low initial surface voltage, much below the grid voltage. Even though the surface voltage on each side of a charged film may change over time, the ratio of the voltmeter measurement result to the voltage difference measured by fieldmeter is nearly constant, independent of the film material, charging condition, and decay rate and time. This phenomenon can be well explained by the dipolar charge injection model. A small

variation in free charge, which can be as small as ~0.1% of the dipolar charge density, may drastically vary the absolute value of surface voltage, even altering the polarity.

The free charges are mostly produced through contact electrification (CE). The surface voltage of polymeric film induced by contact with liquid is quite controllable in the range of a few kV, corresponding to a surface charge density of a few $\mu C/m^2$. The control variables include the material of the film, the liquid composition, and the external electric field. When contacted with DI water, the surface voltages of PC, PET, and FEP films were -1.47 kV, -1.00 kV and -6.55 kV, respectively. When contacted with IPA, the surface voltages of all the films tended to be around aero. Upon exposure to aqueous solution of IPA or NaCl, the surface voltage of polymer film reduced with the increase of the concentration of IPA or NaCl. Simultaneously treating both sides of a film with different liquids could result in an average surface voltage. The stability of CE-induced charges was lower than CC-induced charges. After exposure to IPA, if the liquid layer on polymer film evaporated in an external electric field ends, the final surface voltage would be dominated by the electric field.

The potential difference of both sides of a polymer films can be controlled by the grid voltage of corona charging. Independent of CC, the surface voltage on either side of electrified polymer film can also be adjusted by CE. Thus, by combining CC and CE, we are able to precisely control the surface voltages of polymer films. The CE-induced free charges have a much lower surface density than CC-induced dipolar charges, and are inherently much more unstable. Hence, the stable charged state of polymer film is purely dipolar; both sides of the film have opposite polarities yet the same surface charge density. The surface voltage of the IPA-rinsed side of a corona

charged polymer film can also be modified by an external electric field; the surface voltage of the other side is determined by both the electric field and the corona charging grid voltage.

In the future, the charge injection depth, the charge injection mechanism, and the charge distribution in electrified polymer films will be investigated by laser induced modulation and pulsed electroacoustic. We will also conduct research on charge storage mechanisms of various polymer films. Microcosmic charge distribution characterization will be carried out through electrostatic force microscopy, so as to understand the processes that govern liquid-solid contact electrification and corona charging. In addition to regular polymers films, we will conduct corona charging on polymer nanofilms, which have important relevant to the development of ultra-insulating materials. Other dielectric materials, according to necessity, will be analyzed to gain a deep understanding of surface charge stability and distribution.

REFERENCES

[1] Buildings data book, Department of Energy, 2015.

[2] How much energy is consumed in U.S. residential and commercial buildings? www.eia.gov.

[3] Apte J., Arasteh D. Window-related energy consumption in the US residential and commercial building stock, Lawrence berkeley national laboratory, 2008,

[4] ENERGY STAR® program requirements for residential windows, doors, and skylights, www.energystar.gov.

[5] Benefits of ENERGY STAR qualified windows, doors, and skylights, www. energystar.

[6] Air conditioner power consumnption: deciphering the label, www.kompulsa.com.

[7] Cost of replacement windows, www.homewyse.com.

[8] Did you guys double glaze your windows, www.forums.whirlpool.net.

[9] Technical request from SHIELD program ARPA-E CFP, 21016

[10] Window and Storefront Thermal Performance: What every specifier needs to know, www.constructionspecifier.com.

[11] List of thermal conductivities, www.en.wikipedia.org.

[12] Ando E., Miyazaki M. Moisture resistance of the low-emissivity coatings with a layer structure of Al-doped ZnO/Ag/Al-doped ZnO. Thin Solid Films, 2001, 392(2): 289-293.

[13] Window technologies: low-e coatings, www.efficientwindows.org.

[14] Heat-reflecting low-e glass, www.explainthatstuff.com.

[15] Werner A., Roos A. Condensation tests on glass samples for energy efficient windows. Solar energy materials and solar cells, 2007, 91(7): 609-615.

[16] Storm window, www.en.wikipedia.org.

[17] Storm windows, www.energy.gov.

[18] Storm windows vs. replacement windows, www.stanekwindows.com.

[19] Jelle B.P., Baetens R., Gustavsen A. Aerogel insulation for building applications. The sol-gel handbook-synthesis, characterization, and applications: synthesis, characterization and applications, 2015, 3: 1385-1412.

[20] Baetens R., Jelle B.P., Gustavsen A. Aerogel insulation for building applications: A state-of-the-art review. Energy and Buildings, 2011, 43(4): 761-769.

[21] Woignier T., Phalippou J., Prassas M. Glasses from aerogels. Journal of Materials Science, 1990, 25(7): 3118-3126.

[22] Dorcheh A.S., Abbasi M.H. Silica aerogel; synthesis, properties and characterization. Journal of Materials Processing Technology, 2008, 199(1): 10-26.

[23] Hrubesh L.W. Aerogel applications. Journal of Non-Crystalline Solids, 1998, 225: 335-342.

[24] Kim G.S., Hyun S.H. Synthesis of window glazing coated with silica aerogel films via ambient drying. Journal of non-crystalline solids, 2003, 320(1): 125-132.

[25] He Y.L., Xie T. Advances of thermal conductivity models of nanoscale silica aerogel insulation material. Applied Thermal Engineering, 2015, 81: 28-50.

[26] Robitaille P.M. Kirchhoff's law of thermal emission: 150 years. Progress in Physics, 2009, 4, 3.

[27] Howell J.R., Menguc M.P., Siegel R. Thermal radiation heat transfer. CRC Press, 2010.

[28] Chen J., Ge X.S., Hu X.F. Single-layer heat mirror films and an improved method for evaluation of its optical and radiative properties in infrared. Solar Energy Materials and Solar Cells, 1998, 55(4): 323-329.

[29] Chiba K., Takahashi T., Kageyama T., Oda H. Low-emissivity coating of amorphous diamond-like carbon/Ag-alloy multilayer on glass. Applied Surface Science, 2005, 246(1): 48-51.

[30] Biswas P.K., De A., Pramanik N., Chakraborty P., Ortner K., Hock V., Korder S. Effects of tin on IR reflectivity, thermal emissivity, Hall mobility and plasma

wavelength of sol–gel indium tin oxide films on glass. Materials Letters, 2003, 57(15): 2326-2332.

[31] Low-e window film vs. replacement windows, www.pacific-tint.com.

[32] 3M low-e energy conservation films, www.3m.com.

[33] Low-emissivity window films, www.apexfilms.ca.

[34] Schaefer C., Bräuer G., Szczyrbowski J. Low emissivity coatings on architectural glass. Surface and Coatings Technology, 1997, 93(1): 37-45.

[35] Solovyev A.A., Rabotkin S.V., Kovsharov N.F. Polymer films with multilayer low-e coatings. Materials Science in Semiconductor Processing, 2015, 38: 373-380.

[36] Demiryont H., Parlar H., Ersoy A., Aktulga E. Anti-solar and low emissivity functioning multi-layer coatings on transparent substrates. Patent WO 1999065838 A1, 2000.

[37] Grenadyorov A.S., Rabotkin S.V., Parnyugin A. The effectiveness of low-emissivity coating on a polymer film, 7th International Forum on Strategic Technology (IFOST), 2012.

[38] Jacob S., Kasthurirengan S., Karunanithi R. Investigations into the thermal performance of multilayer insulation (300-77 K) Part 2: Thermal analysis. Cryogenics, 1992, 32(12): 1147-1153.

[39] Dunn B.D. Materials and processes: for spacecraft and high reliability applications, 2015.

[40] Finckenor M., Dooling D. Multilayer insulation material guidelines, 1999.

[41] Multi-layer insulation, www.wikipedia.org.

[42] Shraiman B.I., Siggia E.D. Heat transport in high-Rayleigh-number convection. Physical Review A, 1990, 42(6): 3650.

[43] Choy C. Thermal conductivity of polymers. Polymer, 1977, 18(10): 984-1004.

[44] Zhang S., Bogy D. A heat transfer model for thermal fluctuations in a thin slider/disk air bearing. International Journal of Heat and Mass Transfer, 1999, 42(10): 1791-1800.

[45] Tripathy S.K., Singh V., Murthy Y.R., Banerjee P., Suresh N. Influence of process parameters of dry high intensity magnetic separators on separation of hematite. International Journal of Mineral Processing, 2017, 160: 16-31.

[46] Kharisov B.I., Dias H.R., Kharissova O.V., Vázquez A., Pena Y., Gomez I. Solubilization, dispersion and stabilization of magnetic nanoparticles in water and non-aqueous solvents: recent trends. RSC Advances, 2014, 4(85): 45354-45381.

[47] Mukhopadhyay S., Donaldson J., Sengupta G., Yamada S., Chakraborty C., Kacprzak D. Fabrication of a repulsive-type magnetic bearing using a novel arrangement of permanent magnets for vertical-rotor suspension. IEEE Transactions on Magnetics, 2003, 39(5): 3220-3222.

[48] Rote D.M., Cai Y. Review of dynamic stability of repulsive-force maglev suspension systems. IEEE Transactions on Magnetics, 2002, 38(2): 1383-1390.

[49] Muxworthy A.R., Williams W. Critical superparamagnetic/single-domain grain sizes in interacting magnetite particles: implications for magnetosome crystals. Journal of the Royal Society Interface, 2008.

[50] Musolino A., Raugi M., Rizzo R., Tripodi E. Stabilization of a permanent-magnet MAGLEV system via null-flux coils. IEEE Transactions on Plasma Science, 2015, 43(5): 1242-1247.

[51] Jackson J.D. Electrodynamics. Wiley Online Library, 1975.

[52] Veit H.M., Diehl T.R., Salami A.P., Rodrigues J.S., Bernardes A.M., Tenório J.A.S. Utilization of magnetic and electrostatic separation in the recycling of printed circuit board scrap. Waste Management, 2005, 25(1): 67-74.

[53] Kwetkus B. Particle triboelectrification and its use in the electrostatic separation process. Particulate science and technology, 1998, 16(1): 55-68.

[54] Xu Y., Luo A., Zhang A., Zhang Y., Tang B., Wang K., Wang F. Spray coating of polymer electret with polystyrene nanoparticles for electrostatic energy harvesting. Micro & Nano Letters, 2016, 11(10): 640-644.

[55] Zhang H., Wang D. Controlling the growth of charged-nanoparticle chains through interparticle electrostatic repulsion. Angewandte Chemie, 2008, 120(21): 4048-4051.

[56] Nel A.E., Mädler L., Velegol D., Xia T., Hoek E.M., Somasundaran P., Klaessig F., Castranova V., Thompson M. Understanding biophysicochemical interactions at the nano-bio interface. Nature materials, 2009, 8(7): 543-557.

[57] Jho Y., Brown F.L., Kim M., Pincus P.A. Repulsion between oppositely charged planar macroions. PloS One, 2013, 8(8): e69436.

[58] Moazzami-Gudarzi M., Maroni P., Borkovec M., Trefalt G. Depletion and double layer forces acting between charged particles in solutions of like-charged polyelectrolytes and monovalent salt. Soft Matter, 2017,

[59] Black J.M., Walters D., Labuda A., Feng G., Hillesheim P.C., Dai S., Cummings P.T., Kalinin S.V., Proksch R., Balke N. Bias-dependent molecular-level structure of electrical double layer in ionic liquid on graphite. Nano Letters, 2013, 13(12): 5954-5960.

[60] Striemer C.C., Gaborski T.R., Mcgrath J.L., Fauchet P.M. Charge-and size-based separation of macromolecules using ultrathin silicon membranes. Nature, 2007, 445(7129): 749-753.

[61] Suzuki Y., Miki D., Edamoto M., Honzumi M. A MEMS electret generator with electrostatic levitation for vibration-driven energy-harvesting applications. Journal of Micromechanics and Microengineering, 2010, 20(10): 104002.

[62] Suzuki Y. Recent progress in MEMS electret generator for energy harvesting. IEEJ Transactions on Electrical and Electronic Engineering, 2011, 6(2): 101-111.

[63] Erhard D.P., Richter F., Bartz C., Schmidt H.W. Fluorinated aromatic polyimides as high- performance electret materials. Macromolecular Rapid Communications, 2015, 36(6): 520-527.

[64] Kestelman V.N., Pinchuk L.S., Goldade V.A. Electrets in engineering: fundamentals and applications. Springer Science & Business Media, 2013.

[65] Harris T. How Laser Printers Work. How Stuff Works in Space, 2007, 200: 1998-2015.

[66] Kim C., Goring D. Surface morphology of polyethylene after treatment in a corona discharge. Journal of Applied Polymer Science, 1971, 15(6): 1357-1364.

[67] Liston E., Martinu L., Wertheimer M. Plasma surface modification of polymers for improved adhesion: a critical review. Journal of Adhesion Science and Technology, 1993, 7(10): 1091-1127.

[68] Gerhard-Multhaupt R. Less can be more. Holes in polymers lead to a new paradigm of piezoelectric materials for electret transducers. IEEE Transactions on Dielectrics and Electrical Insulation, 2002, 9(5): 850-859.

[69] Baeg K.J., Noh Y.Y., Ghim J., Lim B., Kim D.Y. Polarity effects of polymer gate electrets on non-volatile organic field-effect transistor memory. Advanced Functional Materials, 2008, 18(22): 3678-3685.

[70] Jacobs H.O., Whitesides G.M. Submicrometer patterning of charge in thin-film electrets. Science, 2001, 291(5509): 1763-1766.

[71] Tsai P.P., Schreuder-Gibson H., Gibson P. Different electrostatic methods for making electret filters. Journal of Electrostatics, 2002, 54(3): 333-341.

[72] Arakawa Y., Suzuki Y., Kasagi N. Micro seismic power generator using electret polymer film. Proc Power MEMS, 2004, 187(190): 17.

[73] Bauser H., Ronge W. The electret ionization chamber: a dosimeter for long-term personnel monitoring. Health Physics, 1978, 34(1): 97-102.

[74] Neugschwandtner G.S., Schwödiauer R., Bauer-Gogonea S., Bauer S., Paajanen M., Lekkala J. Piezo-and pyroelectricity of a polymer-foam space-charge electret. Journal of Applied Physics, 2001, 89(8): 4503-4511.

[75] Kressmann R., Sessler G., Gunther P. Space-charge electrets. IEEE Transactions on Dielectrics and Electrical Insulation, 1996, 3(5): 607-623.

[76] Macdonald J.R. Theory of ac space-charge polarization effects in photoconductors, semiconductors, and electrolytes. Physical Review, 1953, 92(1): 4.

[77] Asano Y., Suzuki T. Characteristics of polyethylene terephthalate electrets. Japanese Journal of Applied Physics, 1972, 11(8): 1139.

[78] Quamara J., Kaushik B., Mahna S., Asokan K. Electret behaviour of ion irradiated polycarbonate and kapton-H polyimide films. Vacuum, 1997, 48(12): 995-997.

[79] Gerhard-Multhaupt R., Kunstler W., Gome T., Pucher A., Weinhold T., Seiß M., Xia Z., Wedel A., Danz R. Porous PTFE space-charge electrets for piezoelectric applications. IEEE Transactions on Dielectrics and Electrical Insulation, 2000, 7(4): 480-488.

[80] Li Y., Takada T. Progress in space charge measurement of solid insulating materials in Japan. IEEE Electrical Insulation Magazine, 1994, 10(5): 16-28.

[81] Santos L.P., Bernardes J.S., Galembeck F. Corona-treated polyethylene films are macroscopic charge bilayers. Langmuir, 2013, 29(3): 892-901.

[82] Gonz F.C. Charge-Storage Mechanisms in Polymer Electrets; University of Potsdam, 2006.

[83] Giacometti J.A., Oliveira O.N. Corona charging of polymers. IEEE Transactions on Electrical Insulation, 1992, 27(5): 924-943.

[84] Ding L., Shao L., Bai Y. Deciphering the mechanism of corona discharge treatment of BOPET film. RSC Advances, 2014, 4(42): 21782-21787.

[85] Xu Z., Zhang L., Chen G. Decay of electric charge on corona charged polyethylene. Journal of Physics D: Applied Physics, 2007, 40(22): 7085.

[86] Motyl E. Charging of polypropylene foils in corona triode system. Journal of Electrostatics, 1993, 30: 57-64.

[87] Gunther P. Mechanism of charge storage in electron-beam or corona-charged silicon-dioxide electrets. IEEE Transactions on Electrical Insulation, 1991, 26(1): 42-48.

[88] Collins G., Federici J., Imura Y., Catalani L.H. Charge generation, charge transport, and residual charge in the electrospinning of polymers: a review of issues and complications. Journal of Applied Physics, 2012, 111(4): 044701.

[89] Giacometti J.A., Fedosov S., Costa M.M. Corona charging of polymers: recent advances on constant current charging. Brazilian Journal of Physics, 1999, 29(2): 269-279.

[90] Molinié P. Charge injection in corona-charged polymeric films: potential decay and current measurements. Journal of Electrostatics, 1999, 45(4): 265-273.

[91] Toomer R., Lewis T. Charge trapping in corona-charge polyethylene films. Journal of Physics D: Applied Physics, 1980, 13(7): 1343.

[92] Prawatya Y., Neagoe B., Zeghloul T., Dascalescu L. Surface-electric-potential characteristics of tribo-and corona-charged polymers. A Comparative Study. IEEE Transactions on Industry Applications, 2017,

[93] Sahli S., Bellel A., Ziari Z., Kahlouche A., Segui Y. Measure and analysis of potential decay in polypropylene films after negative corona charge deposition. Journal of Electrostatics, 2003, 57(2): 169-181.

[94] Cabrera V.M., Cooray V. On the mechanism of space charge generation and neutralization in a coaxial cylindrical configuration in air. Journal of Electrostatics, 1992, 28(2): 187-196.

[95] Kumara S., Serdyuk Y.V., Gubanski S.M. Surface charge decay on polymeric materials under different neutralization modes in air. IEEE Transactions on Dielectrics and Electrical Insulation, 2011, 18(5):

[96] Moreno R., Gross B. Measurement of potential buildup and decay, surface charge density, and charging currents of corona-charged polymer foil electrets. Journal of Applied Physics, 1976, 47(8): 3397-3402.

[97] Molinie P., Goldman M., Gatellet J. Surface potential decay on corona-charged epoxy samples due to polarization processes. Journal of Physics D: Applied Physics, 1995, 28(8): 1601.

[98] Rouagdia K., Nemamcha M., Herous L., Dascalescu L., Mellouki H. Surface potential decay of DC-corona-charged PET films on humid electrodes. Journal of Electrostatics, 2015, 78(17-21.

[99] Eich M., Sen A., Looser H., Bjorklund G., Swalen J., Twieg R., Yoon D. Corona poling and real-time second-harmonic generation study of a novel covalently functionalized amorphous nonlinear optical polymer. Journal of Applied Physics, 1989, 66(6): 2559-2567.

[100] Lindner M., Bauer-Gogonea S., Bauer S., Paajanen M., Raukola J. Dielectric barrier microdischarges: Mechanism for the charging of cellular piezoelectric polymers. Journal of Applied Physics, 2002, 91(8): 5283-5287.

[101] Chen G., Xu Z., Zhang L. Measurement of the surface potential decay of corona-charged polymer films using the pulsed electroacoustic method. Measurement Science and Technology, 2007, 18(5): 1453.

[102] Bamji S., Jao K., Perlman M. Polymer electrets corona charged at high temperature. Journal of Electrostatics, 1979, 6(4): 373-379.

[103] Hampsch H.L., Yang J., Wong G.K., Torkelson J.M. Dopant orientation dynamics in doped second-order nonlinear optical amorphous polymers. 1. Effects of temperature above and below T_g in corona-poled films. Macromolecules, 1990, 23(15): 3640-3647.

[104] Kao K., Bamji S., Perlman M. Thermally stimulated discharge current study of surface charge release in polyethylene by corona-generated excited molecules, and the crossover phenomenon. Journal of Applied Physics, 1979, 50(12): 8181-8185.

[105] Gunther P. Charging, long-term stability, and TSD measurements of SiO/sub 2/electrets. IEEE Transactions on Electrical Insulation, 1989, 24(3): 439-442.

[106] Chen G. A new model for surface potential decay of corona-charged polymers. Journal of Physics D: Applied Physics, 2010, 43(5): 055405.

[107] Fleming R.J., Henriksen M.M., Henriksen M., Holboll J.T. LIPP and PEA space-charge measurements on LDPE, IEEE 5th International Conference on Conduction and Breakdown in Solid Dielectrics, 1995.

[108] Cui L.L.., Jiang J., Xia Z. F., Chen G. J., Wang Z. Z. Charge storage and transport in polymethylmethacrylate (PMMA) film. Journal of Electrostatics, 1998, 44(1-2): 61-65.

[109] Stark W., Harnisch F., Manthey W. Surface potential homogeneity of corona charged FEP and PVDF electrets. Journal of Electrostatics, 1990, 25(3): 277-285.

[110] Mizutani T., Ieda M. TSC from corona-charged high-density polyethylene and the effects of oxidation. Journal of Physics D: Applied Physics, 1978, 11(2): 185.

[111] Xu W., Liu X. Surface modification of polyester fabric by corona discharge irradiation. European Polymer Journal, 2003, 39(1): 199-202.

[112] Xia Z. Corona charging and charge decay of Teflon-PFA. IEEE Transactions on Electrical Insulation, 1991, 26(6): 1104-1111.

[113] Matsuura S., Takamatsu T. Electret state in blendmers of polypropylene, PP grafted with maleic anhydride and polycarbonate, 9th International Symposium on Electrets, 1996.

[114] Dahringer J., Albers E.A., Groh W., Heyer A. Non-wovens of electret fiber mixtures having an improved charge stability. Patent US5726107. 1998.

[115] Lu T.L. Charging temperature effect for corona charged Teflon FEP electret; 7th International Symposium on Electrets, 1991.

[116] Migahed M., Shaban A., El-Khodary A., Hafiz H. TSDC spectra in negatively corona charged ABS electrets. Polymer Bulletin, 1990, 23(1): 61-66.

[117] Qiu X., Xia Z., Wang F., Wu Y., Zhang Y. The electret behavior of poly (vinylidenefluoride/ chlorotrifluorethylene) film, 11th International Symposium on Electrets, 2002.

[118] Mccurry R., Schaffert R. Space-charge-limited currents in resin films. IBM Journal of Research and Development, 1960, 4(3): 359-363.

[119] Behrendt N., Greiner C., Fischer F., Frese T., Altstädt V., Schmidt H.W., Giesa R., Hillenbrand J., Sessler G. Morphology and electret behaviour of microcellular high glass temperature films. Applied Physics A: Materials Science & Processing, 2006, 85(1): 87-93.

[120] Prawatya Y., Neagoe B., Zeghloul T., Dascalescu L. Comparison between the surface-electric-potential characteristics of tribo-and corona-charged polymers, Industry Applications Society Annual Meeting, 2015.

[121] Handala M.A., Lamrous O. Surface degradation of styrene acrylonitrile exposed to corona discharge. European Transactions on Electrical Power, 2008, 18(5): 494-505.

[122] Zheng Z., Tang X., Shi M., Zhou G. A study of the influence of controlled corona treatment on UHMWPE fibres in reinforced vinylester composites. Polymer International, 2003, 52(12): 1833-1838.

[123] Xia Z., Wedel A., Danz R. Charge storage and its dynamics in porous polytetrafluoroethylene (PTFE) film electrets. IEEE Transactions on Dielectrics and Electrical Insulation, 2003, 10(1): 102-108.

[124] Künstler W., Xia Z., Weinhold T., Pucher A., Gerhard-Multhaupt R. Piezoelectricity of porous polytetrafluoroethylene single-and multiple-film electrets containing high charge densities of both polarities. Applied Physics A: Materials Science & Processing, 2000, 70(1): 5-8.

[125] Lacks D.J., Sankaran R.M. Contact electrification of insulating materials. Journal of Physics D: Applied Physics, 2011, 44(45): 453001.

[126] Zhang J., Zhang L., Wang W., Jia J., Tian Z., Tian Z.Q., Zhan D. Contact Electrification induced interfacial redox reactions and the electrochemical nanoimprint lithography directly in n-type gallium arsenate wafer. Chemical Science, 2016,

[127] Davies D. Charge generation on dielectric surfaces. Journal of Physics D: Applied Physics, 1969, 2(11): 1533.

[128] Lowell J., Rose-Innes A. Contact electrification. Advances in Physics, 1980, 29(6): 947-1023.

[129] Arthur D. A Review of static electrification. Journal of the Textile Institute Transactions, 1955, 46(12): T721-T734.

[130] Apodaca M.M., Wesson P.J., Bishop K.J., Ratner M.A., Grzybowski B.A. Contact electrification between identical materials. Angewandte Chemie, 2010, 122(5): 958-961.

[131] Lacks D.J. The unpredictability of electrostatic charging. Angewandte Chemie International Edition, 2012, 51(28): 6822-6823.

[132] Loeb L.B. The basic mechanisms of static. Science, 1945, 102(2658): 573-576.

[133] Baytekin H., Patashinski A., Branicki M., Baytekin B., Soh S., Grzybowski B.A. The mosaic of surface charge in contact electrification. Science, 2011, 333(6040): 308-312.

[134] Mccarty L.S., Whitesides G.M. Electrostatic charging due to separation of ions at interfaces: contact electrification of ionic electrets. Angewandte Chemie International Edition, 2008, 47(12): 2188-2207.

[135] Zhang C., Tang W., Zhang L., Han C., Wang Z.L. Contact electrification field-effect transistor. ACS Nano, 2014, 8(8): 8702-8709.

[136] Lin Z.H., Cheng G., Lin L., Lee S., Wang Z.L. Water-Solid Surface contact electrification and its use for harvesting liquid-wave energy. Angewandte Chemie International Edition, 2013, 52(48): 12545-12549.

[137] Helseth L., Guo X. Contact electrification and energy harvesting using periodically contacted and squeezed water droplets. Langmuir, 2015, 31(10): 3269-3276.

[138] Founded on the invention of corona treament. www.vetaphone.com.

[139] Kim C., Evans J., Goring D. Corona-induced autohesion of polyethylene. Journal of Applied Polymer Science, 1971, 15(6): 1365-1375.

[140] Lili C., Jian J., Zhongfu X., Gangjin C., Zhenzhong W. Charge storage and transport in polymethylmethacrylate (PMMA) film. Journal of Electrostatics, 1998, 44(1): 61-65.

[141] Olthuis W., Bergveld P. On the charge storage and decay mechanism in silicon dioxide electrets. IEEE Transactions on Electrical Insulation, 1992, 27(4): 691-697.

[142] Sarma M.P., Janischewskyj W. DC corona on smooth conductors in air. Steady-state analysis of the ionisation layer, the Proceedings of the Institution of Electrical Engineers, 1969.

[143] Tansel T., Ener Rusen S., Rusen A. Uniform, large surface-area polarization by modifying corona-electrodes geometry. Review of Scientific Instruments, 2013, 84(1): 015107.

[144] Fujita T., Toyonaga T., Nakade K., Kanda K., Higuchi K., Maenaka K. Selective electret charging method for energy harvesters using biased electrode. Procedia Engineering, 2010, 5: 774-777.

[145] Lang S., Muensit S. Review of some lesser-known applications of piezoelectric and pyroelectric polymers. Applied Physics A, 2006, 85(2): 125-134.

[146] Turnhout J.V., Staal R.E., Wubbenhorst M., Haan P.H.D. Distribution and stability of charges in porous polypropylene films, 10th International Symposium on Electrets, 1999.

[147] Kawai H. The piezoelectricity of poly (vinylidene fluoride). Japanese Journal of Applied Physics, 1969, 8(7): 975.

[148] Neugschwandtner G., Schwödiauer R., Bauer-Gogonea S., Bauer S. Large piezoelectric effects in charged, heterogeneous fluoropolymer electrets. Applied Physics A: Materials Science & Processing, 2000, 70(1): 1-4.

[149] Van Veldhuizen E., Rutgers W. Pulsed positive corona streamer propagation and branching. Journal of Physics D: Applied Physics, 2002, 35(17): 2169.

[150] Ieda M., Sawa G., Shinohara U. A decay process of surface electric charges across poyethylene film. Japanese Journal of Applied Physics, 1967, 6(6): 793.

[151] Wang T.J., Wei Y., Liu Y., Ju J., Sun H., Wang C., Lu H., Liu J. Direct observation of laser guided corona discharges. Scientific reports, 2015, 5.

[152] Xia Z., Gerhard-Multhaupt R., Künstler W., Wedel A., Danz R. High surface-charge stability of porous polytetrafluoroethylene electret films at room and elevated temperatures. Journal of Physics D: Applied Physics, 1999, 32(17): L83.

[153] Dias C., Marat-Mendes J., Giacometti J. Effects of a corona discharge on the charge stability of Teflon FEP negative electrets. Journal of Physics D: Applied Physics, 1989, 22(5): 663.

[154] Creswell R.A., Perlman M.M. Thermal currents from corona charged Mylar. Journal of Applied Physics, 1970, 41(6): 2365-2375.

[155] Lin Z.-H., Cheng G., Wu W., Pradel K.C., Wang Z.L. Dual-mode triboelectric nanogenerator for harvesting water energy and as a self-powered ethanol nanosensor. ACS Nano, 2014, 8(6): 6440-6448.

[156] Zhuang Y., Chen G., Chappell P., Rotaru M. Surface potential decay: Effect of different corona charging times, 2012 Annual Report Conference on Electrical Insulation and Dielectric Phenomena, 2012.

[157] Lowell J., Truscott W. Triboelectrification of identical insulators. II. Theory and further experiments. Journal of Physics D: Applied Physics, 1986, 19(7): 1281.

[158] O'grady P.F. Thales of Miletus: the beginnings of western science and philosophy. Routledge, 2017.

[159] Melnik O., Parrot M. Electrostatic discharge in Martian dust storms. Journal of Geophysical Research: Space Physics, 1998, 103(A12): 29107-29117.

[160] Merrison J.P., Gunnlaugsson H.P., Hogg M., Jensen M., Lykke J., Madsen M.B., Nielsen M., Nørnberg P., Ottosen T., Pedersen R. Factors affecting the electrification of wind-driven dust studied with laboratory simulations. Planetary and Space Science, 2012, 60(1): 328-335.

[161] Pähtz T., Herrmann H.J., Shinbrot T. Why do particle clouds generate electric charges? Nature Physics, 2010, 6(5): 364-368.

[162] Seanor D.A. Electrical properties of polymers. Elsevier, 2013.

[163] Kwetkus B., Sattler K., Siegmann H.C. Gas breakdown in contact electrification. Journal of Physics D: Applied Physics, 1992, 25(2): 139.

[164] Dwari R., Rao K.H. Fine coal preparation using novel tribo-electrostatic separator. Minerals Engineering, 2009, 22(2): 119-127.

[165] Diaz A. Contact electrification of materials: the chemistry of ions on polymer surfaces. The Journal of Adhesion, 1998, 67(1-4): 111-122.

[166] Pai D.M., Springett B.E. Physics of electrophotography. Reviews of Modern Physics, 1993, 65(1): 163.

[167] Johnson A.P., Cleaves H.J., Dworkin J.P., Glavin D.P., Lazcano A., Bada J.L. The Miller volcanic spark discharge experiment. Science, 2008, 322(5900): 404-404.

[168] Schönenberger C. Charge flow during metal-insulator contact. Physical Review B, 1992, 45(7): 3861.

[169] Lowell J. The role of material transfer in contact electrification. Journal of Physics D: Applied Physics, 1977, 10(17): L233.

[170] Lowell J. Tunnelling between metals and insulators and its role in contact electrification. Journal of Physics D: Applied Physics, 1979, 12(9): 1541.

[171] Lee L.-H. Dual mechanism for metal-polymer contact electrification. Journal of Electrostatics, 1994, 32(1): 1-29.

[172] Homewood K. Surface Contamination and Contact Electrification. Treatise on Clean Surface Technology, 1987: 235-245.

[173] Duke C., Fabish T. Contact electrification of polymers: A quantitative model. Journal of Applied Physics, 1978, 49(1): 315-321.

[174] Vick F. Theory of contact electrification. British Journal of Applied Physics, 1953, 4(S2): S1.

[175] Diaz A., Felix-Navarro R. A semi-quantitative tribo-electric series for polymeric materials: the influence of chemical structure and properties. Journal of Electrostatics, 2004, 62(4): 277-290.

[176] Lee J.H., Hinchet R., Kim T.Y., Ryu H., Seung W., Yoon H.J., Kim S.W. Control of skin potential by triboelectrification with ferroelectric polymers. Advanced Materials, 2015, 27(37): 5553-5558.

[177] Invernizzi F., Dulio S., Patrini M., Guizzetti G., Mustarelli P. Energy harvesting from human motion: materials and techniques. Chemical Society Reviews, 2016, 45(20): 5455-5473.

[178] Wang S., Lin L., Wang Z.L. Nanoscale triboelectric-effect-enabled energy conversion for sustainably powering portable electronics. Nano Letters, 2012, 12(12): 6339-6346.

[179] Zhu G., Chen J., Liu Y., Bai P., Zhou Y.S., Jing Q., Pan C., Wang Z.L. Linear-grating triboelectric generator based on sliding electrification. Nano Letters, 2013, 13(5): 2282-2289.

[180] Lindley K., Rowson N. Feed preparation factors affecting the efficiency of electrostatic separation. Physical Separation in Science and Engineering, 1997, 8(3): 161-173.

[181] Kornfeld M. Frictional electrification. Journal of Physics D: Applied Physics, 1976, 9(8): 1183.

[182] Felici N. Conduction and electrification in dielectric liquids: Two related phenomena of the same electrochemical nature. Journal of Electrostatics, 1984, 15(3): 291-297.

[183] Touchard G. Flow electrification of liquids. Journal of Electrostatics, 2001, 51(440-447.

[184] Sarid D. Scanning force microscopy: with applications to electric, magnetic, and atomic forces. Oxford University Press on Demand, 1994.

[185] Schaffert R., Oughton C. Xerography: A new principle of photography and graphic reproduction. Journal of the Optical Society of America, 1948, 38(12): 991-998.

[186] Urban A.S., Lutich A.A., Stefani F.D., Feldmann J. Laser printing single gold nanoparticles. Nano Letters, 2010, 10(12): 4794-4798.

[187] Jaworek A., Krupa A., Czech T. Modern electrostatic devices and methods for exhaust gas cleaning: A brief review. Journal of Electrostatics, 2007, 65(3): 133-155.

[188] Hamedi M., Karabulut E., Marais A., Herland A., Nyström G., Wågberg L. Nanocellulose Aerogels functionalized by rapid layer-by-layer assembly for high charge storage and beyond. Angewandte Chemie International Edition, 2013, 52(46): 12038-12042.

[189] Zwanikken J., Van Roij R. Charged colloidal particles and small mobile ions near the oil-water interface: Destruction of colloidal double layer and ionic charge separation. Physical Review Letters, 2007, 99(17): 178301.

[190] Gebauer J.S., Malissek M., Simon S., Knauer S.K., Maskos M., Stauber R.H., Peukert W., Treuel L. Impact of the nanoparticle-protein corona on colloidal stability and protein structure. Langmuir, 2012, 28(25): 9673-9679.

[191] Espinosa C.E., Guo Q., Singh V., Behrens S.H. Particle charging and charge screening in nonpolar dispersions with nonionic surfactants. Langmuir, 2010, 26(22): 16941-16948.

[192] Legrand B., Rollier A.S., Collard D., Buchaillot L. Suppression of the pull-in instability for parallel-plate electrostatic actuators operated in dielectric liquids. Applied Physics Letters, 2006, 88(3): 034105.

[193] Chuang W.C., Lee H.L., Chang P.Z. Hu Y.C. Review on the modeling of electrostatic MEMS. Sensors, 2010, 10(6): 6149-6171.

[194] Ball P. Fundamental physics: Feel the force. Nature, 2007, 447(7146): 772-774.

[195] Coombs T., Samad I., Ruiz-Alonso D., Tadinada K. Superconducting micro-bearings. IEEE Transactions on Applied Superconductivity, 2005, 15(2): 2312-2315.

[196] Hunter R.J. Zeta potential in colloid science: principles and applications. Academic Press, 2013.

[197] Sakata S., Inoue Y., Ishihara K. Precise control of surface electrostatic forces on polymer brush layers with opposite charges for resistance to protein adsorption. Biomaterials, 2016, 105: 102-108.

APPENDIX

Repulsive force between electrified polymer films by corona charging and contact electrification

1. Experimental

A measurement system was developed to characterize the repulsive forces among the corona charged, contact electrification (CCCE) modified polymer films, *F* (Figure4.1). It consisted of an analytical balance (Ohaus Explorer Scale-220), two polycarbonate (PC) racks as sample holders, and a glass shielding cage. Before testing, the surface electrostatic of all the components was eliminated by an electrostatic eliminator. The bottom rack was affixed on the balance. The upper rack was affixed on the ceiling of the cage. The height of both racks was more than 5 inch, to avoid the influence from the environment. The changes in measurement data were less than 1% as the rack length further increased. The distance between the upper and the lower racks was 3 mm.

A set of 250-μm-thick 3 inch × 3 inch PC films were electrified through a similar procedure as in Section 5.2.3. One electrified PC film was first placed on the bottom rack, and the scale was calibrated to zero. Another PC film of the same surface voltage was then attached onto the upper rack, with the edges aligned with the bottom film. The samples were carefully handled such that their surfaces were not in contact with any solid or liquid objects, except for the holding points of the racks.

The measurement results of the balance were recorded. Each pair of PC films were measured for 4 times, with the orientation of the upper film being turned by 90° clockwise every time. At least 3 pairs of samples were measured for each parameter setting

2. Results

In a similar setup as in the experiments discussed in Section 4.3.4, we carried out repulsive force measurement on CCCE-treated polymer films (Figure A1). Controlled by V_g, ΔV_f of the two films in Figure A1a are both -1.1 kV, and V_{ft} and V_{fb} of the bottom film are -1.9 kV and -0.8 kV, respectively. The side having the surface voltage of -1.9 kV faces toward the upper film. By contacting the upper films with various liquid, we change the voltage of the lower side of the upper film and measure its repulsive force with the bottom film. The results follow a similar linear pattern as in Chapter 4. The repulsive force is mostly determined by the surface voltages on the sides facing each other; the surface voltages are measured by fieldmeter. The influence of the back sides of the films is secondary. Compared with purely corona charged films, the surface voltages of CCCE-treated films can be adjusted to a much higher level, $V_{CE}+\Delta V_f$, with ΔV_f being much larger than V_{CE}. For instance, when the surface voltages of the sides facing each other are -4 kV and -3.7 kV respectively, the repulsive force can reach ~3 mN, more than twice as high as that of purely corona charged samples.

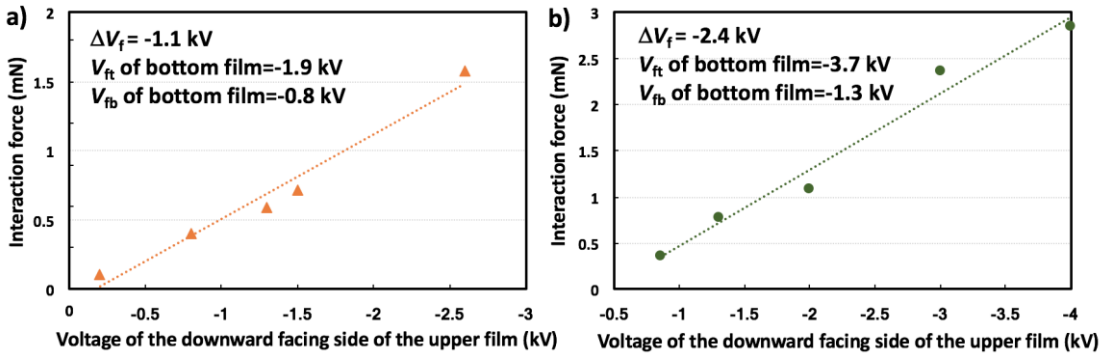

Figure A1 Repulsive force between electrified films: a) ΔV_f=-1.1 kV and V_{ft} of the bottom film is -1.9 kV; b) ΔV_f=-2.4 kV and V_{ft} of the bottom film is -3.7 kV.

3. Conclusion Remarks

The repulsive force between electrified films is dominated by the surface voltages of the two sides facing with each other, and proportional to the voltage of one of the films. CCCE-treated film can have a tailorable and much higher surface voltage (V_{CE}+ΔV_f) than a purely CE film, so it the associated repulsive force.